

NANOSCALE SURFACE FINISHING STUDIES AND CHARACTERIZATIONS
OF CADMIUM ZINC TELLURIDE CRYSTALS

A THESIS SUBMITTED TO
THE GRADUATE SCHOOL OF NATURAL AND APPLIED SCIENCES
OF
MIDDLE EAST TECHNICAL UNIVERSITY



BY
MERVE PINAR KABUKCUOĞLU

IN PARTIAL FULFILLMENT OF THE REQUIREMENTS
FOR
THE DEGREE OF MASTER OF SCIENCE
IN
PHYSICS

DECEMBER 2016

Approval of the Thesis:

**NANOSCALE SURFACE FINISHING STUDIES AND
CHARACTERIZATIONS OF CADMIUM ZINC TELLURIDE CRYSTALS**

submitted by **MERVE PINAR KABUKCUOĞLU** in partial fulfillment of the requirements for the degree of **Master of Science in Physics Department, Middle East Technical University** by,

Prof. Dr. Gülbin Dural Ünver
Dean, Graduate School of **Natural and Applied Sciences**

Prof. Dr. Sadi Turgut
Head of Department, **Physics**

Prof. Dr. Raşit Turan
Supervisor, **Physics Dept., METU**

Examining Committee Members:

Prof. Dr. Mehmet Parlak
Physics Dept., METU

Prof. Dr. Raşit Turan
Physics Dept., METU

Assoc. Prof. Dr. Y. Eren Kalay
Metallurgical and Materials Engineering Dept., METU

Assoc. Prof. Dr. Alpan Bek
Physics Dept., METU

Assoc. Prof. Dr. Emrah Kalemci
Fac. of Engineering and Natural Sciences, Sabancı University

Date: 15.12.2016



I hereby declare that all information in this document has been obtained and presented in accordance with academic rules and ethical conduct. I also declare that, as required by these rules and conduct, I have fully cited and referenced all material and results that are not original to this work.

Name, Lastname: Merve Pınar Kabukcuođlu

Signature:

ABSTRACT

NANOSCALE SURFACE FINISHING STUDIES AND CHARACTERIZATIONS OF CADMIUM ZINC TELLURIDE CRYSTALS

Kabukcuoğlu, Merve Pınar

MS, Department of Physics

Supervisor: Prof. Dr. Raşit Turan

December 2016, 116 pages

Cadmium Zinc Telluride ($\text{Cd}_{1-x}\text{Zn}_x\text{Te}$, CdZnTe) crystals are used in two different applications depending on Zinc (Zn) concentrations. CdZnTe crystals are one of the most promising materials for X-ray and gamma-ray detector applications due to unique material properties such as high atomic number and high resistivity. Wide band gap and high stopping potential of CdZnTe crystals allow operation at room temperature for high performance detectors with several applications including medical imaging, astronomy, and homeland security. CdZnTe crystals are also known to be substrate material for epitaxial growth of Mercury Cadmium Telluride (HgCdTe, MCT) high performance infrared detectors by Molecular Beam Epitaxy (MBE) since lattice constants of HgCdTe and $\text{Cd}_{0.96}\text{Zn}_{0.04}\text{Te}$ are perfectly matched. Producing high quality epi-ready substrates with low defect density on large size wafers (i.e. 2 cm x 2 cm) is highly critical for the MCT based infrared detectors. High quality MBE requires uniform zinc concentration and low-defect density.

This thesis focuses on surface treatments and characterization of finished $\text{Cd}_{1-x}\text{Zn}_x\text{Te}$ single crystals with surface quality factors such as surface roughness and orientation accuracy for {111} and {211} orientations. These two application desire ultra-flat wafers

with desired thickness variation. The main aim is to have sub-nanometer surface roughness and ultra-flat surfaces on the large wafer areas. Within the scope of surface finishing studies, I focused on the optimization of lapping and polishing processes with respect to material removal rate (MRR) and its relation to surface roughness. Nano-mechanical behaviors of various crystallographic orientations and different zinc concentrations were to be understood for machining damage and MRR.

Surface and subsurface damages prevent growth of high quality MCT epi-layers on CZT substrates. Microcracks, plastic deformations, and dislocations induced by machining processes are the main issues required to be investigated. The surface topography and morphology after each process was observed by surface profilometer, atomic force microscopy (AFM), and scanning electron microscopy (SEM) techniques. Surface and subsurface damage were observed by SEM to understand induced defects after each surface process.

Finished CdZnTe single crystals have been characterized in terms of structural, compositional, and optical. X-ray Diffraction (XRD), Electron Dispersive X-ray (EDX) Spectroscopy, and Fourier Transform Infrared (FTIR) methods were employed after each surface treatment to understand the effect of surface preparations. Moreover, Te-inclusions that appears during mechanical polishing analyzed after polishing and chemical etching with Nakagawa and Everson etchants.

(211) and (111) oriented CdZnTe crystals having sizes up to 20 x 30 mm² were sliced with high orientation accuracy based on XRD measurements. Sub-nanometer surface roughness rms down to 0.4 nm was achieved on larger surface area. Zinc distribution throughout finished samples were uniform to be around 10% for Cd_{0.90}Zn_{0.10}Te and 4% for Cd_{0.96}Zn_{0.04}Te crystals. CdZnTe crystals are stoichiometric after final chemical polishing. IR transmittance of mirror-like polished samples were near 66%, which is the theoretical limit.

Keywords: CdZnTe, surface finishing, surface roughness, MRR

ÖZ

KADMIYUM ÇİNKO TELLÜR KRİSTELLERİNİN NANO DÜZEYDE YÜZEY HAZIRLAMA ÇALIŞMALARI VE KARAKTERİZASYONU

Kabukcuoğlu, Merve Pınar

Yüksek Lisans, Fizik Bölümü

Tez Yöneticisi: Prof. Dr. Raşit Turan

Aralık 2016, 116 sayfa

Kadmiyum Çinko Tellür ($Cd_{1-x}Zn_xTe$, $CdZnTe$) kristalleri çinko dağılımına bağlı olarak farklı alanlarda kullanılır. Yüksek atom nmarası ve yüksek direnç gibi özdeün özelliklere sahip olmasından dolayı $CdZnTe$ kristalleri X-ray ve gama-ray algılayıcıları uygulamalarında en çok umut vaat eden malzemelerden biridir. $CdZnTe$ kristallerinin geniş bant aralığı ve yüksek durdurma potansiyeli, oda sıcaklığında yüksek performanslı algılayıcılar için tıbbi görüntüleme, astronomi ve ulusal güvenlik gibi bir çok alanda kullanımına izin vermektedir. $CdZnTe$ kristalleri aynı zamanda moleküler ışın epitaksisi (MBE) yöntemi ile yüksek performanslı kızılötesi algılayıcı olan Cıva Kadmiyum Tellür'ün ($HgCdTe$, MCT) epitaksiyel katman büyütmesi için alt taş malzeme olarak kullanılmaktadır. $HgCdTe$ ve $CdZnTe$ kristallerinin örgü uyumu mükemmel olarak eşleşmektedir. Yüksek kalite epi-hazır alt taşlarda geniş yüzey alanında (2 cm x 2 cm) düşük kusur yoğunluğuna sayıp olması MCT kızılötesi algılayıcılar için oldukça kritiktir.

Bu tezde yüksek kaliteli $Cd_{1-x}Zn_xTe$ tek kristal yüzey hazırlama ve bunların karakterizasyonuna özellikle yüzey kalitesini etkileyen faktörlerden yüzey pürüzlülüğü ve {111} ile {211} yönelimlerindeki yönelim hassiyeti üzerine yoğunlaşmıştır. Yüksek kaliteli MBE'de üniform çinko dağılımı ve düşük kusur yoğunluğu oldukça önemlidir. İstenilen kalınlıkta oldukça düz örnekler iki uygulama alanı içinde istenmektedir. Geniş

yüzey alanında nanometre altı yüzey pürüzlülüğünün hazırlanması amaçlanmıştır. Yüzey hazırlama çalışmaları kapsamında malzeme kaldırma oranı ve bunun yüzey pürüzlülüğü arasındaki ilişkiye göre düzleme ve parlatma işlemlerinin optimizasyonu tamamlanmıştır. Mekaniksel hasarlar ve malzeme kaldırma oranı için çeşitli kristalografik yöntemler ve farklı çinko konsantrasyonların nano-mekanik davranışları incelenmiştir.

Yüzey ve altyüzey hasarları, CdZnTe alt taş üzerinde yüksek kaliteli MCT epi-katman büyümesini engellemektedir. Mekanik işlemler sırasında (kesme, düzleme ve parlatma) ortaya çıkan mikroçatlak, plastik bozulmalar ve kayma (dislokasyon) incelenmesi gerekmektedir. Her yüzey hazırlama işlemi sonrası yüzey topografisi ve morfolojisi yüzey profilometresi, atomik kuvvet mikroskobu (AFM) ve taramalı elektron mikroskobu (SEM) ile analiz edilmiştir. Yüzey ve yüzey altı hasarlar yüksek çözünürlük taramalı elektron mikroskobu ile farklı işlemler sırasında oluşturulan kusurlar incelenmiştir.

Yüzeyi hazırlanan tek kristal alana sahip CdZnTe kristalleri yapısal, bileşimsel ve optiksel olarak karakterize edilmiştir. Yüzey hazırlama çalışmalarının etkisini anlamak için her yüzey hazırlama işleminden sonra X-ışını kırınımı (XRD), elektron kırınımı X-ışını spektroskopisi (EDX) ve kızılötesi geçirgenlik (FTIR) yöntemleri kullanılmıştır. Yüzey işlemlerinin yüzey kalitesini önemli derecede etkilediği tespit edilmiştir. Buna ek olarak, mekanik parlatma sırasında ortaya çıkan Te-birikintileri, Nakagawa ve Everson aşındırıcıları ile parlatma ve kimyasal aşınma sonrası analiz edilmiştir.

10 x 10 mm²'den büyük yüzey alanına sahip {211} ve {111} yönelimine sahip CdZnTe kristalleri XRD ölçümlerine dayanılarak yüksek oryantasyon hassasiyeti ile dilimlendi. Geniş yüzey alanında nanometre-altı, yaklaşık olarak 0.4 nm, yüzey pürüzlülüğü elde edildi. Yüzey hazırlama işleri sırasında örnek yüzeyinde çinko konsantrasyonu Cd_{0.90}Zn_{0.10}Te kristalleri için yaklaşık %10 ve Cd_{0.96}Zn_{0.04}Te kristalleri için yaklaşık olarak %4 olarak ölçülmüştür. Ayna gibi parlatılmış yüzeylerde kızılötesi geçirgenlik %60'dan fazla ölçülmüştür.

Anahtar Kelimeler: CdZnTe, yüzey hazırlama, yüzey pürüzlülüğü, MRR



To my family

ACKNOWLEDGMENTS

First of all, I would like to express my deepest appreciation to my supervisor Prof. Dr. Raşit Turan for his endless support and guidance during my M.Sc. study. I am very grateful him for giving me change to work such a valuable topic to operate a set of valuable experimental equipment, providing me a key role at Crystal Growth Laboratory and encouraging me through my researches.

I would like to thank Prof. Dr. Mehmet Parlak for his supportive attitude, informative discussions and kindness. I am grateful to him for sharing the ideas about experimental techniques and experiences in semiconductor technology.

I would like to thank to Assoc. Prof. Dr. Y. Eren Kalay for his guidance, helpful discussions and kind approach. I am delightful to him for sharing deep experiences in crystallography during slicing experiments.

I gratefully thank to my colleagues from METU-CGL.

I sincerely thank to Yasin Ergunt for his sharing deep knowledge on CdZnTe growth and surface preparation and guiding me during this study. I really appreciate his infinite support, kindness and endless friendship. I can honestly say that I am more than lucky to work with such a talented person and to have excellent friend.

I also would like to thank to Bengisu Yaşar for SEM operations. I am grateful to work with Özden Başar Balbaş for his kindness, supportive behaviors and encouragements during my studies.

I would like to thank to Burak Aşıcı, Cüneyt Eroğlu and Ayşe Şan for creative ideas, helpful discussions and their priceless work attitude. I am also grateful them for sharing deep knowledge in CdZnTe growth and manufacturing technology, allowing to use white light interferometer and x-ray back reflection equipment. I also would like to thank to İsmail Soyalp for dicing our samples and Melih Kaldırım for helping XRD measurements.

Special thanks go to Mustafa Ünal for his support and friendship during master study. I also would like to thank him for teaching me AFM and SEM measurements and his valuable suggestions for characterization techniques.

I would like to thank to Dr. Tahir Çolakoğlu and Kurtuluş Abak for their endless support, creative ideas, motivational words and all discussions during coffee times. I am grateful them for sharing deep experiences on semiconductor technology and measurement techniques.

I would like to thank to GÜNAM family, especially Hande Çiftpınar, Serra Altınoluk, Ergi Dönerçark, Olgu Demircioğlu, Zeynep Demircioğlu, Hasan Hüseyin Güllü, Seda Kayra Güllü, Dr. Hisham Nasser and Mona Zolfaghari Borra for their friendship and kindness all times.

I am grateful to GÜNAM technicians for their technical supports and kindness: Tayfun Yıldız, Yücel Eke, Nevzat Görmez and Dursun Erdoğan.

Special thanks to my dearest friends Gamze Kökbudak and Hande Kılıç for their excellent friendships and endless support for more than seven years.

Finally, I would like to thank to Mehmet Ali Nebioğlu for his encouraging support, endless patient and being there whenever I need.

Last but not the least, I would like to thank to family for believing and supporting me about all my decisions throughout my life.

TABLE OF CONTENTS

ABSTRACT	v
ÖZ.....	vii
ACKNOWLEDGMENTS.....	x
TABLE OF CONTENTS	xii
LIST OF TABLES	xv
TABLE OF FIGURES	xvi
CHAPTER 1.....	1
1.1 Importance of CdZnTe Crystals	1
1.2 Manufacturing of CdZnTe Crystals	2
1.3 Outline of the Thesis	6
CHAPTER 2.....	7
2.1 Properties of CdZnTe	7
2.1.1 Crystal Structure.....	7
2.1.2 Polarity of CdZnTe Crystals	10
2.1.3 Band Structure.....	11
2.1.4 Mechanical Properties	12
2.1.5 Optical Properties.....	14
2.2 Crystalline Defects in CdZnTe.....	17
2.2.1 Grains and Grain Boundaries	17
2.2.2 Twins	18
2.2.3 Dislocations	19
2.2.4 Te Inclusions	22

2.3 Theory of Surface Finishing Studies.....	24
2.3.1 Theory of Lapping.....	26
2.3.2 Theory of Polishing.....	28
2.3.3 Material Removal Mechanisms	31
CHAPTER 3	33
3.1 Surface Preparation Processes.....	33
3.1.1 Grain Revealing Etching	34
3.1.2 Orientation Dependent Slicing.....	36
3.1.3 Polarity Determination.....	40
3.1.4 Lapping Processes.....	41
3.1.5 Polishing Processes	43
3.1.6 Material Removal Rate (MRR) Studies	44
3.2 Crystal Characterizations	46
3.2.1 Surface Characterizations.....	46
3.2.1.1 Surface Roughness Measurements.....	46
3.2.1.2 Surface Morphology Measurements	47
3.2.2 Structural Characterizations	47
3.2.2.1 Crystal Orientation od CdZnTe Crystals.....	48
3.2.2.2 Surface Composition of CdZnTe Crystals	48
3.2.2.3 IR-Transmittance of CdZnTe Crystals.....	48
3.2.2.4 Defect Revealing Etching for CdZnTe Crystals	49
3.3 Nano-mechanical Characterization of Crystals.....	50
3.4 Subsurface Damage Experiments	50
CHAPTER 4	53
4.1 Material Removal Rate Studies.....	53

4.1.1 Material Removal Rate Studies for Lapping Procedure.....	54
4.1.2 Material Removal Rate Studies for Polishing Procedures	59
4.2 Surface Characterizations.....	61
4.2.1 Lapped Surface Characterization	62
4.2.1.1 Surface Roughness of Lapped Crystals.....	62
4.2.1.2 Surface Morphology Analyses of Lapped Crystals.....	67
4.2.2 Surface Characterizations after Polishing	71
4.2.2.1 Surface Roughness of Polished Crystals	72
4.2.2.2 Surface Morphology Analyses of Polished Crystals.....	82
4.3 Structural Characterizations	85
4.3.1 Crystal Orientation Studies with XRD method.....	86
4.3.2 Surface Composition of Crystals with EDX Method.....	89
4.3.3 IR Transmittance Studies	91
4.3.4 Chemical Etching for Defect Characterizations.....	94
4.4 Nano-mechanical Characterizations.....	100
4.5 Subsurface Damage Analyses	104
CONCLUSIONS.....	107
REFERENCES.....	111

LIST OF TABLES

TABLES

Table 2.1 Lattice parameter change with respect to the atom fraction of Zn in $Cd_{1-x}Zn_xTe$ crystal	9
Table 2.2 Band gap of the principle compound semiconductors	12
Table 2.3 Hardness and elastic modulus of different orientation of $Cd_{1-x}Zn_xTe$ crystals	13
Table 2.4 Hardness of abrasive materials at room temperatures	26
Table 3.1 List of dislocation revealing etching	50
Table 4.1 Material Removal Rate of different crystallographic orientations with various size of Al_2O_3 abrasives.....	57
Table 4.2 MRR of polishing processes	61
Table 4.3 TTV of surface preparation processes.....	61
Table 4.4 Optimized Lapping Parameters	62
Table 4.5 Surface profilometer results	67
Table 4.6 Parameters of Mechanical Polishing	71
Table 4.7 Chemo-mechanical polishing optimization study 1	79
Table 4.8 Chemo-mechanical polishing optimization study 2	80
Table 4.9 Composition analyses of $Cd_{0.96}Zn_{0.04}Te$ crystal and inclusion.....	97

TABLE OF FIGURES

FIGURES

Figure 1.1 Main processes of manufacturing CdZnTe crystals.....	3
Figure 1.2 Schematic of Bridgman method and Vertical Gradient Freeze method	5
Figure 2.1 Zinc-blende structure for CdTe-related compounds [18]	8
Figure 2.2 Crystal lattice of $Cd_{1-x}Zn_xTe$ and $Hg_{1-y}Cd_yTe$ crystals.....	9
Figure 2.3 Polar surfaces of $\{111\}$ -oriented fcc crystal [18]	10
Figure 2.4 Schematic representation of load vs displacement data.....	14
Figure 2.5 IR-transmittance of CdZnTe depends on free carrier absorption [2].....	16
Figure 2.6 Different types of IR-transmittance spectrum [15].....	17
Figure 2.7 The atomic configuration of twin formation of fcc crystals	19
Figure 2.8 Different types of dislocations (a) edge dislocation, (b) screw dislocation, and (c) α -edge and β -edge dislocations [42]	20
Figure 2.9 Schematic view of the characteristic shape of etch pits.....	21
Figure 2.10 Plot of the diameter versus density of Te-second phases in CdTe crystal [47]	22
Figure 2.11 Evaluation of Te-inclusions [49]	23
Figure 2.12 Shape evaluation of Te-inclusions under different growth conditions [51]	24
Figure 2.13 Schematic view of lapping system.....	27
Figure 2.14 Parameters and requirements of polishing	30
Figure 2.15 Schematic view of two-body and three-body abrasive wear	32
Figure 3.1 Schematic flow of CdZnTe wafer processing [2]	34
Figure 3.2 MT4 ingot before and after grain reveal etching	35
Figure 3.3 MT7 ingot before and after grain revealing etching	35
Figure 3.4 Orthogonal crystal orientations for fcc	36
Figure 3.5 Slicing trials with twinning method (a),(b) MT2-grown ingot and (c),(d) MT5-grown ingot	37

Figure 3.6 XRD measurement of (a) {111}-oriented (b) {110}-oriented (c) {211}-oriented crystals	38
Figure 3.7 Slicing of MT8-grown ingot with x-ray back reflection method (a) selecting grain, (b) arranging wire, (c),(d) sliced crystals	39
Figure 3.8 Polarity determination for {111}-oriented crystal (a) Cd-terminated face (b) Te-terminated face	41
Figure 3.9 Measured points of thickness variation on CdZnTe crystals	42
Figure 3.10 Schematic view of bonded-interface method.....	51
Figure 4.1 Material Removal Rate Studies with 20 rpm and 30 rpm plate speed (a) 15 μm Al_2O_3 (b) 9 μm Al_2O_3 and (c) 3 μm Al_2O_3	55
Figure 4.2 Atomic density of (100), (110), and (111) planes for fcc crystals.....	57
Figure 4.3 Material removal rate studies for $\text{Cd}_{0.90}\text{Zn}_{0.10}\text{Te}$ and $\text{Cd}_{0.96}\text{Zn}_{0.04}\text{Te}$ crystals with same parameters (a) 15 μm , (b) 9 μm , and (c) 3 μm Al_2O_3 lapping	58
Figure 4.4 Material removal rate for mechanical polishing (a) under different applied load (b) under different slurry concentration.....	60
Figure 4.5 AFM measurement; (a) Surface topography, (b) x-line scan, and (c) y-line scan for 15 μm Al_2O_3 lapped crystal.....	63
Figure 4.6 AFM measurement; (a) Surface topography, (b) x-line scan, and (c) y-line scan for 9 μm Al_2O_3 lapped crystal.....	64
Figure 4.7 AFM measurement; (a) Surface topography, (b) x-line scan, and (c) y-line scan for 3 μm Al_2O_3 lapped crystal.....	65
Figure 4.8 3D topographical images of pits after lapping with (a) 15 μm Al_2O_3 , (b) 9 μm Al_2O_3 , and (c) 3 μm Al_2O_3	66
Figure 4.9 Surface morphology of CdZnTe single crystals with 800x magnification (a) 15 μm lapped, (b) 9 μm lapped and (c) 3 μm lapped	68
Figure 4.10 Cleavages of CdZnTe single crystals with 12000x magnification (a) 15 μm Al_2O_3 lapping, (b) 9 μm Al_2O_3 lapping, and (c) 3 μm Al_2O_3 lapping	70
Figure 4.11 Polyurethane polishing cloth (a) 80x (b) 1500x, and used cloth during (c) mechanical polishing (d) chemo-mechanical polishing.....	72
Figure 4.12 Surface roughness and topography measurements with (a) AFM method and (b) White light interferometer method for 1 μm Al_2O_3 polishing process	73

Figure 4.13 AFM measurement of 1 μm Al_2O_3 polishing process for (a) 20 x 20 μm^2 and (b) 10 x 10 μm^2 surface area	75
Figure 4.14 Surface topography measured with white light interferometer after 0.3 μm Al_2O_3 DIW mixture polishing (a) 15% v/o (b) 7.5% v/o, and (c) CMP with commercial solution	76
Figure 4.15 Material removal rate and roughness value under different 0.3 μm abrasive concentration	78
Figure 4.16 Surface topography of crystals polished with CMP1 (a) 10 minutes (b) 20 minutes	81
Figure 4.17 Optical microscope images of polished samples with (a) 1 μm Al_2O_3 , (b) 0.3 μm Al_2O_3	82
Figure 4.18 SEM images of polished samples with 0.3 μm Al_2O_3 abrasives	83
Figure 4.19 SEM images of chemo-mechanical polishing with modified solution (a) from edge and (b) from the center (c) cleaned surface	85
Figure 4.20 XRD measurements of (211)-oriented as-cut $\text{Cd}_{0.96}\text{Zn}_{0.04}\text{Te}$ slices (a) sliced with twinning method from MT5 (b) sliced with X-ray back reflection method from MT3	87
Figure 4.21 XRD measurements of {111}-sliced crystal after surface treatments	88
Figure 4.22 Left: Atomic Zinc concentration of $\text{Cd}_{0.90}\text{Zn}_{0.10}\text{Te}$ crystal after different surface treatments measured by EDX, Right: The ratio of overall Te to Cd+Zn chemical compositions measured by EDX spectra.....	90
Figure 4.23 Atomic zinc concentration of polished $\text{Cd}_{0.96}\text{Zn}_{0.04}\text{Te}$ crystal from different point on the surface	90
Figure 4.24 IR Transmittance measurements after surface treatments	91
Figure 4.25 IR transmission measurements (a) polished surfaces (b) lapped and grinded surfaces	92
Figure 4.26 IR Transmittance measurements for chemical polishing studies.....	93
Figure 4.27 IR Transmittance and EPD measurements for (a), (c) MT5-grown ingot and (b), (d) MT8- grown ingot	94
Figure 4.28 Inoue etchant applied to different crystallographic orientations (a) {111}-orientation, (b) {211}-orientation, (c) {100}-orientation, and (d) {110}-orientation	96

Figure 4.29 Te inclusion (a) SEM image (b) EDX mapping.....	97
Figure 4.30 Te inclusions decorated with dislocation line from MT5-grown ingot (a) after 0.3 μm Al_2O_3 mechanical polishing (b) after Nakagawa etching.....	98
Figure 4.31 Te inclusions from MT10-grown ingot (a), (b) same Te-inclusion after mechanical polishing and Everson etching (c), (d) same Te-inclusion after chemo-mechanical polishing and Everson etching.....	99
Figure 4.32 Te-inclusion depth analyses (a), (b) after Nakagawa etching to MT5-grown wafer (c), (d) after Everson etching to MT2-grown wafer	100
Figure 4.33 Nano-indenter measurement for {111}-oriented $\text{Cd}_{0.96}\text{Zn}_{0.04}\text{Te}$ crystal (a) Load-displacement curve (b) Hardness and elastic modulus measurements, and (c) Optical microscope images	102
Figure 4.34 Hardness and elastic modulus measurements under different force for (a) {211}-oriented (b){100}-oriented, and (c) {110}-oriented $\text{Cd}_{0.96}\text{Zn}_{0.04}\text{Te}$ crystals.....	103
Figure 4.35 Hardness and elastic modulus measurement for {211}-oriented $\text{Cd}_{0.90}\text{Zn}_{0.10}\text{Te}$ crystal	104
Figure 4.36 Subsurface damages of CdZnTe (a), (b) 9 μm Al_2O_3 lapped and (c), (d) 3 μm Al_2O_3 lapped.....	105
Figure 4.37 Subsurface damages of CdZnTe (a) 1 μm Al_2O_3 polished, (b) 0.3 μm Al_2O_3 polished	106



CHAPTER 1

INTRODUCTION

1.1 Importance of CdZnTe Crystals

Cadmium Zinc Telluride ($\text{Cd}_{1-x}\text{Zn}_x\text{Te}$, CdZnTe) single crystals are one of the most promising materials for room temperature x-ray and gamma-ray detectors. They are also used as substrate materials for epitaxial film growth of Mercury Cadmium Telluride (MCT) which is used for the fabrication of best performing infrared detector arrays. A high quality MCT growth depending on ZnTe mole fraction in CdZnTe [1,2].

Cadmium Telluride (CdTe) related crystals were found to have great potential in x-ray and gamma-ray semiconductor detector applications such as medical imaging systems, homeland security, and also astronomy applications due to their unique material properties [3]. They have large atomic numbers which is the main advantage for larger photoelectric absorption coefficient compared to semiconductor detectors based on germanium (Ge) and Silicon (Si) technology [4]. In addition, CdZnTe radiation detectors have room temperature operability owing to their higher resistivity ($> 10^8 \Omega\cdot\text{cm}$) and wide band gap between 1.4eV and 2.26eV; while the traditional high performance detectors need liquid-nitrogen cooling systems [5,6].

$\text{Hg}_{1-y}\text{Cd}_y\text{Te}$ is one of the most important material for infrared detector technology because of its excellent performance both in mid wavelength infrared (MWIR) and long wavelength infrared (LWIR) region between 2-14 μm ranges [2]. HgCdTe infrared detectors were first synthesized nearly fifty years ago, upon the first investigation of this material properties such as direct band gap with high absorption coefficient, moderate thermal coefficient of expansion, etc. [7,8]. High quality and defect free bulk growth of

HgCdTe is highly difficult because of the high vapor pressure of Hg; so that bulk growth has been replaced with epitaxial film growth which requires suitable substrates. In mid 1970s, CdTe large size single crystals were used as substrate materials because of their good optical properties such as high infrared transmission in both LWIR and MWIR regions. However, CdTe crystals have a few percent of lattice mismatch with HgCdTe causing formation of undesirable defects and rougher surfaces in the epitaxial grown HgCdTe layer. In order to adjust the lattice parameter of CdTe to match HgCdTe, a few percent of ZnTe have been added and then $Cd_{1-x}Zn_xTe$ has been used as substrate for epitaxial film growth of HgCdTe where x value is nearly 0.04. Comparing the lattice parameters of $Hg_{0.77}Cd_{0.23}Te$ versus $Cd_{0.96}Zn_{0.04}Te$ and others, CdZnTe is almost perfectly matching rather than CdTe, Si, and GaAs for a good epitaxial growth [2]. For a high quality MCT epilayer growth, it is important to have high quality substrate in terms of defect density and uniformity of Zn concentration [9]. Furthermore, MBE growth technology requires high-quality surfaces in terms of surface roughness, flatness, and orientation accuracy [8,9].

1.2 Manufacturing of CdZnTe Crystals

In spite of difficulties in growing high quality bulk crystal, CdZnTe crystal has been the dominating material for X-ray and Gamma-ray detector applications and substrate for epitaxial growth of HgCdTe for infrared applications. The main difficulty of bulk growth of CdZnTe is to be able to obtain large-volume single crystals with low-defect density due to higher thermal conductivity, ease of twin formation, controlling stoichiometry and Zn segregation [10].

Wafering processes are as critical as the bulk growth processes. Radiation detector performance in terms of resolution and detector signal to noise ratio depends not only the bulk material quality, but also on the CdZnTe surface quality [1,11]. Surface quality plays a critical role for HgCdTe detector performance because any kind of damage and defects (scratches, cracks, inclusions, and dislocations) on CdZnTe substrate surface are directly

transferred to the HgCdTe epilayer. Epitaxial growth technology requires high crystal quality, ultra flat surface with sub-nanometer roughness [12].

Many research groups have focused on CdZnTe bulk growth from liquid phase since the first synthesis of CdZnTe. Various growth techniques such as Bridgman method, vertical gradient freeze (VGF), and travelling heater method (THM) have been developed [4,10,13].

The main processes in manufacturing of CdZnTe wafers are shown in **Figure 1.1**.

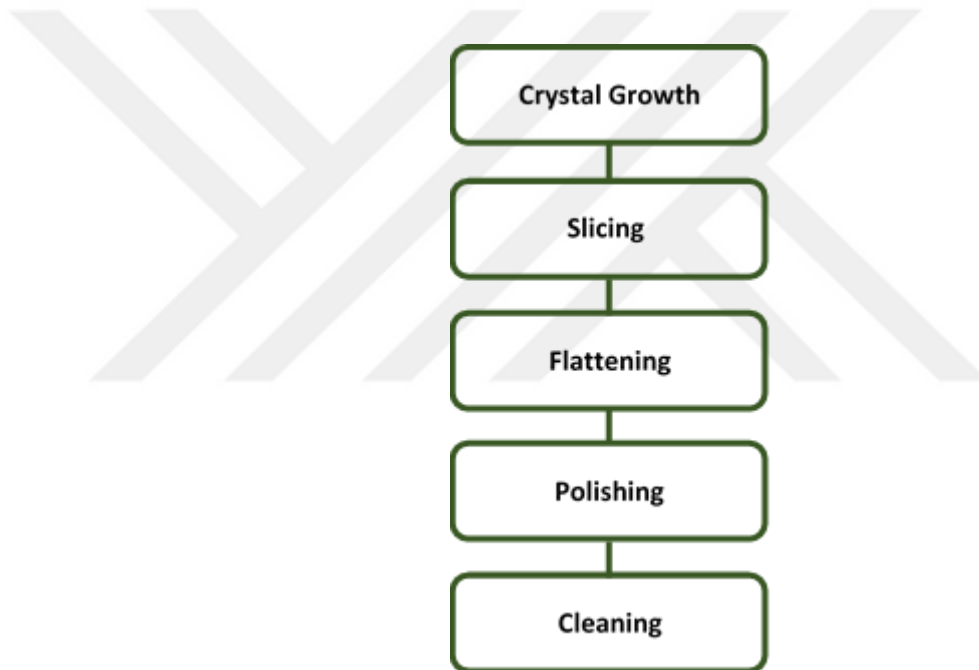


Figure 1.1 Main processes of manufacturing CdZnTe crystals

Following the first successful growth of CdTe in 1978, CdZnTe crystals were grown primarily by Bridgman method in which the starting elemental materials (Cd, Zn, Te) inside a crucible is moved slowly under an axial temperature gradient (**Figure 1.2**) [13]. Since vapor pressure of Te is much lower than that of Cd, a sealed quartz crucible is used to prevent evaporation of Cd. In Bridgman method, elements are homogenized by melting at high temperatures (nearly 1100°C) and finally crystallization is started slowly with a few mm/h growth rate from the lower end. Both vertical and horizontal systems with proper pressure conditions have been designed and manufactured [10]. The major

disadvantage of the Bridgman method is the (i.e. thermal stress) movement of large amount of melt material inside the crucible [4].

In order to eliminate the temperature variation due to the movement of the crucible, Vertical Gradient Freeze (VGF) method has been developed. In this method, the crucible is kept stationary while the control of the temperature is achieved by computer programming of a multi zone system (**Figure 1.2**) [14]. Temperature distribution for melting of materials is controlled by computer programming in multi-zone furnace that achieve A good temperature stability and a well-controlled temperature profile is then obtained [4,16]. VGF method allows high precision in controlling the melt/solid interface, which is absolutely necessary to produce large crystal domain in the grown ingot. In the growth processes, the charge (could be elemental or component) is loaded inside the closed crucible as in the Bridgman method. It is melted and soaked for several hours at higher temperatures, nearly 1115°C for CdZnTe, for homogenization. The melt is then cooled down for nucleation under a certain temperature gradient (a few degree per cm). Solidification is initialized from one end of the crystal and it is the lower end in vertical gradient freeze configuration. Once the solidification starts, solid-liquid growth interface is moved to the upper body of the melt crystal using electronically controlled temperature gradient until the melt becomes completely solid at the tail end. The grown ingot is thereafter cooled down to room temperature with a proper cooling rate (a few tens degrees per hour) to control defect mechanism throughout the crystal.

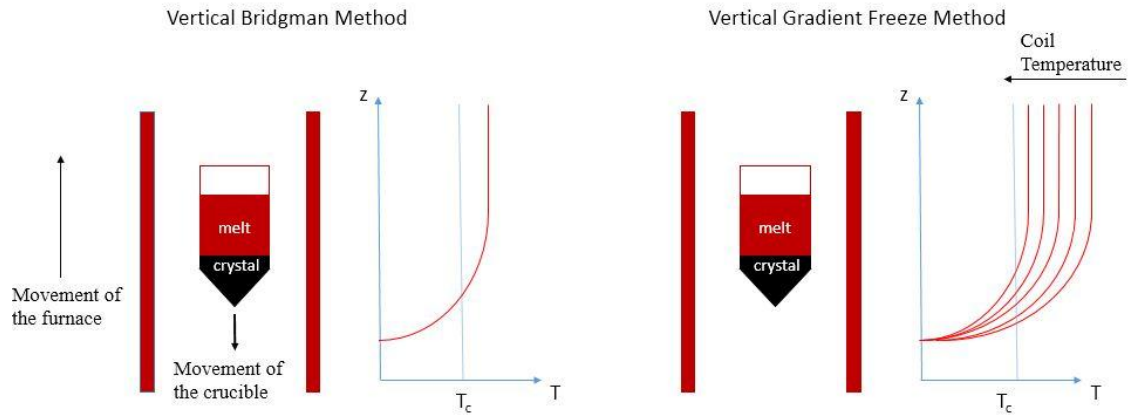


Figure 1.2 Schematic of Bridgman method and Vertical Gradient Freeze method

A series of delicate processes such as slicing/dicing, flattening, polishing and cleaning has to be carried out in order to transform the ingot to wafers which are the main study of semiconductor technologies. Thanks to the silicon wafering technology which has provided basic knowledge and methodology for the fabrication of high quality CdZnTe wafers [2]. However, difficulties still arise during the surface finishing of CdZnTe crystals due to their soft-brittle nature.

Slicing of CdZnTe crystals in a specific orientation is one of the challenging processes. Perfectly {111}- and {211}-oriented crystals are preferred for HgCdTe epitaxial growth since crystallographic misorientation has deleterious effects on epitaxial layers. Wire-cutter or dicer are commonly employed for the slicing process. Because of the multi-crystal nature of the grown ingot, extracting single crystal grains from the ingot (called grain mining) is critical in the process yield and the number which is important for the cost of the final product.

Sliced crystals from the ingot slices cut from the ingot with different dimensions depending on grain size and depth are lapped/grinded to remove the damage on the surface and at the subsurface. A relatively flat surface and desired wafer thickness are obtained after the lapping/grinding process.

Mechanical polishing and chemo-mechanical polishing are then applied to improve surface quality and remove subsurface damaged formed during the lapping/grinding process. At this stage chemical treatments play an important role in reaching a good flatness at sub nanometer level [16].

Finally, wafers are cleaned and packed for characterization.

1.3 Outline of the Thesis

In this thesis, manufacturing of single crystal CdZnTe from ingot to wafer and characterization of surface preparation of the CdZnTe wafers during and after the whole process chain were deeply studied. The outline of the thesis and the main objectives are given below:

- Chapter 1 gives a short summary of the importance of CdZnTe crystals for the two main applications and manufacturing studies.
- Chapter 2 presents the crystal properties of CdZnTe and the theory of surface preparation techniques.
- Chapter 3 covers the experimental details of surface finishing studies. Slicing experiments are explained in detail. Lapping and polishing studies are provided subsequently in each section. Material Removal Rate (MRR) studies are also investigated. Characterization techniques are presented in this chapter.
- Chapter 4 focuses on the results and detailed discussion of experimental results. MRR studies of crystal machining processes conducted on CdZnTe wafers having different crystallographic orientations are given in this chapter. Characterization of wafering studies in terms of surface, structural, and optical properties are presented.
- In the last chapter, Chapter 5, general conclusions drawn from this thesis as well as possible future studies are provided.

CHAPTER 2

THEORY

In this chapter, general information about CdZnTe crystals are given and theory of surface finishing studies are described. Main properties of CdZnTe crystals are explained in Section 2.1. Crystalline defects that affect the crystal quality are given in Section 2.2. Finally, theory of surface preparation studies and material removal mechanisms of each step is described in Section 2.3.

2.1 Properties of CdZnTe

2.1.1 Crystal Structure

$\text{Cd}_{1-x}\text{Zn}_x\text{Te}$ crystals have zinc-blende (or sphalerite) crystal structure from $F\bar{4}3m$ cubic space group [17]. This crystal structure consists of two interpenetrating face-centered-cubic (fcc) Bravais lattice, that are occupied by metallic (Cd or Zn) and non-metallic (Te) atoms (**Figure 2.1**). One sublattice comprises of only cations (Cd^{+2} or Zn^{+2}) and the other only anions (Te^{-2}). All atoms in the crystal lattice are identical.

The Bravais lattice consists of Cd-Te pair displaced from one another $\frac{1}{4}$ bond length distance along the (111) direction [18]. Cd and Te atoms are dispersed over close-packed planes (i.e. {111} planes).

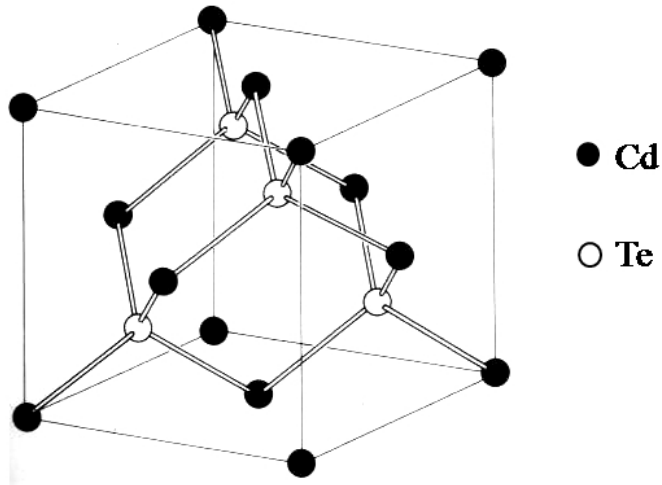


Figure 2.1 Zinc-blende structure for CdTe-related compounds [18]

Each atom shares its four neighbor-hetero atoms; thus structure form as covalent bonding [9]. Te atoms are surrounded by 4 Cd atoms (**Figure 2.1**). The covalent bonding between Cd and Te plays an important role on ionicity that is 0.55 for Cd-Te which is one of the highest in II-VI semiconductors [19].

$\text{Cd}_{1-x}\text{Zn}_x\text{Te}$ crystals can be described as a CdTe crystal with Zn atoms randomly substituting the Cd atoms in the fraction of x . Lattice constants of $\text{Cd}_{1-x}\text{Zn}_x\text{Te}$ are calculated by Vegard's law (**Equation 2.1**) [20]. In the equation, a is the lattice parameters of compounds.

Equation 2.1
$$a_{\text{Cd}_{1-x}\text{Zn}_x\text{Te}} = (1 - x)a_{\text{CdTe}} + (x)a_{\text{ZnTe}}$$

At room temperature, lattice parameters of CdTe and ZnTe are 6.481 Å and 6.1037 Å, respectively. Lattice parameters depend on zinc mole fraction (**Table 2.1**).

Table 2.1 Lattice parameter change with respect to the atom fraction of Zn in $\text{Cd}_{1-x}\text{Zn}_x\text{Te}$ crystal

Compounds of $\text{Cd}_{1-x}\text{Zn}_x\text{Te}$	Lattice parameters (Å)
CdTe	6.481
ZnTe	6.1037
HgTe	6.46
$\text{Cd}_{0.96}\text{Zn}_{0.04}\text{Te}$	6.466
$\text{Cd}_{0.90}\text{Zn}_{0.10}\text{Te}$	6.443
HgCdTe	6.466

Addition of Zinc into the CdTe crystal lead to decreasing of lattice parameter since Zn atoms have smaller atomic radius than Cd atoms.

Lattice constant of $\text{Cd}_{0.96}\text{Zn}_{0.04}\text{Te}$ is highly vital for epilayer growth of HgCdTe. Comparing to high lattice mismatch crystals (CdTe, Si, and GaAs), $\text{Cd}_{0.96}\text{Zn}_{0.04}\text{Te}$ crystals have perfect lattice match with $\text{Hg}_{0.77}\text{Cd}_{0.23}\text{Te}$ (**Figure 2.2**).

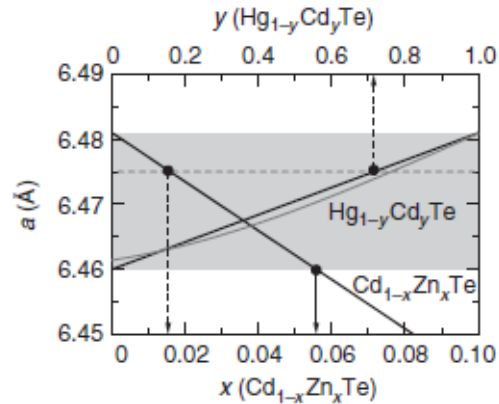


Figure 2.2 Crystal lattice of $\text{Cd}_{1-x}\text{Zn}_x\text{Te}$ and $\text{Hg}_{1-y}\text{Cd}_y\text{Te}$ crystals

2.1.2 Polarity of CdZnTe Crystals

CdZnTe crystals have four fold roto-inversion axis, one three-fold rotation axis, and mirror plane called $F\bar{4}3m$. CdZnTe crystals have no center symmetry; therefore, the crystal structure has exhibited crystallographic polarity. Opposite crystallographic planes, (hkl) and $(\bar{h}\bar{k}\bar{l})$, have different structural, chemical and crystal growth behaviors [21].

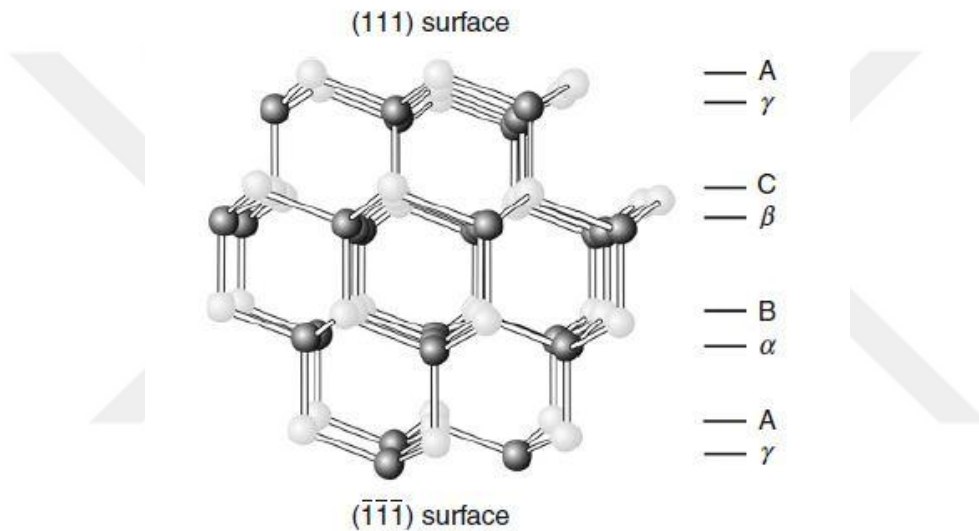


Figure 2.3 Polar surfaces of $\{111\}$ -oriented fcc crystal [18]

One of the clearest example of crystallographic polarity is seen on $\{111\}$ surfaces of zinc-blende structure. In the composition of fcc, Roman letter id used to symbolize metal atoms (Cd (or Zn for CdZnTe) and Greek letter is used to denote non-metal atoms (Te). (111) and $(\bar{1}\bar{1}\bar{1})$ surfaces are terminated by one type of atom (Cd or Te). In **Figure 2.3** (111) surface is terminated with Cd atoms and opposite face is terminated with Te atoms. The surfaces can be described as $\{111\}Cd$ and $\{\bar{1}\bar{1}\bar{1}\}Te$. It is suggested that white circles are called A (alabaster) element and black circles are called B (black) for ball and stick diagram as shown in **Figure 2.3** [21]. For CdTe-related compounds, A-terminated Cd surface is described as $\{111\}A$ and B-terminated Te surface is described as $\{\bar{1}\bar{1}\bar{1}\}B$ [18].

Earliest studies showed that (111)A surface is less chemically reactive than (111)B surface for zinc-blende III-V materials [22,23]. Due to more reactivity, $\{\bar{1}\bar{1}\bar{1}\}$ B surface is dissolved in oxidizing agents more rapidly and chemical etching is attached to $\{\bar{1}\bar{1}\bar{1}\}$ B surface faster than {111}A face. Differences in etch pit formations is also investigated for different polarities [23]. Besides, epitaxial growth and some mechanical properties such as subsurface damage depth, strain, and nano-hardness depend on polarity of the surface.

Polarity of any surface can be determined by the polarity index formula [21] that is given as;

Equation 2.2
$$P = \frac{n_A - n_B}{n_T}$$

Here; n_A , n_B , and n_T are the number of A atoms, B atoms, and total atoms, respectively. Polar index $P=1$ or -1 shows opposite polarities of fully polar faces such as {111}A and $\{\bar{1}\bar{1}\bar{1}\}$ B faces. Beside this orientation, {211} surfaces also shows polarity. From this equation, Polarity indexes of {110} and {100} surfaces are zero ($P=0$). These surfaces are known to be non-polar.

In order to reveal A and B surfaces, chemical etchants are commonly used [24]. One of most effective etchant is Brown etchant involved HF:HNO₃:lactic acid (1:1:1 v/o) or HF:HNO₃:acetic acid (1:1:1 v/o) [24,25]. These etchants leave a matt-black surface on {111}A face and a bright-shiny surface on $\{\bar{1}\bar{1}\bar{1}\}$ B face.

2.1.3 Band Structure

CdTe and ZnTe semiconductors have direct band gap structures at $k=0$ at room temperature. Band gap of CdTe and ZnTe are 1.54 eV and 2.26 eV, respectively [18]. Band gap of Cd_{1-x}Zn_xTe crystals are changed by adding Zn into CdTe. Growth of compound semiconductor with wide range of band gap, atomic number, and density proper an important advantage for almost all applications [20]. Comparing with traditional semiconductors, Cd_{1-x}Zn_xTe crystals have wide band gap at room temperature (**Table 2.2**).

Table 2.2 Band gap of the principle compound semiconductors

Material	Band Gap (eV)
Si	1.17
Ge	0.67
GaAs	1.52
Cd _{0.96} Zn _{0.04} Te	1.56
Cd _{0.90} Zn _{0.10} Te	1.59

Band gap of Cd_{1-x}Zn_xTe crystals can be calculated from **Equation 2.3** where c is “bowing parameter” and nearly 0.27 at room temperature [10]. Increasing additional Zn in CdTe compound leads to increase band gap of the CdZnTe material and therefore more energy is required to generate an electron-hole pair.

Equation 2.3
$$E_g(Cd_{1-x}Zn_xTe) = xE_g(ZnTe) + (1 - x)E_g(CdTe) - cx(x - 1)$$

2.1.4 Mechanical Properties

Mechanical behaviors of crystals play a critical role in the growth and surface processing. Dislocation formation during solidification depend on residual stress and strain on CdTe; hence, they should be known. Residual stress in the crystal affects the physical properties of Cd_{1-x}Zn_xTe crystals [26]. Residual stresses of CdZnTe crystals are measured as $\tau_{12}=-4$ MPa (shear stress) and $\sigma_1=30$ MPa, and $\sigma_2=14$ MPa (axial stresses) [19].

Hardness and dislocation energies are related inversely [27]. Addition of Zn into CdTe weakens the crystal lattice since Cd-Te ionicity is higher than Zn-Te ionicity. Zn-Te bond energy is lower, defect energy formation is higher and these cause lower dislocation density. Hardness of CdZnTe crystals are decreased by addition of Zn due to shorter bond length between Zn and Te atoms [16].

CdZnTe crystals have soft-brittle nature. Since CdZnTe crystals have anisotropic structure, surface finishing studies in terms of material removal rate and surface roughness

are related to the orientation of crystals [28]. Crystal machining and surface damages are correlated with nano-mechanical behaviors of crystallographic orientations. Hence, it is necessary to know nano-mechanical properties of CdZnTe. Nano-hardness and elastic modulus of Cd_{1-x}Zn_xTe crystals were measured by different researchers [11,29]. Hardness are measured by Oliver and Pharr method [30].

Equation 2.4
$$H = \frac{P_{max}}{A_c}$$

In the **Equation 2.4** H is the hardness, P_{max} is the maximum applied load, and A_c is contact area. Young's modulus (Elastic modulus) can be calculated by **Equation 2.5** where E and v are the Young's modulus and Poisson's ratio for the crystal and E_i and v_i are the same parameters of Berkovich indenter.

Equation 2.5
$$\frac{1-v^2}{E} = \frac{1}{E_r} - \frac{1-v_i^2}{E_i}$$

E_r is the reduced modulus and it can be measured from stiffness of crystal (**Equation 2.6**).

Equation 2.6
$$S = \frac{dP}{dh} = \frac{2}{\pi} E_r \sqrt{A}$$

Table 2.3 Hardness and elastic modulus of different orientation of Cd_{1-x}Zn_xTe crystals

Crystal	Orientation	Hardness (GPa)	Elastic Modulus (GPa)
Cd _{0.90} Zn _{0.10} Te	{111}	1.19	43.4
Cd _{0.96} Zn _{0.04} Te	{111}	1.21	42.5
Cd _{0.96} Zn _{0.04} Te	{110}	1.02	44.0

shows that hardness of {111} oriented Cd_{0.90}Zn_{0.10}Te crystals is lower than that of {111}-oriented Cd_{0.96}Zn_{0.04}Te crystals due to additional Zn. Zhang et al. have measured that {111}-oriented Cd_{0.96}Zn_{0.04}Te crystal has higher hardness than {110}-oriented Cd_{0.96}Zn_{0.04}Te crystal since {110} surface has less atoms than {111} surface [11]

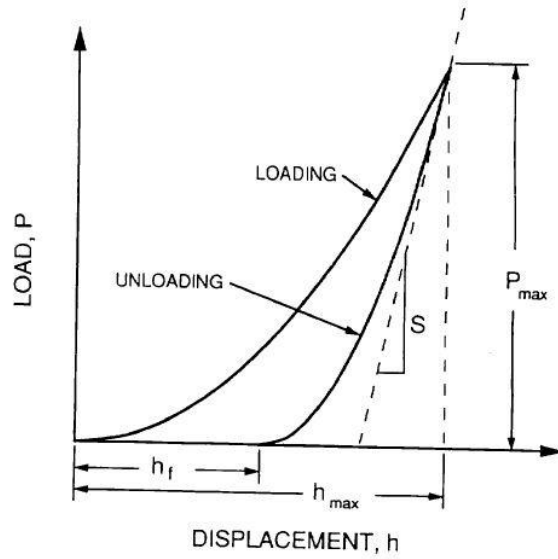


Figure 2.4 Schematic representation of load vs displacement data

2.1.5 Optical Properties

Optical transmission of crystals provides useful information about quality of growth and surface studies. In order to characterize optical properties of CdTe-related compounds, Infrared (IR) transmittance measurements are crucial [31]. IR-transmittance of crystals are directly related to the crystalline imperfections. General formula for the Infrared transmission (T) is given in **Equation 2.7** where R is the reflectivity of the surface, α is the absorption coefficient, and d is the thickness of sample [32]

Equation 2.7

$$T = \frac{(1-R)^2 e^{-\alpha d}}{1-R^2 e^{-2\alpha d}}$$

Reflectivity of the CdTe samples can be calculated from **Equation 2.8**, where n is reflective index, since real part of the complex reflection is larger than imaginary part due to wide band gap of CdTe-related compound.

Equation 2.8

$$R = \frac{(n-1)^2}{(n+1)^2}$$

Solving the **Equation 2.7** and **Equation 2.8**, absorption coefficient α can be calculated from **Equation 2.9** where T_{\max} is the maximum degree of transmittance (T) in every spectrum.

Equation 2.9

$$\alpha = \frac{1}{d} \ln \frac{(1-R)^2 + \sqrt{(1-R)^4 + 4T_{\max}^2 R^2}}{2T}$$

Theoretical IR-transmittance value for CdZnTe is around 66% in the 2-20 μm wavelength range at room temperature [33]. Te-rich regions are the main source of degrading for the IR transmission of CdZnTe crystals. Decreasing of IR-transmittance at shorter wavelengths is a result of scattering of precipitates; whereas, free carrier absorption dominates the decreasing of IR-transmission at higher wavelengths [2].

Te precipitates and Te inclusions exist in CdZnTe crystals as Te-rich phases. Te-rich CdZnTe crystals present p-type behavior and p-type ingots have lower IR-transmittance because of higher carrier concentration. Cd-rich CdZnTe crystals show n-type behavior and have higher IR-transmittance due to lower carrier concentration [10].

IR-transmittance spectrum decreases with increasing free carrier absorption (**Figure 2.5**). Free carrier absorption is seen in heavily doped semiconductors where Fermi energy is closed to conductive band and materials are prone to high free carrier concentration. When free carrier concentration is around $3 \times 10^{15} \text{ cm}^{-3}$, the effect of free carrier absorption can be seen very clearly in CdZnTe crystals [34].

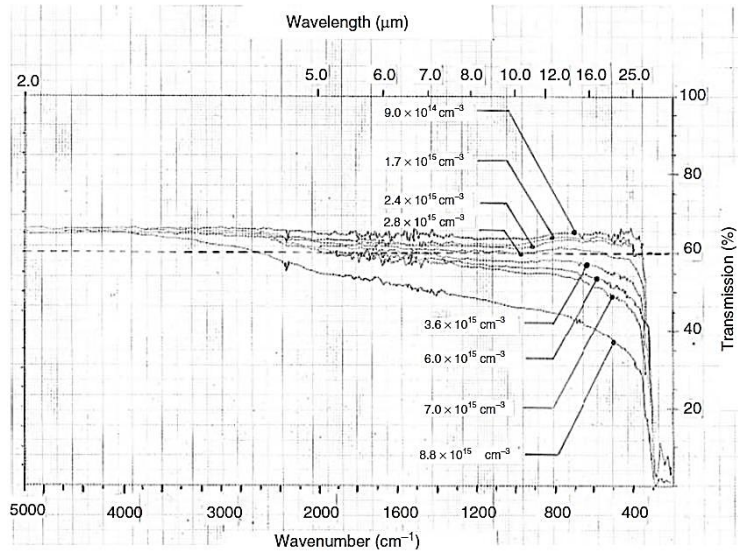


Figure 2.5 IR-transmittance of CdZnTe depends on free carrier absorption [2]

Li et al. showed four types of IR-transmittance spectrum for CdZnTe crystals [35]. These types are correlated with the quality of crystals. Crystals with high dislocation density have descending type (a), low resistive crystals have ascending-type spectrum (b), crystals with high dislocation density and low resistivity have low-straight type (c), and crystals with low dislocation density and high resistivity have high-straight type IR-transmittance spectrum (d) as shown **Figure 2.6**.

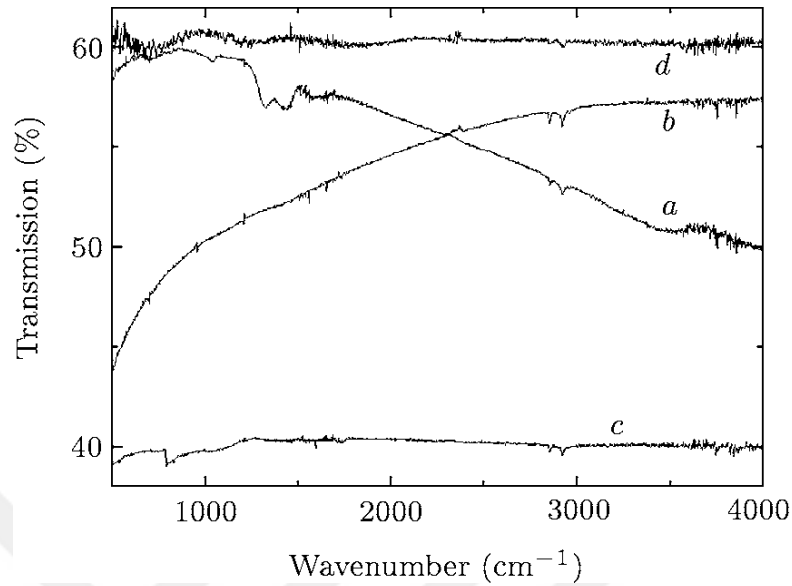


Figure 2.6 Different types of IR-transmittance spectrum [15]

2.2 Crystalline Defects in CdZnTe

2.2.1 Grains and Grain Boundaries

Grain is an individual crystal having specific crystal orientation in metals or semiconductors. Grains are produced during the cooling of crystal growth by high growth rates, high temperature gradients or may also be a result of the growth convection [15]. Grain boundaries divide the crystal surface two or more crystal volume that have different crystallographic orientation. Grains and phase boundaries are two-dimensional defects that are formed due to non-equilibrium thermodynamics [36].

Grain boundaries can form at the beginning of crystal growth when nucleation of grains occurs or they may form by instabilities at the growth interface. Grain boundaries degrade CdZnTe detector performance in terms of thermal conductivity and electrical properties. High concentration of dislocations and impurities are placed at the grain boundaries [9].

CdZnTe crystals are grown generally polycrystalline. Grain boundaries in CdZnTe ingots are one of the main problems selecting (mining) single oriented wafers due to decreasing

the single crystal yield. Generally, grain size of CdZnTe crystals about a few centimeters are acceptable to use as X-ray and gamma-ray detectors and substrate for IR detectors.

2.2.2 Twins

Twins are defined as specific oriented grains having symmetric crystallographic relation to their host grain. Largest grain in a twin formation on it is called as ‘host’, ‘parent’ or ‘matrix’ grain. Twin formations form in the crystal along minimum energy orientations. {111} planes have the largest atomic density and interplane spacing; moreover, {111} planes have the weakest interactional force [37]. Hence, for cubic systems (like fcc) twin planes usually lie on {111} face in order to satisfy low boundary energy [18] Twin boundaries are internal surfaces between the twin plane and the host plane having the lowest energy [38].

Twins are generally formed by temperature fluctuation during cooling of crystal growth with low stacking fault energy ($11 \times 10^{-7} \text{ J cm}^2$) [36]. Misorientation of atoms because of unstable solid-liquid interface or thermal stress at higher temperature introduce twins and twin boundaries [39]. Some parameters of crystal growth can also cause twinning such as crucible wall, rotation of crucible etc. Twin formations are classified as stress induced twins and growth twins. Stress induced twins are evaluated by slipping of dislocations under deformation stress. Crystalline energy and stacking fault energy change when partial dislocation nucleate and slip on the plane [40]. Interaction between crucible and crystal and temperature change during crystal growth are caused growth twins.

Twins are shifted {111} planes with a Burgers vector $\frac{a}{6} \langle 112 \rangle$ without any wrong bonds. When the atoms are shifted, stacking sequence change from ...A α -B β -C γ -A α -B β -C γ -A α -B β -C γ ... to twin stacking sequence ...A α -B β -C γ -A α -C β -A γ -C α -B β -A γ ... to sustain mirror symmetry (**Figure 2.7**).

Twinning in CdZnTe crystals can be identified as rotation of the lattice by 180° about {111} orientation. Micro-twin formations having few atomic layers to cm size occur in a

group of 3-6 twins parallel to each other [37]. Twin formations degrade the electrical properties of CdZnTe crystals and thus, performance of detectors [33].

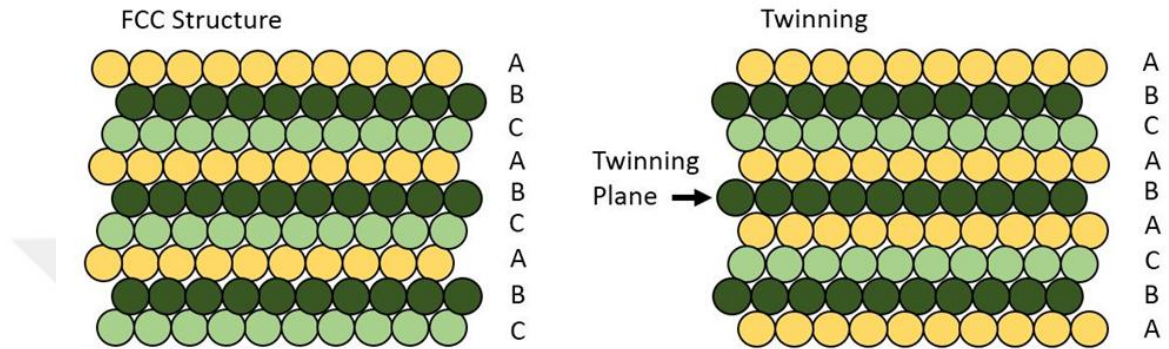


Figure 2.7 The atomic configuration of twin formation of fcc crystals

2.2.3 Dislocations

Dislocations are known as irregularities of atoms in crystals structure. Dislocations are produced during crystal growth due thermo-mechanical stresses caused by interaction between required temperature for bulk growth [9,41]. Many types of dislocations can be formed in CdZnTe crystals such as edge, screw, Cd (α), and Te (β) dislocations.

Edge and screw dislocations are dislocation lines that related with Burgers vector [42]. Atoms around slip plane can move through dislocation lines leading to disorder in the crystal lattice. If Burger vector and the dislocation line are perpendicular to each other, it is called an edge dislocations (**Figure 2.8a**). If Burger vector and the dislocation line are parallel to each other, a screw dislocations form (**Figure 2.8b**). The length of dislocation lines are tenths of microns [41].

α (Cd) and β (Te) dislocations are 60° edge dislocations produced along $\{111\} \langle 110 \rangle$ slip systems due to crystallographic polarity of CdZnTe crystals [43]. α and β dislocations can be described as extra plane of atoms [18]. If extra planes are terminated at the slip plane

of cations (Cd), it is called α -edge dislocation and β -edge dislocation has an extra plane that terminate at the anion atoms (Te) (**Figure 2.8c**).

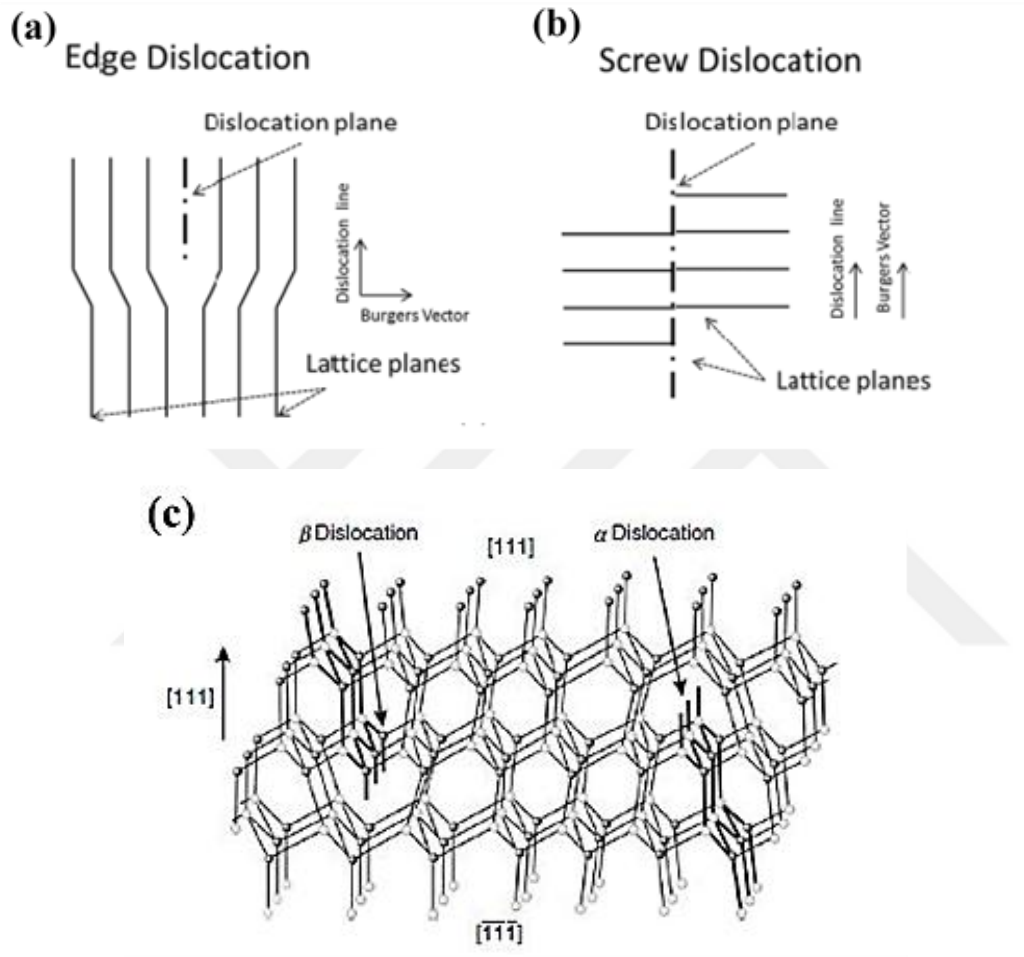


Figure 2.8 Different types of dislocations (a) edge dislocation, (b) screw dislocation, and (c) α -edge and β -edge dislocations [42]

Density of all type dislocations can be characterized by etch pit density (EPD) method. Chemical etchings are used to reveal etch pits on the surface. This technique is an important method to identify growth and surface quality. Inoue [44], Nakagawa [45], and Everson [46] etchants are mainly used to reveal dislocations.

Inoue introduced chemical polishing solutions (E- and P-solutions) to obtain mirror like surfaces and chemical etching solutions (EAg-1 and EAg-2) to reveal all kinds of

dislocations. Etch pits of $\{111\}$, $\{110\}$, and $\{100\}$ surfaces have different characteristic shapes. Shape of dislocation etch pits are associated with Thomson's tetrahedron in real space (**Figure 2.9**). Chemical etching of $\{111\}$ -oriented crystals have equilateral triangle, $\{110\}$ -oriented crystals have isosceles triangle with 70.6° apical angle, and $\{100\}$ -oriented crystals have rectangular shape etch pits [44].

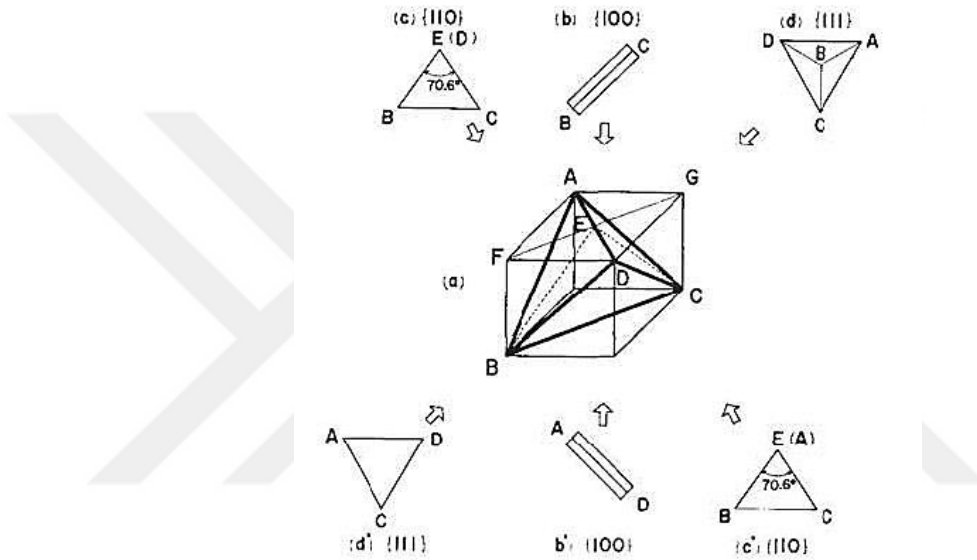


Figure 2.9 Schematic view of the characteristic shape of etch pits

In order to reveal fresh dislocations on CdTe crystal surfaces, Nakagawa developed a solution that is completely different than E-Ag reagent that not capable to reveal fresh dislocations [45]. Nakagawa etching is used to reveal dislocations on $\{111\}$ -oriented polished surfaces.

Everson was introduced a new etchant to reveal dislocations on B side of $\{111\}$ - and $\{211\}$ - oriented CdTe-related compounds [46]. Everson etching produces pits on $(111)B$ and $(211)B$ face of CdZnTe. This etch produces equilateral triangles on $(111)B$ surface and elongated triangles on $(211)B$ surface with 10:1 width:depth ratio that can be seen unaided eye.

2.2.4 Te Inclusions

Te-inclusions are formed due to the difference of thermal expansion between Te and CdZnTe matrix. CdTe-related compounds are prone to become Te-rich at high temperature during crystal growth due to Cd overpressure [18]. Morphological instabilities at the crystallization layer are the result of Te-rich melts. Te-rich droplets of CdZnTe are captured from Te-rich diffusion layer at the interface caused originating of Te-inclusions. Relation of growth rates and temperature gradients at solid-liquid interface cause the emergence of Te-inclusions.

Cd loss and Te enrichment cause two phases with different size and density *i.* appearance of Te inclusions ($\geq 1 \mu\text{m}$ in diameter, low density of Te particles) and *ii.* emergence of Te precipitates (size between 0.01 and 0.1 μm in diameter, high density of Te particles) (Figure 2.10)

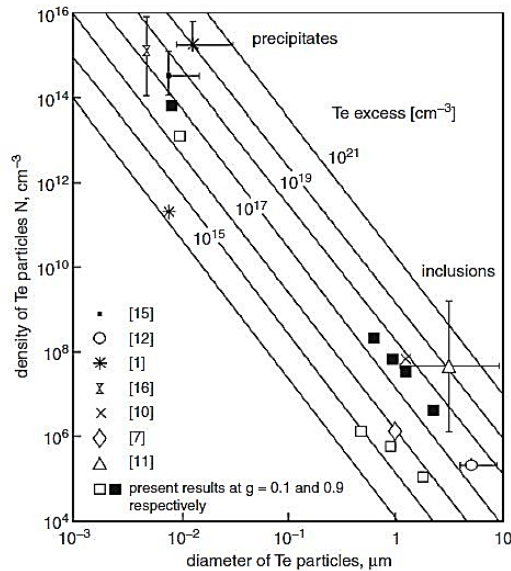


Figure 2.10 Plot of the diameter versus density of Te-second phases in CdTe crystal

[47]

Te-inclusions can decorate with other crystallographic defects in lattice. Dislocations, twins and grain boundaries can be decorated by Te-inclusion [48]. High density of second phase inclusions may induce extended defects such as dislocations, i.e. surrounding by etch pit roseate and gliding patterns [49,50]. Te decorated with dislocations on {111} surface with $\langle 110 \rangle$ direction of glide propagation is shown in **Figure 2.11**.

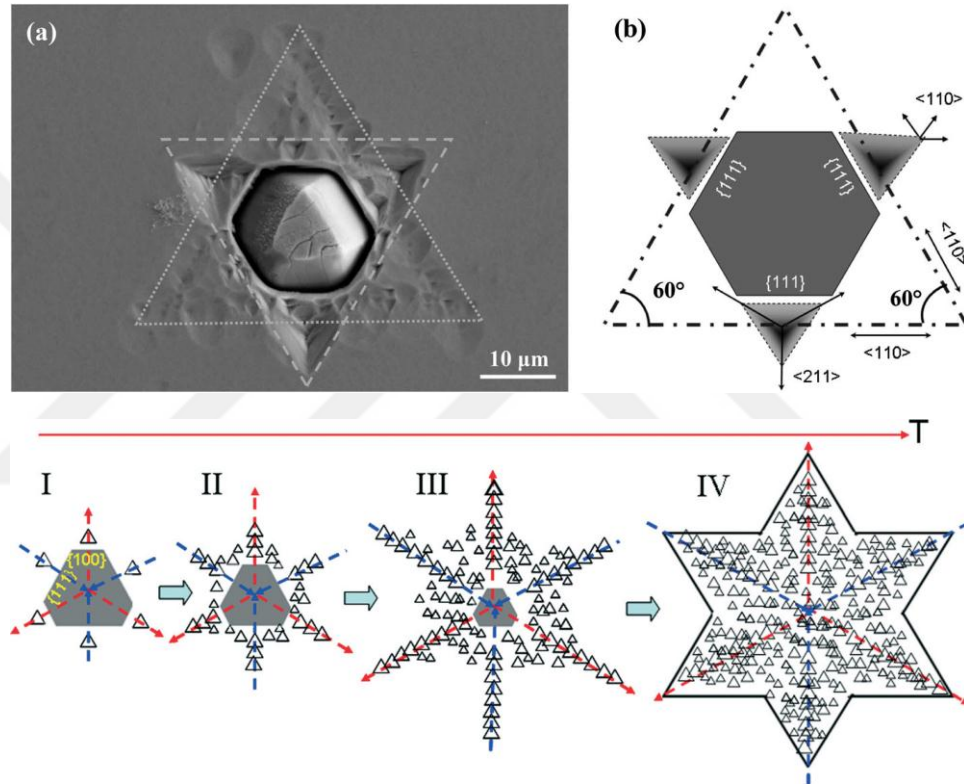


Figure 2.11 Evaluation of Te-inclusions [49]

Morphology of Te-inclusions changes under different growth conditions and depends on the polarity of the surface. Final shape of Te-inclusions completely changes from the beginning of their morphology. He et al. represented morphology evaluation of Te-inclusions in CdZnTe crystals [51]. Shape of the inclusions may be formed due to cooling rate. Larger cooling rate ($\geq 50 \text{ Kh}^{-1}$) keep their shape as **Figure 2.12a-b** and slow cooling rate Te inclusions keep their shape as **Figure 2.12c-f**. In CdZnTe crystals, triangular and hexagonal shape of Te-inclusions with 1-2 μm diameter up to 10-20 μm [52].

Second phase inclusions degrade the optical mechanical and electrical properties of CdZnTe crystals. Larger dimension inclusions distort the electrical field and increase the leakage current; hence, presence of inclusions decrease the energy resolution of the detector [9,53]. Density of Te inclusions effect the infrared transmission of CdZnTe crystals [48]. Large size Te inclusions have strong infrared absorption caused reducing of infrared transmission.

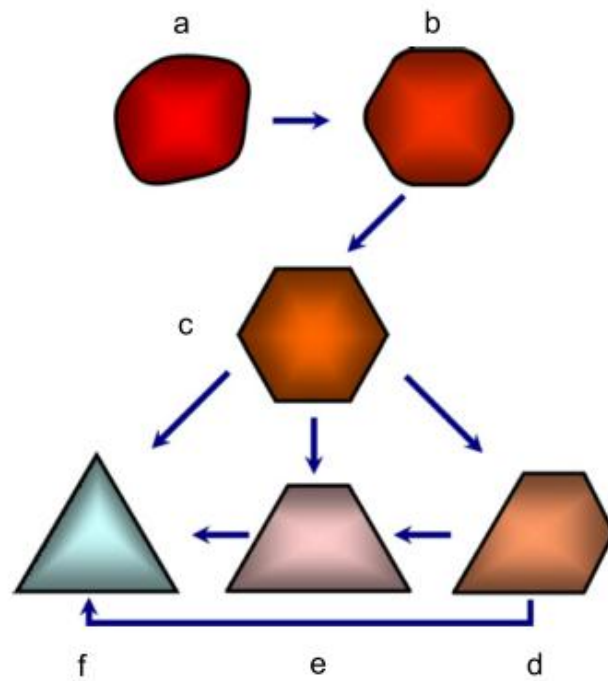


Figure 2.12 Shape evaluation of Te-inclusions under different growth conditions [51]

2.3 Theory of Surface Finishing Studies

CdZnTe crystals are the most promising materials for room-temperature detectors and substrates for epitaxial growth of HgCdTe for IR detectors [54]. Both applications demand high surface quality in terms of surface roughness, orientation accuracy, flatness, and favorable thickness [8]. These factors are getting important for high resolution detector performance. Hence, wafering studies (ingot to wafer) need state-of-the-art technology.

To improve the quality of CdZnTe, crystal machining steps should be well understood. Lapping, mechanical polishing (MP), and chemo-mechanical polishing (CMP) are known crystal machining processes for semiconductors [7,12,54].

Both lapping and polishing are abrasive based processes that have been employed in semiconductor fabrication for more than 100 years. Lapping and polishing methods remove the materials with free abrasives that are easily embedded on the surface and hard to remove. These methods are different than traditional crystal machining processes such as grinding, milling, drilling etc., due to free abrasive particles. These traditional methods end up with the fracture of brittle materials due to micro vibrating of machines [55].

The aim of lapping and polishing is to achieve high orientation accuracy and flatness and to obtain minimum surface and subsurface damage. These are very similar machining processes that workpiece and rotating plate contact and removed material by fraction of abrasives. Differences of both processes lie on the material removal mechanisms and various sizes of abrasive suspended in liquid carrier or paste. Lapping processes are called three-body abrasive mechanisms; on the other hand, polishing procedure involves two-body abrasive mechanisms. Lapping has higher material removal to obtain flatter surfaces while reducing surface roughness; although, polishing is a surface smoothing process that provide a reflective surface with lower material removal rate.

Abrasive choice is crucial for crystal machining. Abrasive grains must be harder than workpiece in lapping and polishing procedures. Since CdZnTe crystals are soft-brittle materials with around 1 GPa hardness, abrasive size and type is very important to restrain the abrasive wear suffering [56]. It is given that hardness values of abrasive grains in **Table 2.4**.

Table 2.4 Hardness of abrasive materials at room temperatures

Abrasive Type	Hardness of abrasive (GPa)
Diamond	56-102
Cubic boron nitride (CBN)	42-46
Silicon carbide	~24
Silica	24
Alumina oxide	~21

2.3.1 Theory of Lapping

Lapping process can be identified as the material removal processes by the results of the frictional interaction of workpiece with plate and abrasive slurry. This process is influenced by abrasives (size, type, shape, and concentration), process parameters (velocity of plate, applied load, and lapping time), and materials (machined materials and lapping plate). In the lapping process, important properties are material removal rate, surface roughness, surface flatness, surface and subsurface damage, and residual stress.

A lapping system consists of lapping plate, slurry carrier and a holder for machined crystal. Crystals are mounted on the jig and then constant load is applied on the jig to remove the material (**Figure 2.13**). The abrasive slurry is prepared in a cylinder container to feed the lapping plate. An automatic slurry controller adjusts for constant flow rate of abrasive slurry. Low velocity is given to lapping plate to machine. Lapping processes are low-speed processes due to mechanism of abrasion and this process known as three-body abrasion.

During lapping, material removal can occur by lapping abrasives distributed in a liquid (i.e. water). The properties of lapping abrasive play an important role on mechanisms of material removal and the parameters of the process. The abrasive can be characterized by abrasive type, abrasive shape, abrasive size distribution, and mixing ratio of abrasive and liquid that are also connected to each other.

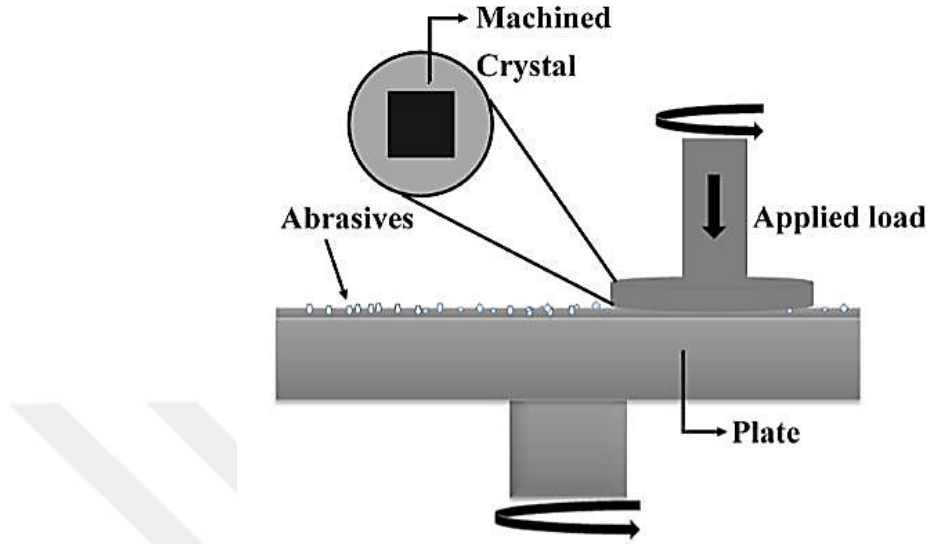


Figure 2.13 Schematic view of lapping system

The material removal is realized by the abrasives, it has to be harder than the machined crystal. Deep scratches are created with much harder and sharper abrasives than workpiece as hard abrasives can be embedded in softer materials easily. Thus, softer the machined crystal, the softer the abrasive. Since CdZnTe crystals have soft-brittle nature, lower hardness abrasives must be preferred (**Table 2.4**). Silicon carbide, most common abrasive, can be used for hard and soft materials. Aluminum oxide is preferred for machining of softer materials. Boron carbide is harder than silicon carbide and aluminum oxide, then it is used for harder materials. Diamond is much harder and sharper than others. Hence, aluminum oxide powders are more suitable than others for machining of CdZnTe crystals.

Material removal rate and surface roughness are directly related to size of abrasive. Bigger size abrasives are prone to higher MRR and higher surface roughness than smaller size abrasives. To complete high surface quality, many work cycles with smaller-sized abrasives and reduced material removal rate must be needed. It is suggested that different size of abrasives should not be used at the same time. Moreover, different lapping plates should be used for rough and fine lapping process or lapping plate should be cleaned after each size abrasives.

Number of active abrasives are determined by the mass or volume ratio of abrasives and the liquid. Mixing of lapping abrasive and lapping fluid (medium or paste) is called as lapping slurry. Abrasive concentration is volumetric mixing of abrasive and liquid generally with the ratio of 1:2 to 1:6. Abrasives are fall apart in the fluid. The optimum volumetric ratio depends on abrasive size and machined material that is only determined experimentally. Thus, all abrasive based properties strongly influence the material removal mechanisms that are related to achievable surface roughness and material removal rate.

The characteristics of lapping plate have great importance for quality lapping processes. Lapping plate made by too hard material can deeply scratch the machined crystal. Harder plates do not allow to embed abrasives on them. Therefore, abrasives roll between plate and workpiece. This may cause micro-fracture on the surface of the machined crystal due to stress. Abrasives can be embedded into the softer lapping plates. Consequently, abrasives slide rather than roll during lapping and removal mechanism is plowing. Finer surface finishing but less planarity are common results for softer lapping plates. Many types of lapping plates are available for various applications. Glass lapping plates are used for softer materials (i.e. opto-electronic materials).

During lapping processes, deformation, separation and friction processes combine to remove materials. Wear mechanism is happened while material gradual material removal from crystal by contact and relative motion of abrasive and lapping plate. There are many types of wear such as adhesion, erosion and abrasion wear. Abrasion (abrasive) wear mechanism is mostly seen for one side lapping processes that create grooves and scratches by sliding movement. Detachment of material from crystal in relative motion that caused by abrasive particles between lapping plate and workpiece or fixed in lapping plate.

2.3.2 Theory of Polishing

Polishing processes can be defined as obtaining smooth and shiny surfaces by rubbing crystals on polishing cloth or using chemical action. Polishing is crucial process for

semiconductor technology with the increasing demands for functional enhancement, since surface quality of crystals directly influence the performance of the device. Polishing technology promises completely atomically smooth mirror-like, and damage-free surfaces that are basic requirements for the high quality surfaces. Nanometer order of geometrically dimensional shapes are produced with ultra-precision polishing processes.

Abrasive based slurry is dripped on the polishing cloth and abrasives are retained on the cloth surface resiliently and elastically for mechanical and chemo-mechanical polishing processes. Higher plate velocity is applied to remove material by scratching. Mechanical and frictional actions of abrasive and polishing plate can produce shallow scratches due to micro-cutting. Material removal rate of polishing process is much smaller than the lapping process.

Polishing processes are influenced by slurry (properties of abrasive and liquids), polishing cloth, and process parameters (velocity of plate, applied load, and polishing time). Requirements of finish samples and their influencing factors depend on the parameters given above (**Figure 2.14**). Important parameters for high quality wafers are:

- Flatness or total thickness variation (TTV)
- Surface roughness
- Mechanical damages of surface and subsurface
- Crystal defects

Abrasive choosing is one of the most important parameter for polishing processes like lapping. Abrasive type, shape, size, and mixing ratio determine the process quality. Type and shape of abrasive are chosen according to the hardness of abrasive and machined crystal. Fine abrasives of below 1 μm are preferred to obtain smooth and mirror-like surfaces with the effect of polishing cloth. Fine and ultra-fine abrasives generate brittle fractures on the machined surface by removing materials in terms of plastic deformation to produce nano-scale surface roughness.

Geometric accuracy and quality of machined surfaces are necessary factors after polishing. In polishing, machined surface and polishing cloth are rubbed under constant pressure. Chip formations are produced by abrasive particles that are dripped and

embedded on the polishing cloth. Shape accuracy of plate (polishing plate or lapping plate) are transferred to crystal's surface with pressure and smooth surfaces are generated. For that reason, condition of polishing cloth (topography of cloth) should be done carefully and smooth polishing cloths with minimum elastic deformations should be used during polishing.

Material removal depends on relative velocity between the crystal and plate, applied load on jig, and time of the process. These parameters can be optimized by experimental trials since crystals has different properties and optimized parameters.

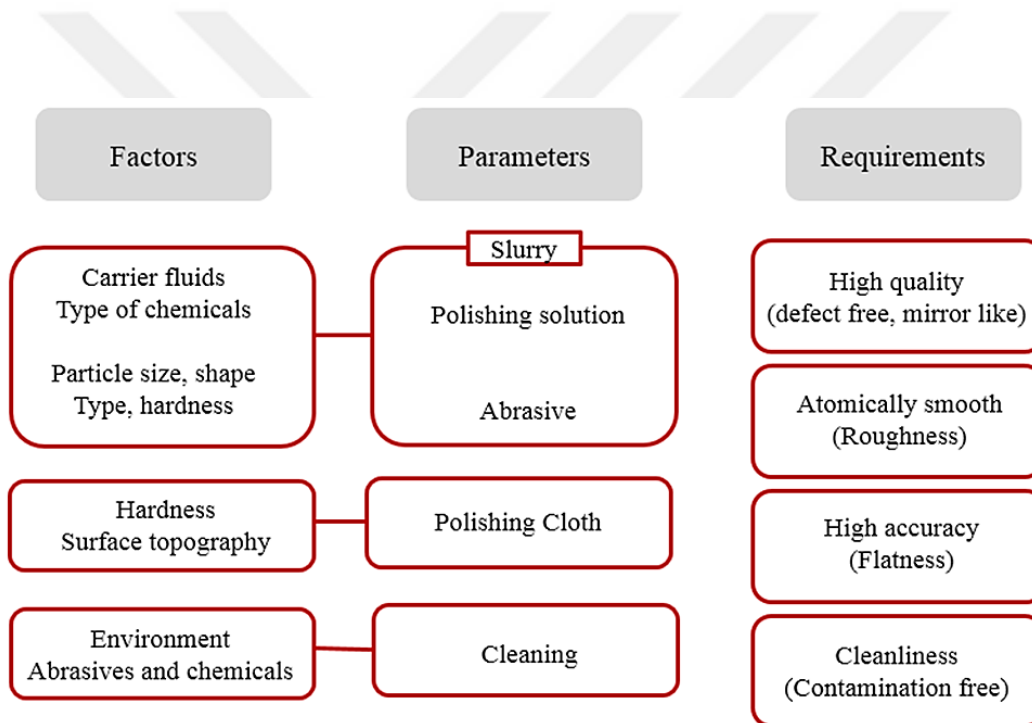


Figure 2.14 Parameters and requirements of polishing

Chip formations during polishing are important in order to obtain high quality mirror-like surfaces. Chip generations determine the surface roughness. Abrasive slurry, polishing cloth and cleaning affect the quality. Abrasives in the slurry are the main parameters for formation of chipping from the surface. Different polishing plates (cloths) should be used for different size (or type) of abrasives. If bigger or harder slurry has been used previously, polishing plate becomes contaminated and dirty with that particles which can cause higher surface roughness than expected with deep scratches. Moreover, unwanted dust particles

in the slurry can produce deep cracks on the surface. Removing large particles and dusts in the slurry, washing polishing cloth and crystal, and cleaning of environment of the polishing system enhance the quality of surfaces.

Mechanical and chemical actions influence the removal mechanisms. Mechanical actions include removal and frictional actions; on the other hand, chemical actions include oxidation and dissolving of reaction. Chemo-mechanical polishing method can be defined as the combination of these two actions. In order to improve the accuracy and efficiency, proper chemicals for oxidizing and dissolving materials can be added to slurry. Chemo-mechanical processes are mechanical and chemical processes that mechanical actions applied to the surface when chemical reactions activate on the material. In this process, both friction induced by mechanical work and chemical work involve abrasion are responsible for material removal. Chemical interaction on the surface is a more significant factor than mechanical action. Material removal rates increase and deep scratches are removed due to combination of abrasives and chemicals. Thus, chemo-mechanical polishing produce high quality surfaces without formation of damaged layer.

2.3.3 Material Removal Mechanisms

Abrasive wear can be classified in two categories as two-body and three-body abrasive wear (**Figure 2.15**). If the abrasives are bound or attached to a second body (lapping plate), it is called two-body abrasive wear. If the abrasive particles are free to roll and slide between workpiece and the second body, it is called as three-body abrasive wear. Lapping is three-body abrasive wear since abrasives can roll and slide freely. However, sometimes abrasives may embed into the plate or the machined crystal in sliding mode for a Abrasive wear can be classified in two categories as two-body and three-body abrasive wear short time referred to two-body abrasive wear. On the other hand, material removal process involve ploughing damage and grooves on the surface in rolling mode. Particle shape change the mode of abrasive wear. Round and uniform size abrasives increase the

possibility of rolling mode while rectangular and non-uniform size (larger width than thickness) abrasives are increased the possibility of sliding mode.

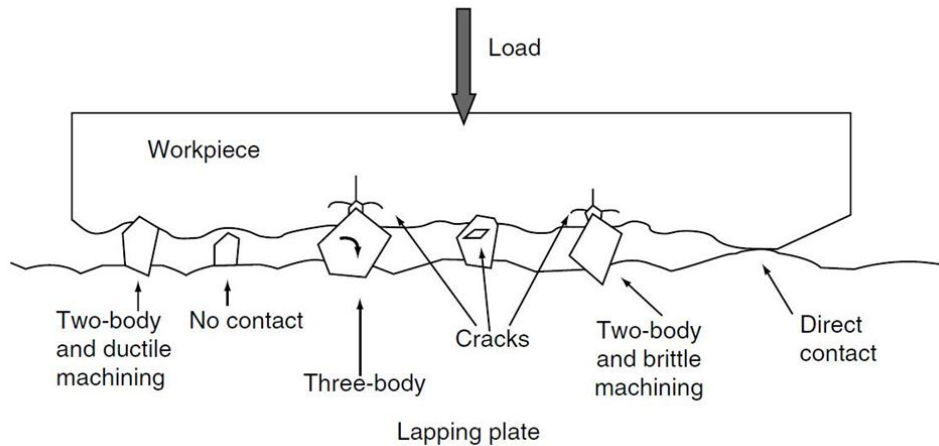


Figure 2.15 Schematic view of two-body and three-body abrasive wear

There are two main forces on the crystal during lapping processes that are pressure of the applied load and relative velocity of lapping plate and machined crystal. Increasing applied load on the jig causes deeper embedding and scratching formations on the surface. The material removal mechanisms of brittle materials is based on generation, networking and propagation of microcracks that grown the effect of stress field. Effect of abrasive wear is very important for removal mechanisms. Embedded abrasive wear and small abrasive wear removal mechanisms are also identified for soft-brittle materials during lapping.

CHAPTER 3

EXPERIMENTAL PROCEDURE

In this chapter, process flow from ingot to wafer and characterization studies of surfaces are described. Process steps that have been carried out for surface machining processes of CdZnTe crystals are as follows: slicing, lapping/grinding, mechanical polishing, and chemo-mechanical/chemical polishing. Details on surface preparation methods and material removal rate (MRR) studies are given in **Section 3.1**. Characterization studies are presented in **Section 3.2**.

Throughout this thesis, METU grown ingots have been used. Grown CdZnTe crystals are named starting with prefix MT, which stands for METU, followed by numerical order of crystal growth. For example, MT12 corresponds to 12th growth at METU-CGL

CdZnTe crystals having various sizes, crystallographic orientations, and Zn concentrations have been processed by following different surface treatments.

3.1 Surface Preparation Processes

Surface preparation processes are highly critical for detector technology. Surface and subsurface damages play an important role on detectors performance. Damages on the machined surface like inclusions, scratches, cracks, and imbedding abrasive powders bring about high leakage current strongly influencing the resolution of x-ray/gamma-ray detector. Because of soft-brittle nature of CdZnTe, crystal treatment is much more difficult than that of traditional hard-brittle or soft-plastic materials such as Si, GaAs. Ultra

precision machining is needed for CdZnTe materials. CdZnTe surface processing is highly sensitive and needs to be optimized with respect to material removal rate, surface roughness, and stoichiometry of surface.

Although the steps mentioned below in **Figure 1.1** below are the main processes of crystal machining, grain revealing and polarity determination etchants must be applied as intermediate steps. In **Figure 3.1**, general wafer processing flow diagram for CdZnTe crystals is given.

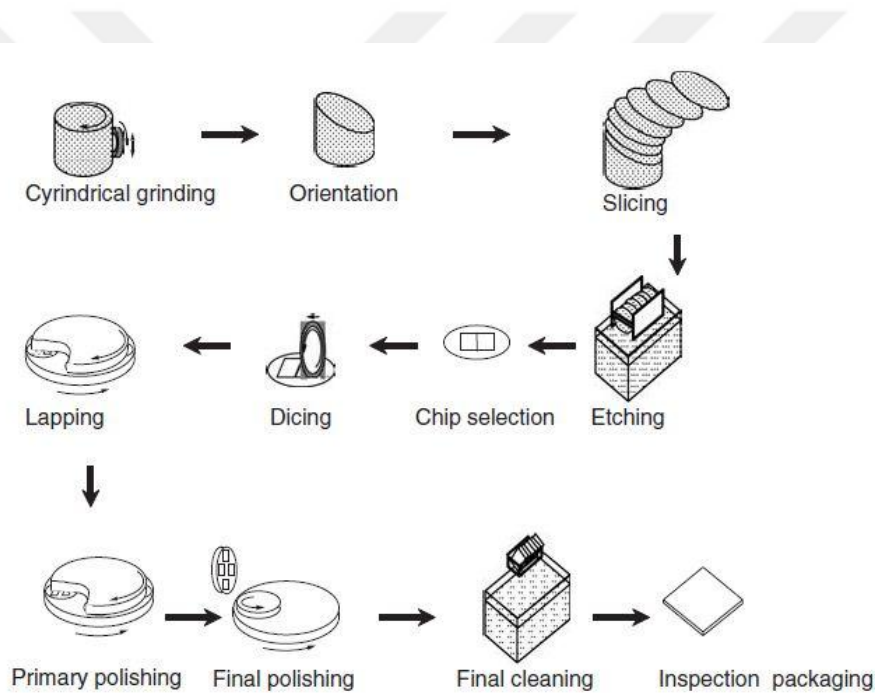


Figure 3.1 Schematic flow of CdZnTe wafer processing [2]

3.1.1 Grain Revealing Etching

Abrasive wire saw machine equipped with goniometer and 300 μm diameter diamond wire have been employed for slicing of CdZnTe crystals. Water-based cutting liquid was used as buffer between the wire and the sample in order to avoid cracks and damage. It

also provided less kerf loss. Cutting feed and wire speed parameters were optimized to avoid deflection of wire (i.e. prevention of wire breakage).

After retrieval of grown ingot from the ampoule, the conical tip and the heel parts were cut off as standard steps as shown in **Figure 3.2**. Generally it was difficult to observe grain formations on as grown or sliced ingots. To investigate grain formations, the ingot was first grinded with sandpaper and then chemically etched with grain revealing etching. Etching enabled us to see grain boundaries and also twin formations as shown in **Figure 3.3**.

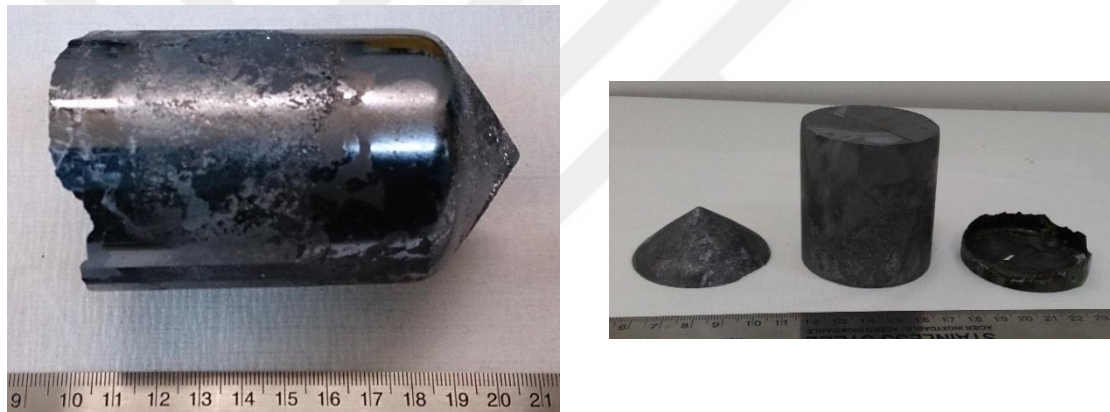


Figure 3.2 MT4 ingot before and after grain reveal etching



Figure 3.3 MT7 ingot before and after grain revealing etching

3.1.2 Orientation Dependent Slicing

In the growth of CdZnTe, grain growth take place randomly. Twins are commonly observed on CdZnTe crystals with special orientation. Twins can be called as grains which always grown on $\{111\}$ faces and grown along $[112]$ directions. From crystallographic knowledge, it was realized that $[111]$, $[110]$ and $[112]$ directions were orthogonal to each other (**Figure 3.4**). To obtain $\{111\}$ - and $\{211\}$ - oriented single crystals twining method has been developed and used during this study. With this method, selected grains were cut parallel to twin planes, if any, to obtain $\{111\}$ planes.

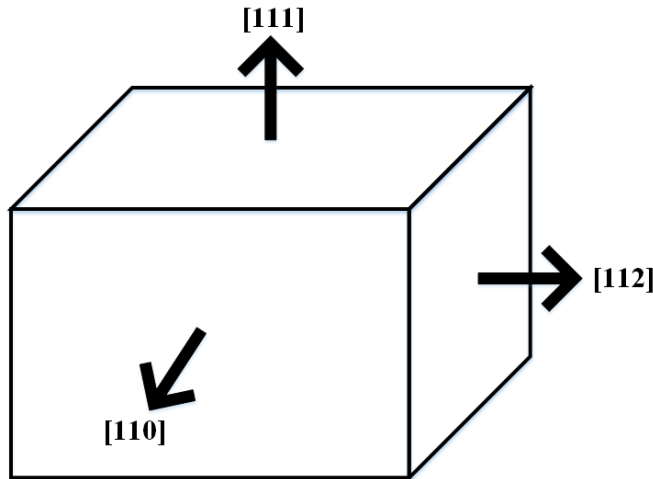


Figure 3.4 Orthogonal crystal orientations for fcc

Selected grain containing twin formations was separated from other grains to prevent from cutting of others during slicing trials (**Figure 3.5**). First twin formations were marked and then top of the marked face was arranged parallel to wire saw by goniometer. It was aimed that slicing of large thickness of $\{111\}$ -oriented pieces since edges of the sliced crystal was referred to $\{211\}$ - and $\{110\}$ -plane orientations (**Figure 3.5d**). The larger thickness $\{111\}$ orientation, the larger surface area for $\{211\}$ and $\{110\}$. Slicing experiments with twining method for MT2-grown and MT5-grown ingots have been discussed in this thesis.

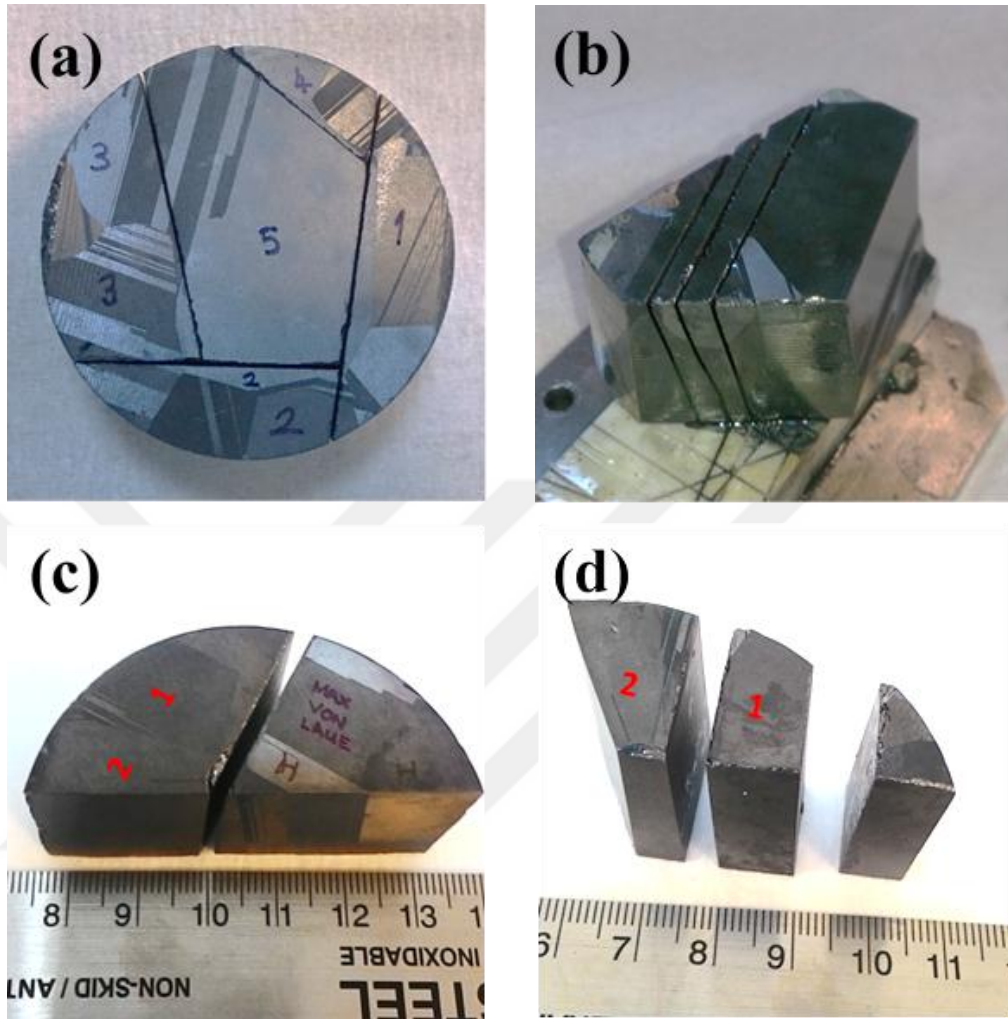


Figure 3.5 Slicing trials with twinning method (a),(b) MT2-grown ingot and (c),(d) MT5-grown ingot

MT2 ingot was sliced 5 pieces to obtain larger grain from the center. Twin formations was used to arrange goniometer and sliced on them (**Figure 3.5b**). Larger than $10 \times 10 \text{ mm}^2$ surface area $\{111\}$ -oriented wafers were sliced from MT2-grown ingot. MT5-grown ingot was also sliced to separate grains as with twin formation and non-twin formation parts. $\{111\}$ -oriented crystal with large thickness ($\sim 10 \text{ mm}$) was sliced. The edge of $\{111\}$ -oriented sliced was cut perpendicular $[111]$ direction. Therefore, $\{211\}$ - and $\{110\}$ -oriented wafers with larger than $10 \times 10 \text{ mm}^2$ surface area were obtained. XRD measurements gave the information about orientation of the crystals (**Figure 3.6**)

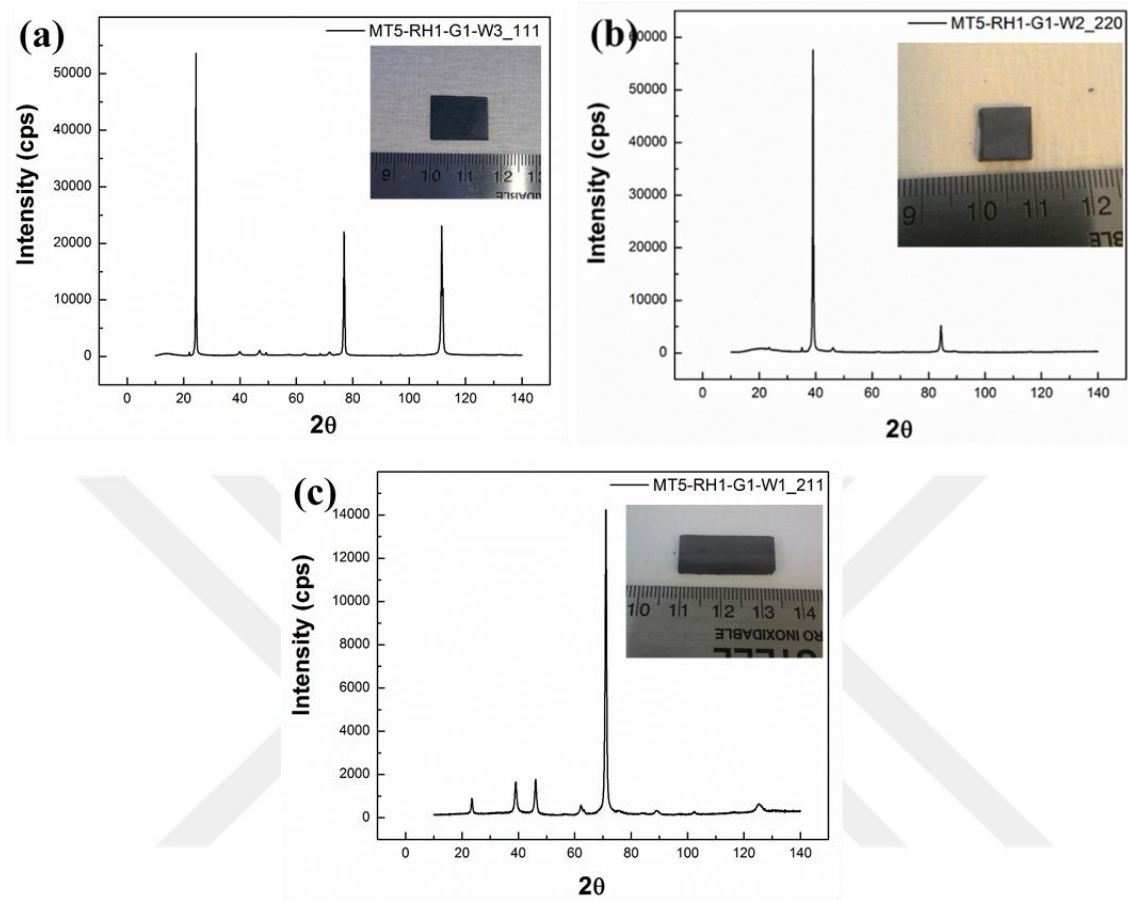


Figure 3.6 XRD measurement of (a) {111}-oriented (b) {110}-oriented (c) {211}-oriented crystals

Positions of desired orientation planes were found also by X-ray back reflection method. This method gives us information about grain orientation and angle between desired orientation and orientation of host grain. The angle was arranged with goniometer and wire cutter was employed for slicing. Slicing trials with X-ray back reflection method for MT8-grown ingot has been discussed in this thesis (**Figure 3.7**)

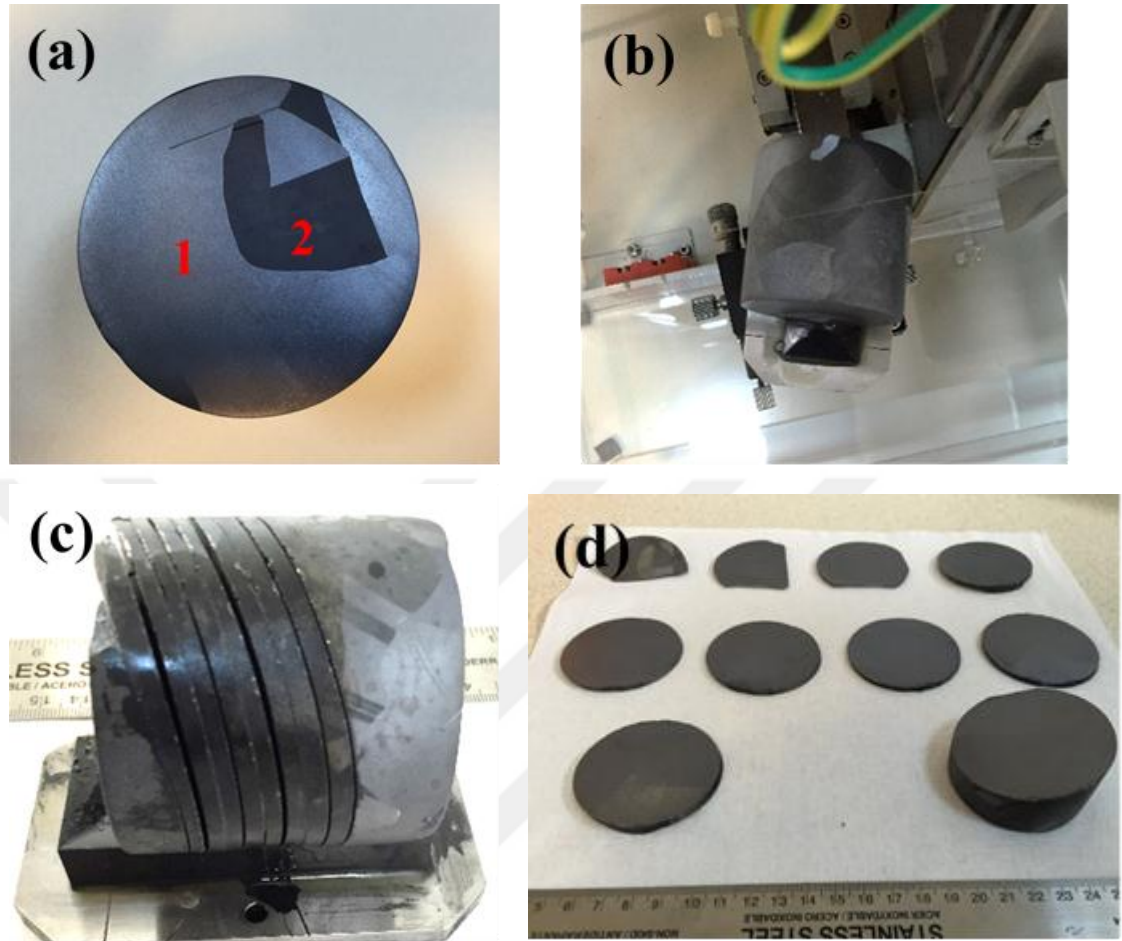


Figure 3.7 Slicing of MT8-grown ingot with x-ray back reflection method (a) selecting grain, (b) arranging wire, (c),(d) sliced crystals

Wafers were cut from sliced part which shown in **Figure 3.7c** and **Figure 3.7d**. It was obviously presented that crystal consumption was less than the twinning method. Wafers with large size area (i.e. $20 \times 30 \text{ mm}^2$) were cut from one sliced for MT8-grown ingot which had high yield.

The main advantage of this method was that any desired orientation can be sliced without twin formations. Size and number of wafers were increased with X-ray back reflection method. Moreover, total time consumed for slicing was decreased. Detailed characterizations of samples prepared with these two methods have been described in **Chapter 4**.

In general, wafers were diced from sliced part into square/rectangular shapes larger than $10 \times 10 \text{ mm}^2$. Crystals had wire damages, cracks on the surface and high subsurface damage because of brittle nature of CdZnTe after slicing. The performance of the wire saw forced us to have slices thicker than 2 mm. Thickness of wafers was changed depending on the application area such that we had thicker crystals for detector applications ($\text{Cd}_{0.90}\text{Zn}_{0.10}\text{Te}$) and thinner crystals for substrate applications ($\text{Cd}_{0.96}\text{Zn}_{0.04}\text{Te}$).

3.1.3 Polarity Determination

Between slicing and lapping procedures, surface polarity was determined by chemical etchant proposed by Brown et al. which is a mixture of HF, HNO_3 , and CH_3COOH (or $\text{C}_3\text{H}_6\text{O}_3$). (1:1:1, v/o) [24]. Crystals were dipped in this chemical solutions for 30 seconds followed by rinsing with deionized water (DIW) immediately. After etching, the matt face was identified as (111) Cd-terminated face called {111}A, and bright face was identified as Te-terminated face called {111}B by convention (**Figure 3.8**). This procedure has been same for {211}-oriented crystals.

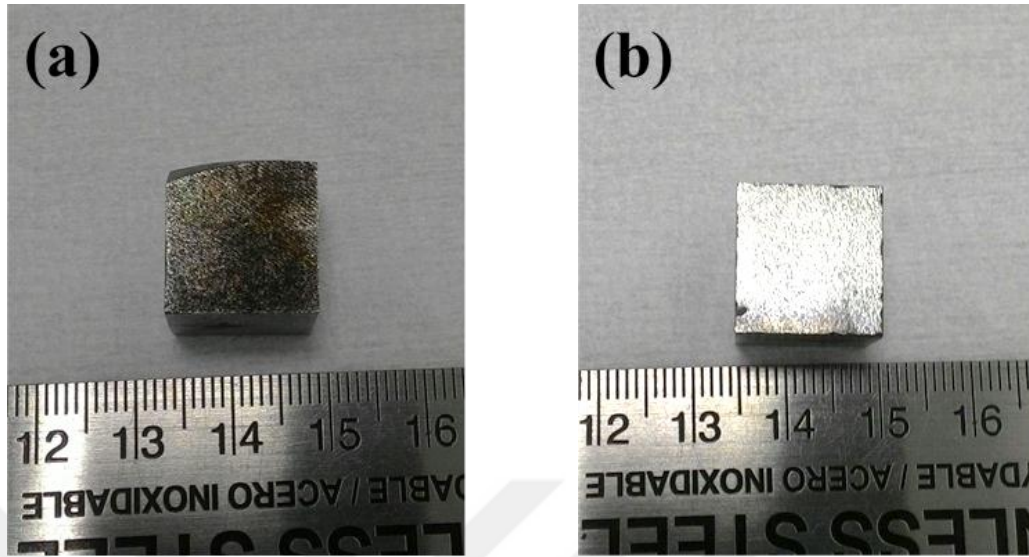


Figure 3.8 Polarity determination for $\{111\}$ -oriented crystal (a) Cd-terminated face
(b) Te-terminated face

3.1.4 Lapping Processes

During slicing and cutting procedures from ingot into single crystal wafers, surface and subsurface damages are inevitably induced. Crystals were lapped after slicing and polarity determination steps to a) remove surface and subsurface damage caused by slicing b) obtain more flat and smooth surfaces required for polishing steps and c) control the desired wafer thickness. Double-side surface preparation processes were preferred rather than single-side processes to produce ultra-flat surfaces for material characterization. Crystal thickness values were controlled thoroughly by contact thickness measurement gauge following to each surface finishing step.

Different type and size of alumina oxide (Al_2O_3) abrasive powders were used throughout this thesis study. 15 μm , 9 μm , and 3 μm sized alumina powders were mixed separately with DIW. Because of its high stock removal rate, 15 μm Al_2O_3 slurry was used if the slices were thicker. If not, lapping was started from 9 μm Al_2O_3 slurry. While the size of powders decreased, not only surface damage such as micro-cracks and cleavage but also the subsurface damage was minimized.

Various concentrations of DIW and aluminum oxide abrasives were prepared to optimize the lapping slurry. Between 10% and 15 % volume ratio was determined to be better than other concentrations. Lapping process was carried out with lapping and polishing system having an automatic abrasive slurry flow control feature which continuously feeds the plate. Specimens were bonded on a glass substrate and lapped on grooved or non-grooved glass plate depending on the dimensions of crystals. Material was removed in lapping processes by rolling or sliding abrasive particles between the surface of crystal and the glass plate which refers to three-body abrasive wear. Applied load on the jig was changed from 100g to 500g to optimize the pressure. Different plate rotation speeds were also employed to obtain material removal rate (MRR) and total thickness variation (TTV) data. TTV was calculated by measuring thickness variations from 5 different points on the crystals and taking difference of maximum and minimum value of them as shown in **Figure 3.9**. Therefore, TTV measurements gave the information about flatness of the surface, too.

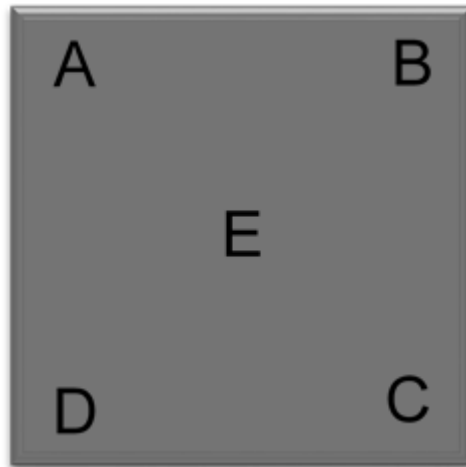


Figure 3.9 Measured points of thickness variation on CdZnTe crystals

Parameters affecting the quality of lapping process will be mentioned in material removal rate studies section.

3.1.5 Polishing Processes

After several steps of lapping procedures, a series of polishing processes was performed to improve surface quality and decrease subsurface damage layer. Mechanical polishing, chemo-mechanical polishing and chemical polishing were applied. Mirror-like surfaces were obtained for both surfaces which was necessary for characterizations.

Polyurethane polishing cloth were preferred for polishing and ultra-fine Al_2O_3 powders were mixed with DIW. Abrasives were free to roll on the glass plate in lapping process while abrasives are limited to roll on the polishing cloth in mechanical polishing process. Abrasive powders were imbedded to the polishing cloth. Another difference from lapping processes was that sub-nanometer roughness values were achieved. Successive mechanical polishing processes were completed with decreasing the particle size of powders. After 3 μm Al_2O_3 lapping procedure, crystals were polished with ultra-fine Al_2O_3 powders. Some of the crystals first polished with 1 μm Al_2O_3 powders for rough polishing to prepare samples prior to fine polishing in which 0.3 μm -sized Al_2O_3 abrasives were used for fine polishing.

Rotation velocity of plate was set to maximum rpm of the polishing system and constant abrasive flow. Different concentrations of abrasive slurry were prepared to find the most efficient one and applied load per unit area was also optimized. Total polishing time was also one of the critical parameters needed to be optimized carefully in order to eliminate subsurface damage of lapping process and keep away from over-polishing. When compared to lapping processes, surface cracks and pits were removed; however, inclusions and dislocations were appeared on the crystals surface.

After sub-nanometer rms roughness and mirror like surfaces were obtained, crystals were chemo-mechanically polished with commercial polishing fluid which include sodium hypochlorite and sub-micron size Al_2O_3 abrasives. Chemo-mechanical polishing (CMP) studies were done for time optimization. Characterization of CMP with various polishing times was completed in terms of surface morphology and topography.

A modified polishing slurry was prepared for chemo-mechanical polishing. One of the NaOCl-based commercial solution (pH around 13) that includes nano-sized silica abrasives was preferred. The polishing slurry was modified by adding strong acid into solution until pH value became around 7. Polished surfaces were analyzed in terms of surface roughness, topography and morphology. This chemical polishing slurry was called CMP1 in this study and optimized polishing parameters were used.

Based on commercial solutions, another unique solution that does not contain abrasives was developed so that the surfaces could be free of scratches. Chemicals were chosen in terms of oxidation rates and removal rates for CdZnTe. This unique solution that involve citric acid and NaOCl (pH around 7) was called CMP2 in this study.

3.1.6 Material Removal Rate (MRR) Studies

Crystal machining studies were carried out to investigate the effects of process parameters on material removal rate (MRR) in lapping and polishing. Plate rotation speed rpm, applied pressure on the samples, concentration of abrasive slurry, size of abrasives, and slurry flow rate were main parameters affecting MRR and so the machining quality. Slurry drip rate (drip/minute) has been almost the same for each lapping processes whose drip rate is lower than polishing processes. MRR was measured according to **Equation 3.1**. Thicknesses of the crystals were measured from different points before and after each steps as shown in **Figure 3.9**. Average thickness from the measurement were calculated as final thickness with contact thickness measurement gauge.

Equation 3.1
$$MRR = \frac{d_1 - d_2}{t}$$

Here, d_1 : initial thickness of crystal

d_2 : final thickness of crystal at some time of t

t: machining time

From CMP studies of crystals MRR have been equal to Preston's equation which is given in **Equation 3.2**.

Equation 3.2
$$MRR = \frac{\Delta d}{\Delta t} = C_p \cdot P \cdot V$$

In this thesis, MRR has been extensively studied to optimize lapping and polishing processes for desired thickness and to understand the quality of the surface under different conditions. According to Preston's Equation (**Equation 3.2**), MRR is directly affected by the applied pressure and plate rotation. Different slurry concentrations were prepared to obtain a relation between removal rate and the surface quality in terms of roughness.

Material removal rates were measured by changing the applied pressure where the other parameters were constant. Next, velocity of plate rotation was changed from 20 rpm to 30 rpm and MRR was calculated accordingly as other parameters were kept constant. Crystals were lapped with different size and type of abrasive particles under the same conditions and their MRR was determined. In addition to these studies, different concentrations of Al₂O₃ polishing slurry were used to compare removal rates since the abrasive particles are responsible for material removal due to rolling, sliding and embedding mechanism.

Material removal studies were conducted with (211)- and (111)- crystallographic oriented Cd_{0.96}Zn_{0.04}Te crystals. Optimized parameters were identified in terms of surface morphology, surface topography, and material removal rate. Higher plate speeds caused scratches on the surface due to micron-sized abrasives and caused non-uniform thickness during lapping. Additionally, while higher pressures cracked the edges of the crystals, lower pressures led to polishing times longer than expected. Maximum plate rotation of 70 rpm was applied during polishing processes..

Li Yan et al. mentioned that MRR and surface quality depends on crystal orientations which have different nanoscale mechanical properties. Li Yan et al. also claimed in their another work that MRR on (111)-oriented plane is smaller than (110)-oriented plane under same machining parameters because of anisotropic structure of CdZnTe crystals [28,29]. It was realized that there has not been a detailed experimental study on literature about nanomechanical behavior and MRR on different crystallographic planes of CdZnTe

crystals. Thus, optimized parameters were applied during lapping and mechanical polishing to (100)-, (110)-, (111)- and (211)-oriented $\text{Cd}_{0.96}\text{Zn}_{0.04}\text{Te}$ wafers. Furthermore, (211)-oriented $\text{Cd}_{0.90}\text{Zn}_{0.10}\text{Te}$ wafers were lapped and polished to investigate the effect of Zn mole fraction of CdZnTe ($\text{Cd}_{0.96}\text{Zn}_{0.04}\text{Te}$ and $\text{Cd}_{0.90}\text{Zn}_{0.10}\text{Te}$). Moreover, same crystals were investigated under nanoindentation tests.

3.2 Crystal Characterizations

All detector applications need high-quality substrates since the surface processes strongly influence the detectors performance. High-quality substrates require nano-scale surface roughness, high orientation accuracy, and stoichiometric crystals with low defect density.

Different techniques have been employed to characterize the quality of surface processes and crystals as well. These techniques can be classified into two groups as surface characterizations and structural characterizations.

3.2.1 Surface Characterizations

Surface characterizations are crucially important to understand and improve the quality of the surface. Surface quality is usually expressed in terms of surface roughness and surface morphology are the main analyses of the each process.

3.2.1.1 Surface Roughness Measurements

Surface roughness analyses of various processes were performed with surface profilometer Veeco dektak, atomic force microscopy (AFM), and white light interferometer.

Roughness values of as-cut sliced crystals and various abrasive-sized lapped crystals were measured with surface profilometer and AFM. Surface profilometer was scanned 3 mm line and speed of scan was 0.5 mm/sec. AFM scans on the surface were performed over $20 \times 20 \mu\text{m}^2$ and $10 \times 10 \mu\text{m}^2$ scanning areas with high resolution pixel (512 x 512). Before the measurements, parameters such as scanning speed and frequency were optimized to avoid damage on the processed surface. It was decided that tapping-mode with 4 $\mu\text{m}/\text{min}$ scan speed is suitable for soft-brittle CdZnTe single crystals.

Polished surfaces roughness was measured with white-light interferometer in addition to the AFM technique. Measurable surface area of AFM was much smaller than light interferometer measurements. Light interferometer was preferred due to larger area measurement availability ($0.35 \times 0.47 \text{ mm}^2$ or $0.35 \times 0.26 \text{ mm}^2$ depending on objectives)

3.2.1.2 Surface Morphology Measurements

Surface morphologies of differently treated crystals were observed with Optical Microscope (OP) and Scanning Electron Microscopy (SEM). Lapped and polished crystals were used to observe the effect of removal mechanisms of various-sized abrasives. Surface defects appeared on finished surface and mechanical damage were examined. While chips, scratches, and cleavages due to removal mechanisms of soft materials were analyzed for lapped specimens; polishing lines, dislocations, and inclusions were investigated for polished specimens.

3.2.2 Structural Characterizations

After slicing wafers, surface morphology have not been enabled to examine structural characterizations. With surface treatments, structural analyses have been made possible to analyze the quality of crystals and success of processes. X-ray Diffraction (XRD) method, Energy Dispersive X-ray Spectroscopy (EDX), Fourier Transform Infrared Spectroscopy

(FTIR) analyses were performed and chemical etching studies for Etch Pit Density (EPD) analyses have been carried out at METU. Except for chemical etching which was applied only after polishing procedures, other characterization techniques were applied for each surface treatment processes.

3.2.2.1 Crystal Orientation of CdZnTe Crystals

After different surface treatments, XRD measurements were repeated. Sliced, lapped and polished surfaces of same crystals were used and measurement results were recorded for each. Shifting of peak position and intensity were discussed. Besides, full-width half-maximum (FWHM) of X-ray rocking curve measurements were carried out.

3.2.2.2 Surface Composition of CdZnTe Crystals

The surface compositions of lapped and polished crystals were analyzed with EDX method. The stoichiometry of the surface after each surface treatment was measured. $\text{Cd}_{0.90}\text{Zn}_{0.10}\text{Te}$ and $\text{Cd}_{0.96}\text{Zn}_{0.04}\text{Te}$ crystals were used. Atomic concentrations of elements on processed CdZnTe surfaces were obtained and Te overall ratio to Cd+Zn was measured. Additionally, this method was used to investigate surface contamination after treatments. Since samples were exposed to air, surface was covered with Carbon (C) and Oxygen (O) easily. Except for Cd, Zn, Te, C and O elements, Aluminum (Al) was also found at compositional analyses due to abrasive based slurry.

3.2.2.3 IR-Transmittance of CdZnTe Crystals

A Fourier Transform Infrared Spectroscopy (FTIR) analysis was used to understand not only the IR transmission of crystals but also the defect structure inside the crystals. In the

wavelength interval 2-20 μm , nearly 60% IR transmission is expected. IR transmittance (%) was measured with Bruker Equinox 55 FTIR Spectroscopy for different treatments. Single side polished and double side polished wafers were prepared from the same ingots to investigate the difference. Chemical polishing solution, Inoue's E-solution, was applied to single-side polished crystals to analyze the effect of chemical polishing. HNO_3 (10 mL) + H_2O (10 mL) + $\text{K}_2\text{Cr}_2\text{O}_7$ (4 g) were the chemicals of E-solution [44]. Crystals were dipped various times (40 s, 60 s, and 120 s) to understand chemical polishing effect on IR-transmission.

3.2.2.4 Defect Revealing Etching for CdZnTe Crystals

Chemical etching experiments were applied to reveal defects in the crystals. Etching processes are known as destructive analyses. Everson, Nakagawa and Inoue etching were used to reveal dislocations lines, inclusions, and etch pits (**Table 3.1**). Different chemical etchants utilize the analysis of crystals and surface quality. Crystals were dipped to chemical solutions and after that crystals were rinsed with DIW. Crystals were dried with air immediately. Etched surfaces were examined with OP and SEM imaging techniques. Etch pit formations are observed based on Thomson tetrahedron, shape of pits varied depending on crystallographic orientation. Various oriented crystals that are {111}, {211}, {100}, and {110} oriented $\text{Cd}_{0.96}\text{Zn}_{0.04}\text{Te}$ crystals were etched with Inoue's solution capable of revealing defects for all orientations. Finished surfaces was chemically etched to investigate Te-inclusions. EPD was used to compare IR-transmittance in the range of 14-20 μm wavelengths to decide crystal quality of selected ingots.

Table 3.1 List of dislocation revealing etching

Etchant	Chemicals	Time
Everson [46]	HF:HNO ₃ :Lactic acid (1:4:25,v/o)	5 minutes
Nakagawa [45]	HF:H ₂ O ₂ :H ₂ O (3:2:2,v/o)	2 minutes
Inoue [44] (EAg1,EAg2)	10 mL E-solution+ 0.5 g AgNO ₃	2 minutes
	10 mL E-solution+10 g AgNO ₃	

3.3 Nano-mechanical Characterization of Crystals

Nano-indentation tests were performed for different orientations and different Zn-concentration. For this specific study, {111}-, {100}-, {110}- and {211}- oriented slices from Cd_{0.96}Zn_{0.04}Te and {211}-oriented Cd_{0.9}Zn_{0.1}Te crystals were cut. Crystals were lapped and polished under same conditions. A Berkovich diamond indenter was used with 100 nm tip radius. Hardness and elastic modulus of various crystals were measured as a function of applied load. Different loads varied from 1 mN to 9 mN were applied. Loading and unloading times were 10 s and a 10 s awaiting period between loading and unloading was selected. Because of anisotropy of CdZnTe crystal, hardness values vary for different crystallographic orientations and additional Zn in the CdTe structure also influences the harness and elastic modulus. Micro-mechanical behaviors were influenced nano-mechanical behaviors so material removal rates of different orientations are not the same as nano-mechanical properties.

3.4 Subsurface Damage Experiments

Subsurface damages inside the crystals degrade the quality of detectors in terms of mechanical, optical, and electrical properties. Field emission scanning electron microscopy was employed to investigate subsurface damages. Two polished surfaces were

bounded on the top of the polished faces by bonding wax as shown in Error! Reference ource not found.. Cross-section crystal machining was applied to the surface. Surface treatments listed below were applied:

- 9 um lapping
- 3 um lapping
- 1 um rough polishing
- Ultra-fine polishing

Samples were etched with 5 ml HNO_3 + 10 ml H_2O + 2 g $\text{K}_2\text{Cr}_2\text{O}_7$ + 0.25 g after treatment proposed by Li Yan's group [28]. This etching solution which is modified from Inoue etching solution was used to reveal damages. The etching time was 30 seconds. Micro scale damages were investigated by SEM.

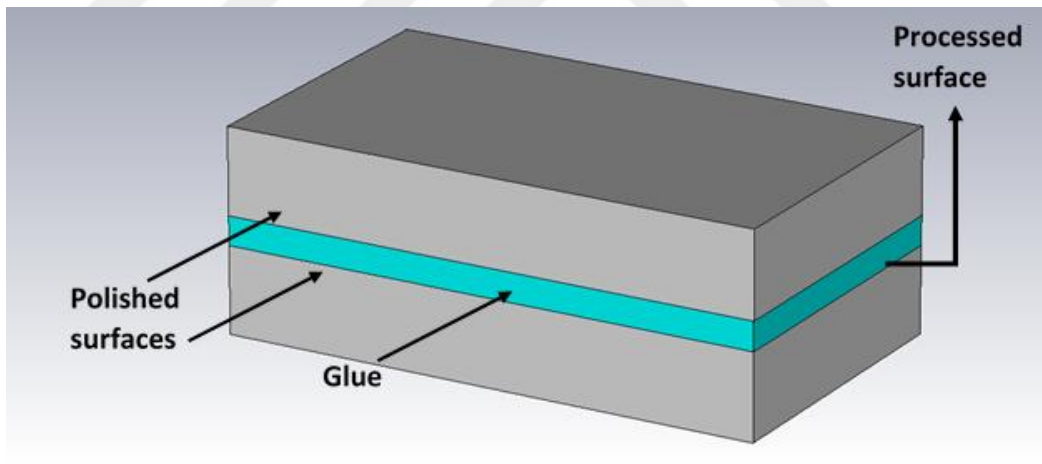


Figure 3.10 Schematic view of bonded-interface method



CHAPTER 4

RESULTS & DISCUSSION

In this chapter, results of surface preparation studies are given. Material removal studies with changing of load and plate speed for various size of Al_2O_3 abrasives are shown. Optimization studies for different orientations are discussed in **Section 4.1**. Surface characterizations of MT-grown crystals after lapping and polishing steps are discussed in **Section 4.2** and finally structural characterizations are evaluated in **Section 4.3**. CdZnTe bulk-growth, surface treatment studies and characterizations of prepared surfaces were conducted at METU-CGL

4.1 Material Removal Rate Studies

Surface quality of CdZnTe is highly critical for both infrared and x-ray, gamma ray applications. Due to its soft and brittle nature, the surface of CdZnTe is highly prone to be scratched and can be damaged easily. Thereby it is necessary to pay special attention during mechanical and chemical processes. After slicing by a wire saw or dicer, several lapping processes are applied. Primary purpose of lapping is to remove the surface and subsurface damage formed after the cutting process and reduce to wafer thickness to the desired value. Later, mechanical and chemical polishing is applied to obtain atomically smooth and defect-free surfaces. Mechanical steps with Al_2O_3 abrasive based solutions must be optimized to obtain high quality surfaces in terms of surface roughness and flatness

In this section, the results of material removal rate studies are presented. Optimization studies were carried out for (211)- oriented $\text{Cd}_{0.96}\text{Zn}_{0.04}\text{Te}$ wafers. An identical study was conducted for (111)- (100)- and (110)- oriented $\text{Cd}_{0.96}\text{Zn}_{0.04}\text{Te}$ wafers to compare material removal rates of different crystallographically oriented crystals. Moreover, (211)-oriented $\text{Cd}_{0.90}\text{Zn}_{0.10}\text{Te}$ crystals were also lapped and mechanically polished with optimized parameters to understand the effect of Zn concentration.

Optimization of material removal includes adjustment of equipment parameters such as applied pressure, plate speed etc. Applied pressure on the jig was chosen in such a way that the material removal can be done in a well-controlled and uniform way. In general, lower plate speeds were applied for lapping studies due to micron-sized Al_2O_3 abrasives (i.e. high removal rate) while higher plate speed was used for polishing studies due to ultra-fine Al_2O_3 polishing abrasives (i.e. low removal rate and uniformity). Slurry concentration was 15% volume ratio for the lapping procedure. For polishing, abrasive based slurry concentration varied from 5% to 20% volume ratio to obtain better surface quality in terms of roughness.

4.1.1 Material Removal Rate Studies for Lapping Procedure

During lapping studies, material removal rate ($\mu\text{m}/\text{min}$) was determined by measuring thickness variation per minute. A contact mode thickness measurement gauge was employed for thickness measurements from five selected points on the crystals.

{211}-oriented $\text{Cd}_{0.96}\text{Zn}_{0.04}\text{Te}$ crystals were used for material removal rate (MRR) optimization studies. According to Preston Equation, MRR mainly depends on applied pressure and velocity of platen. Other factors affecting MRR, crystal structure (orientation and Zinc concentration), and slurry properties (size, type, concentration, and drip rate of abrasive) are accounted for in the Preston constant (C_p).

MRR of lapping processes were conducted under various applied loads on the jig for 20 rpm and 30 rpm platen velocity (**Figure 4.1**). 15% volume ratio of Al_2O_3 abrasive and DIW mixture were used for all lapping processes. MRR increased almost linearly as the applied load and platen velocity were increased.

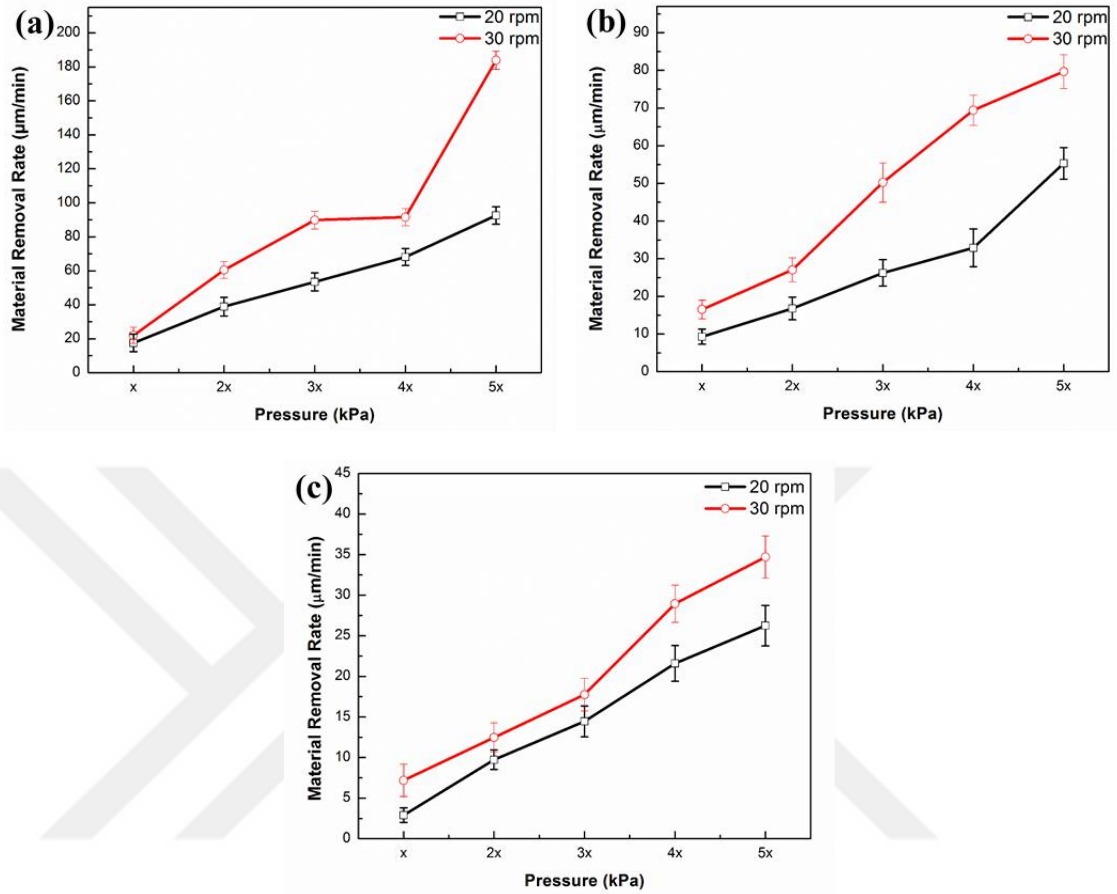


Figure 4.1 Material Removal Rate Studies with 20 rpm and 30 rpm plate speed (a) 15 μm Al_2O_3 (b) 9 μm Al_2O_3 and (c) 3 μm Al_2O_3

Large diameter abrasives removed much more material from the crystals in a minute. For 15 μm Al_2O_3 abrasives and 20 rpm rotation, removal rates varied between 17.5 and 92.5 $\mu\text{m}/\text{min}$ as the applied pressure was changed. Similarly, for 30 rpm rotation, MRR increased from 22 to 123 $\mu\text{m}/\text{min}$ when the jig load increased linearly. 15 μm Al_2O_3 abrasive slurry was used only for thicker samples due to high material removal rate.

9 μm Al_2O_3 abrasive has MRR between 9 and 55 $\mu\text{m}/\text{min}$ for various applied loads, in the meantime, plate rotation was 20 rpm. Based on Preston equation, MRR was expected to change by 1.5 times when the rotation was set to 30 rpm. Removed material per minute was higher than expected due to experimental variables that strongly affect the Preston constant.

Material removal rate was smaller for 3 μm -sized Al_2O_3 abrasives as expected. MRR changed from 2.9 to 26.4 $\mu\text{m}/\text{min}$ by applying load between 100 g to 500 g for 20 rpm plate rotation. MRR rose around 1.5 times for 30 rpm.

In general, plate velocity rpm, applied force on the wafer, size of abrasive, concentration of abrasive, and slurry drip rate have great influence on the MRR and therefore on lapping processes [57]. Influence of variables on MRR was analyzed. Theoretically, if variables are constant during lapping, MRR must be constant. Experimental results show that, MRR show tiny changes even if the parameters are kept constant. Changing zinc concentration in the crystals due to zinc segregation along the ingot, inaccuracy in preparation of abrasive concentration, jig rotation and jig position during lapping, and reconditioning of the lapping plate may have influence on the MRR. Even though such factors are present, reproducible results were achieved for all lapping processes.

It is obtained that higher removal rates with increasing applied load as expected since there exists a linear relation between MRR and pressure (Preston Equation). Due to uncontrolled thickness value under higher pressures and difficulties of adjusting lower pressures on small size wafers (i.e. $1 \times 1 \text{ cm}^2$), 300 g ($\sim 30 \text{ kPa}$) has been determined as the most suitable value for all lapping processes.

According to Preston equation, MRR is proportional to the platen velocity. 20 rpm was decided as optimized parameter since 20 rpm has lower stock removal than 30 rpm.

Preston constant, C_p , includes the abrasive type, size, and concentration of slurry. Calcined alumina was used with 15% (v/o) concentration for all lapping processes. Decreasing of abrasive size resulted in lower material removal.

Table 4.1 Material Removal Rate of different crystallographic orientations with various size of Al₂O₃ abrasives

Al ₂ O ₃ abrasive size	MRR of Different Crystallographic Orientations			
	{111}	{100}	{211}	{110}
15 μm	38.58	47.55	49.70	66.18
9 μm	20.66	24.74	25.98	32.00
3 μm	12.38	13.29	15.22	16.61

Different crystallographic orientations were sliced from Cd_{0.96}Zn_{0.04}Te ingots to understand their effect on MRR. The atomic density of different crystallographic orientations are not the same and therefore this leads to anisotropic mechanical properties [29]. Therefore, MRR changes according to hardness of planes related to atomic density. Number of atom inside the crystals can be arranged in the following order, {111}>{100}>{110} according to Miller indices as shown in **Figure 4.2**.

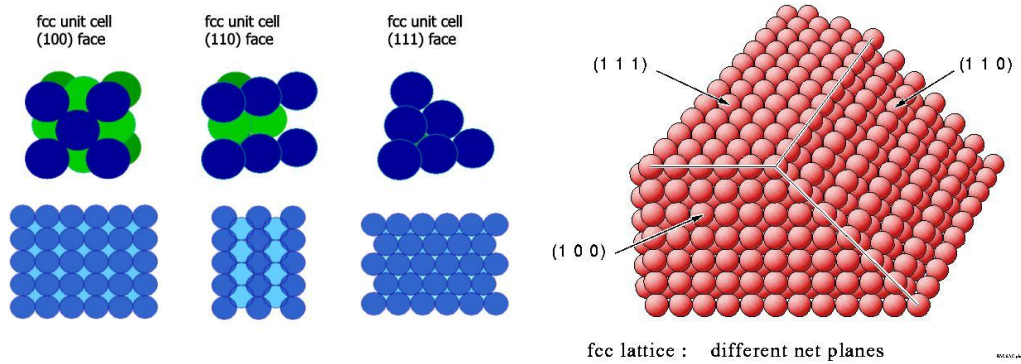


Figure 4.2 Atomic density of (100), (110), and (111) planes for fcc crystals

Optimized lapping parameters were applied to different crystallographic orientations to measure MRR and hardness of crystals (see **Section 4.4**). Applied pressure and plate rotation speed was kept constant during processes. Only the crystallographic orientation was variable that was involved in Preston constant, C_p . According to experimental results in **Table 4.1**, when atomic density increased, it was getting hard to remove material from

the surface. The increasing order of material removal rate for differently oriented crystals is $\{110\} > \{211\} > \{100\} > \{111\}$.

$\{111\}$ planes are known as closed packed planes offered minimum frictional force on the surface. $\{110\}$ plane is cleavage plane for zinc-blende structures and that leads to the easy-removal of materials because of higher fracture energy. (Fracture energies for $\{111\}$ - and $\{110\}$ -oriented crystals are $\omega_{f\{111\}} = 0.580 \text{ J/m}^2$ and $\omega_{f\{110\}} = 180 \text{ J/m}^2$ [18].)

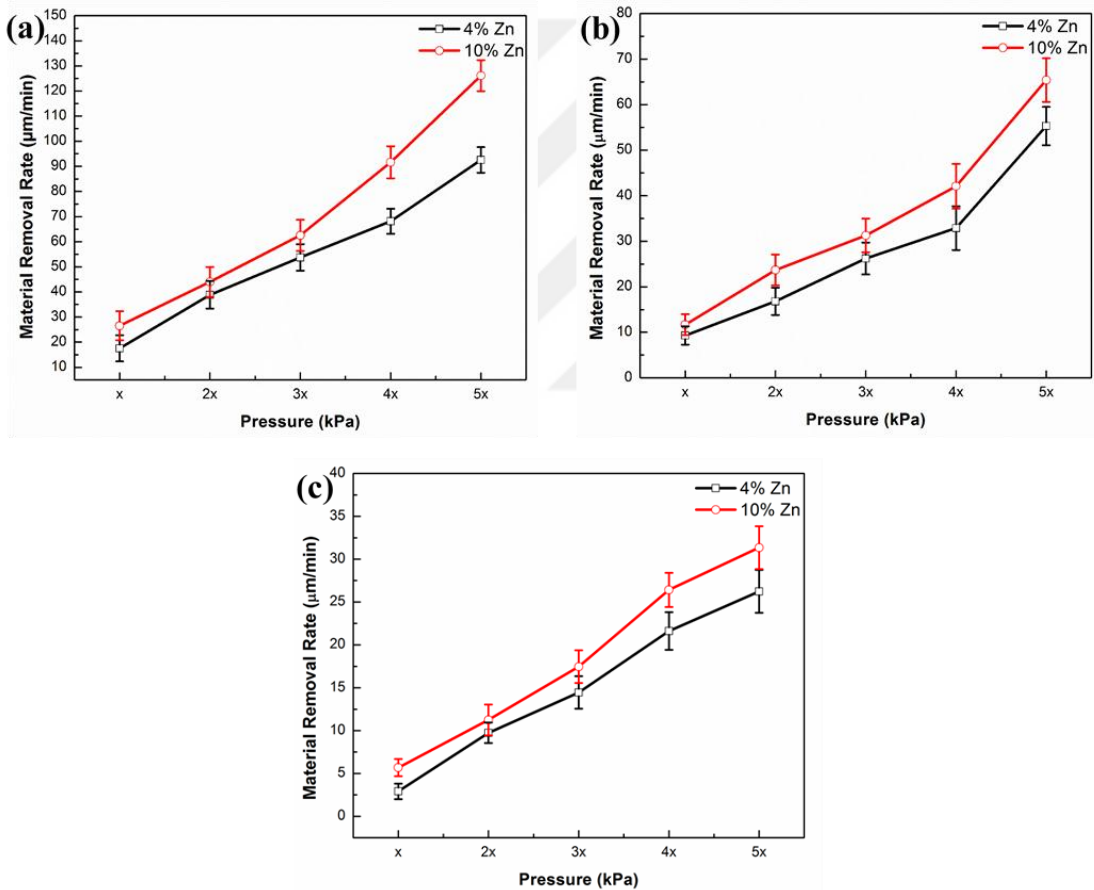


Figure 4.3 Material removal rate studies for $\text{Cd}_{0.90}\text{Zn}_{0.10}\text{Te}$ and $\text{Cd}_{0.96}\text{Zn}_{0.04}\text{Te}$ crystals with same parameters (a) $15 \mu\text{m}$, (b) $9 \mu\text{m}$, and (c) $3 \mu\text{m}$ Al_2O_3 lapping

In order to see the effect of Zn concentration, $\text{Cd}_{0.90}\text{Zn}_{0.10}\text{Te}$ crystals were analyzed in terms of MRR under the same parameters as $\text{Cd}_{0.96}\text{Zn}_{0.04}\text{Te}$ crystals. Results are shown in **Figure 4.3**. Mechanical properties of these CdZnTe crystals are known to vary with zinc

concentration. The crystals have different frictional coefficient and different hardness. These factors have influence on the MRR.

Following parameters were used during lapping processes,

- Plate speed: 20 rpm
- Abrasive concentration: 15% (v/o) Al_2O_3 inside the DIW
- Constant slurry drip rate
- Various applied load (from 100 g to 500 g)

As we see from the results displayed in **Figure 4.3**, material removal of $\text{Cd}_{0.90}\text{Zn}_{0.10}\text{Te}$ crystals were higher than $\text{Cd}_{0.96}\text{Zn}_{0.04}\text{Te}$ crystals. Cd atoms are substituted by Zn atoms in the $\text{Cd}_{1-x}\text{Zn}_x\text{Te}$ crystals. Bond energies of Cd-Te and Zn-Te are different than each other and this affects the soft nature of crystals.

4.1.2 Material Removal Rate Studies for Polishing Procedures

Several steps of polishing processes were applied to the lapped samples. During the polishing, thickness changes were measured by contact mode thickness measurement gauge. MRR and total thickness variations were measured after each process.

{211}-oriented $\text{Cd}_{0.96}\text{Zn}_{0.04}\text{Te}$ crystals were used for optimization of polishing parameters under different applied loads. Different types of slurries were prepared for mechanical polishing, chemo-mechanical polishing and chemical polishing processes. According to Preston Equation, abrasive concentration and slurry type included in Preston constant C_p influence the MRR.

0.3 μm Al_2O_3 inside DIW were prepared with different concentrations (20% (v/o) to 5% (v/o)) to measure MRR and observe the effect of abrasive removal on the crystals. To optimize applied load for polishing studies, 15% and 7.5% Al_2O_3 and DIW mixture was used (**Figure 4.4**). Since abrasives are responsible for material removal, MRR increased with higher abrasive concentration. Moreover, MRR almost linearly increased with the

changing of applied load. 300 g applied load was decided as optimized pressure parameter during polishing studies.

Different abrasive slurry concentration was prepared for MRR. Surfaces were polished under the following parameter,

- 300 g applied load
- 70 rpm platen velocity
- Stable (but higher than lapping) drip rate

Increasing of abrasive concentration led to more removal on the surface due to the abrasives. There is a logarithmic increasing of the MRR. The reason of not to be linear increasing is abrasives can be embedded into the polishing cloth and this is prone to be decreasing of MRR.

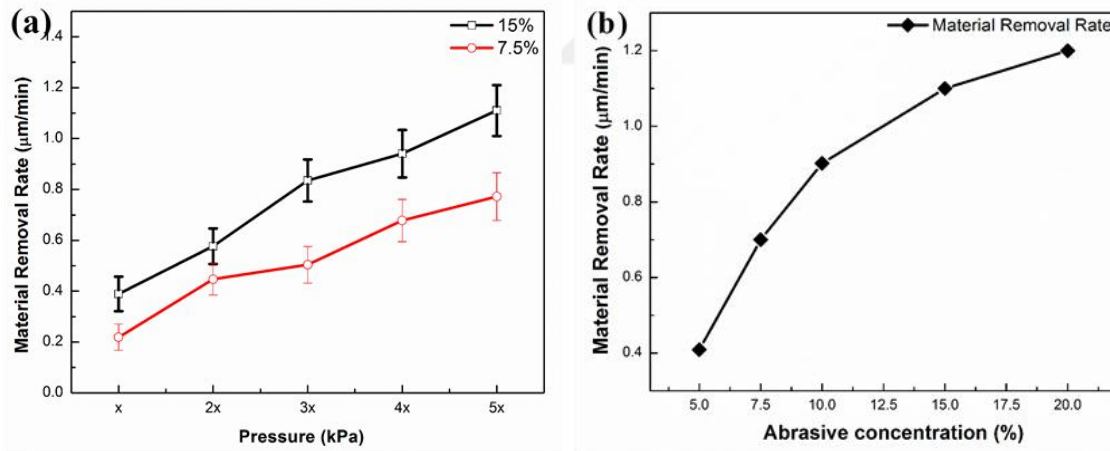


Figure 4.4 Material removal rate for mechanical polishing (a) under different applied load (b) under different slurry concentration

Optimized parameters were used for chemo-mechanical polishing and chemical polishing processes too. MRR of each process are given in the (Table 4.2). While mechanical polishing include removing and frictional processes, chemical polishing include oxidizing and dissolving. In chemo-mechanical polishing, materials are removed by the combination of abrasives and chemical reactions. For that reason, MRR was higher for

chemo-mechanical polishing processes and the lowest values of MRR belonged to chemical polishing.

Table 4.2 MRR of polishing processes

Process	Mechanical Polishing	Chemo-mechanical Polishing	Chemical Polishing
MRR	0.4-1.2 μm	7.2-5.3 μm	50-32 nm

Total thickness variation (TTV) is measured as the maximum and minimum thickness of the surface (**Table 4.3**). After each surface preparation, it is aimed to obtain flatter surfaces as abrasive size decreases. After final polishing, TTV can be as low as 1 μm . In lapping and polishing, the shape of the plate (glass plate or cost-iron plate with polishing cloth) is transferred to the machined crystals. Thus, plate condition has great influence on the flatness and changing of thickness along the crystal. Moreover, crystals were bonded to glass substrate by wax. Wax uniformity under the crystals may influence the thickness changes.

Table 4.3 TTV of surface preparation processes

Process	As-cut	Lapping	Polishing
TTV	130-68 μm	7.4-3.8 μm	2.3-1.1 μm

4.2 Surface Characterizations

Lapping, mechanical polishing, chemo-mechanical polishing, and chemical polishing were applied as sequential steps for surface preparation of crystals. After each surface treatment process, samples were characterized separately. Surface roughness measurements were carried out using AFM and surface profilometer after lapping

processes and white-light interferometer were employed after polishing processes. Morphology of surface was inspected with FE-SEM and/or optical microscope (OP) after each treatment.

4.2.1 Lapped Surface Characterization

Various sized of Al₂O₃ powders were chosen during the lapping process. Crystals were lapped with 15 μm, 9 μm, and 3 μm Al₂O₃ powders in DIW. Optimized parameters used during all lapping procedures are listed in **Table 4.4**.

Table 4.4 Optimized Lapping Parameters

Abrasive size (μm)	Load (g)	Platen speed(rpm)	Concentration of DIW and Al ₂ O ₃
15, 9, 3	300	20	10%-15% (v.)

4.2.1.1 Surface Roughness of Lapped Crystals

After each step, surface roughness were measured with AFM (area scan) and surface profilometer (line scan) methods. Surface topographies after each lapping steps were examined. The root-mean-square (rms) roughness of lapped crystals were investigated. In addition, cross-sectional lines for the peak to valley depths of surfaces were analyzed.

A typical AFM image showing the surface topography and x-y line scans from center of the measured surface after lapping procedure with 15 μm Al₂O₃ abrasives (**Figure 4.5**). Surface roughness-rms was nearly ~500 nm. Difference between maximum height and minimum valley value of the scanning area (peak to valley, PV) was about 3 μm. Large size of pits were observed on topographic image. The pits were related with material removal mechanisms of abrasive based lapping procedure. Abrasives were responsible for

removing and flattening the crystals, but at the same time abrasive particles could be imbedded into the crystals. Since samples were ultrasonically rinsed in isopropyl alcohol with high-frequency, some of embedded abrasives are removed from the surface leaving behind empty holes. The main reason of such a high roughness value was due to the depth of pits from 15 μm Al_2O_3 abrasive.

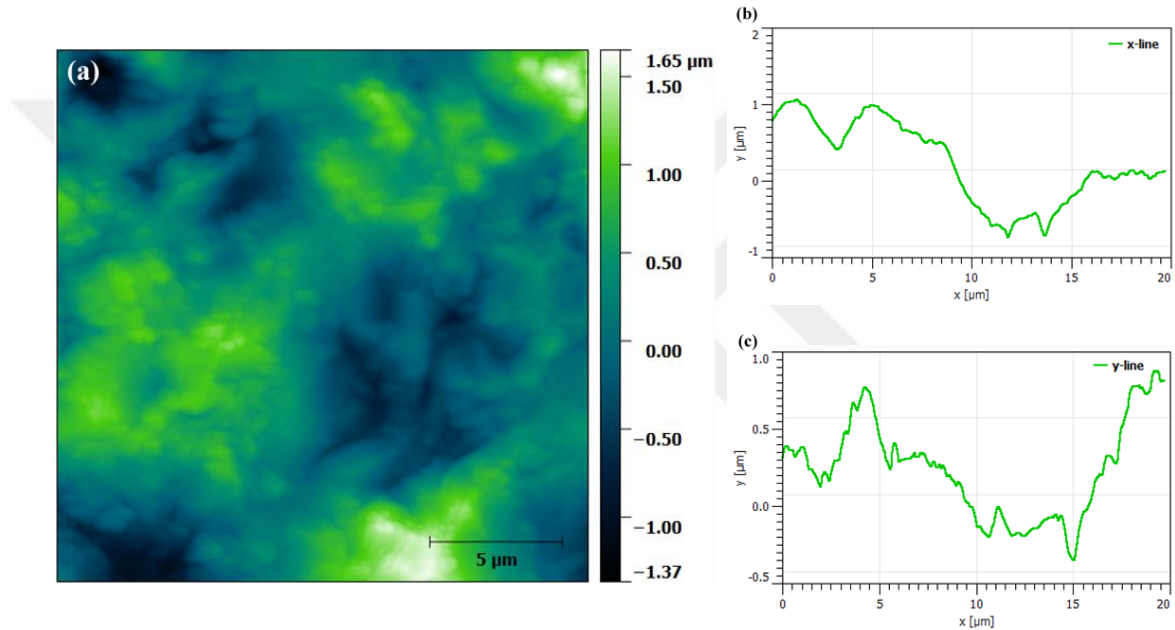


Figure 4.5 AFM measurement; (a) Surface topography, (b) x-line scan, and (c) y-line scan for 15 μm Al_2O_3 lapped crystal

After surface treatment with 9 μm Al_2O_3 abrasive, AFM measurement was repeated. Crystals were ultrasonically cleaned before the measurement to remove embedded abrasive and chipped CdZnTe particles on the surface. Surface topography and x-y line scans near the center were analyzed as shown in **Figure 4.6**. While surface roughness was nearly ~ 400 nm, peak to valley was around 2.70 μm , nearly similar to 15- μm -lapping. Density of pits were decreased due to small size of abrasive.

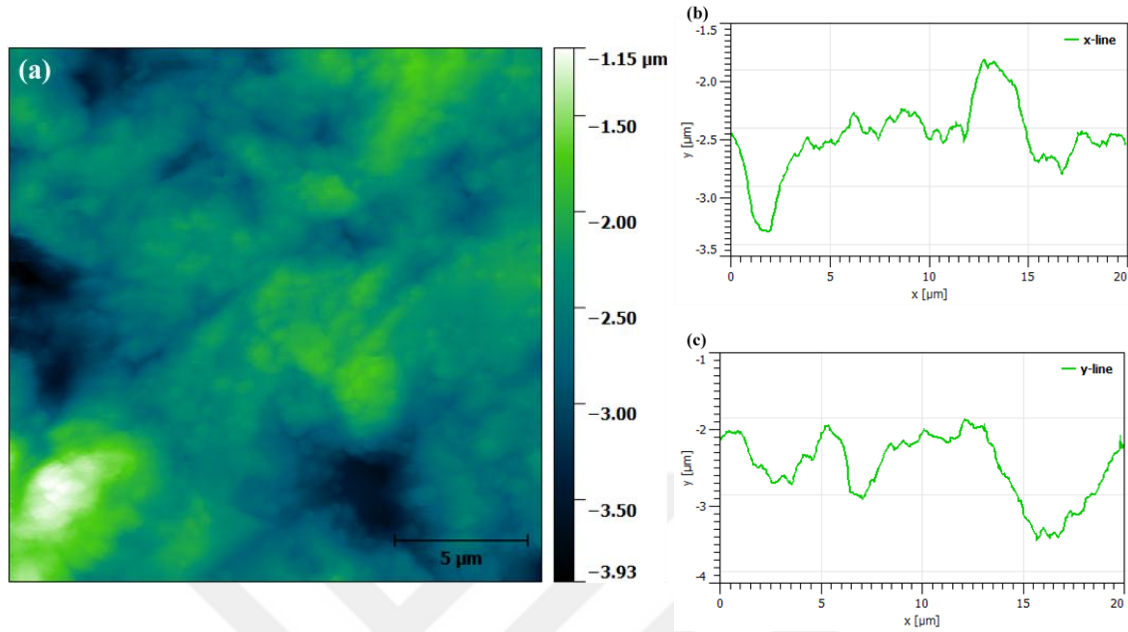


Figure 4.6 AFM measurement; (a) Surface topography, (b) x-line scan, and (c) y-line scan for 9 μm Al₂O₃ lapped crystal

It was presented that surface topography and x-y line scan from the center (**Figure 4.7**) after 3 μm Al₂O₃ abrasive. The surface roughness-rms was nearly ~250 nm and peak to valley value was around 2 μm. Small size pits as well as different size of scratches were observed on the surface. Because of the use of hard abrasive material to machine soft-brittle CdZnTe crystals, deep and shallow scratches were formed during the material removal. Density of pits were much smaller and pit sizes substantially reduced. Moreover, we obtained less variation in the line scans than bigger size abrasive processes as can be seen in **Figure 4.7b** and **Figure 4.7c**

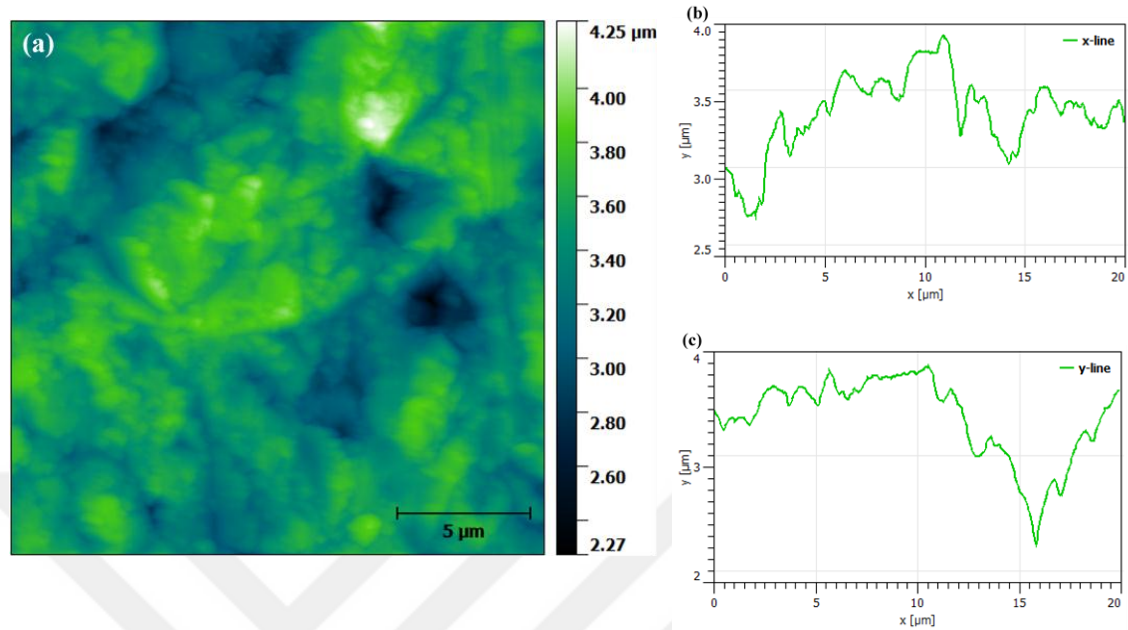


Figure 4.7 AFM measurement; **(a)** Surface topography, **(b)** x-line scan, and **(c)** y-line scan for 3 μm Al_2O_3 lapped crystal

Frictional interaction mechanism was observed between abrasive, glass plate and the crystal during lapping processes. Al_2O_3 abrasives were free to roll and slide between plate and crystal. Abrasives were the main factor scratching the surfaces and they were embedded on the surface of crystals during removal mechanisms. This removal mechanism of soft materials produced pits, cleavages, micro-cracks, micro-fatigue and chips. These were blamed for and causing the surface and subsurface damage. However, AFM technique cannot characterize cracks under the pits. Upon cleaning in an ultrasonic bath, some of embedded abrasives were removed and pits are formed on the surface. Various sizes of Al_2O_3 caused different dimensions and depth of damages (**Figure 4.8**). Combination of these damages, irregular pits and scratches, determined the surface roughness.

Pit dimension was measured to be around $\sim 10 \mu\text{m} \times 10 \mu\text{m}$ with nearly $2 \mu\text{m}$ depth after $15 \mu\text{m}$ Al_2O_3 lapping and the large pit was combination of small pits (**Figure 4.8a**). Pit area was around $\sim 5 \mu\text{m} \times 5 \mu\text{m}$ and depth of pit was nearly $1.4 \mu\text{m}$ after $9 \mu\text{m}$ Al_2O_3 lapping (**Figure 4.8b**). Pit sizes are reduced as a result of smaller abrasive size. Density

of pits also were almost half of previous process as mentioned before. When the Al_2O_3 abrasive particle size is further reduced to $3\ \mu\text{m}$, smaller pit area ($2.9\ \mu\text{m} \times 2.9\ \mu\text{m}$) as expected; however, depth of pits did not changed that was around $1.3\ \mu\text{m}$ (**Figure 4.8c**). Dimensions and depths of the pits were almost same on the analyzed surface. Furthermore, depths scratches were almost same with pits showed that abrasives scratched the surface during removal mechanism.

According to the results obtained, abrasives have not got in uniformly shaped. While mixing Al_2O_3 abrasives with DIW, particles may be bonded to each other or chipped. Small abrasives can be more easily imbedded into the surface which can have certain effect on the surface roughness and flatness.

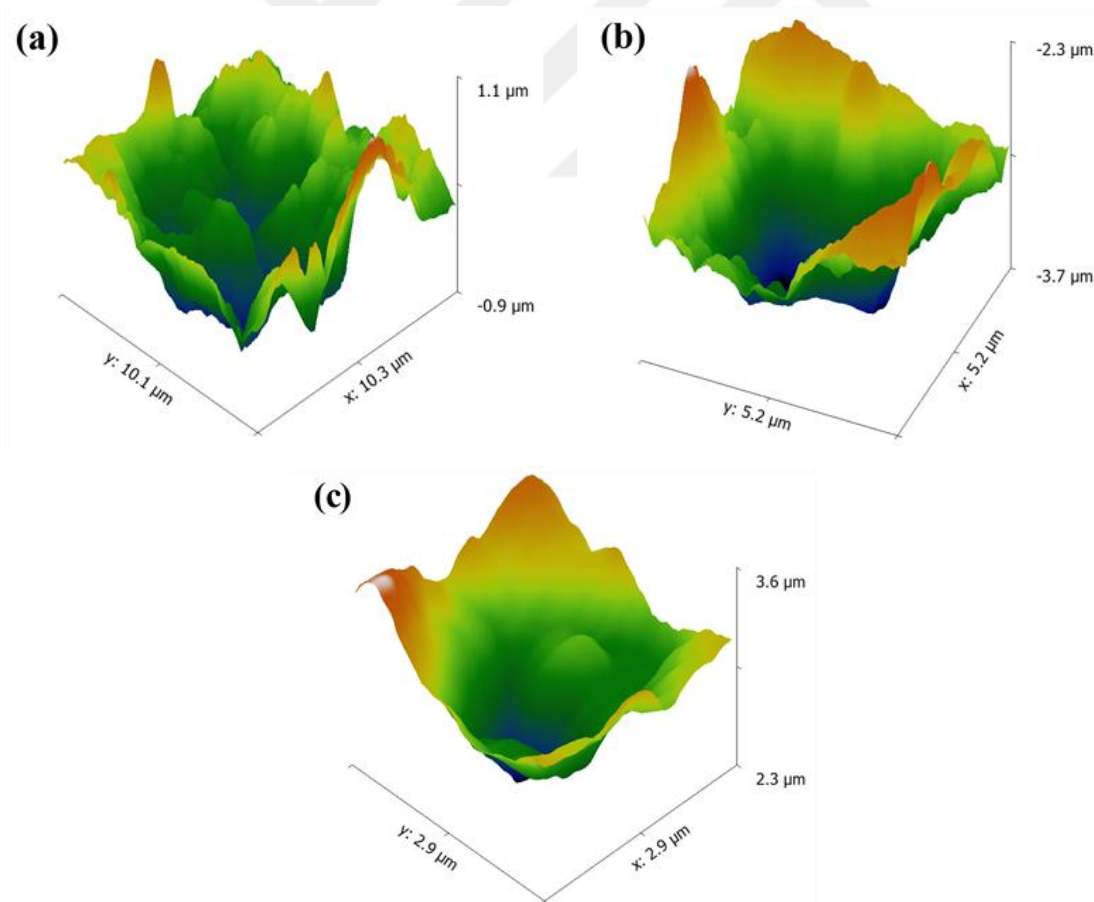


Figure 4.8 3D topographical images of pits after lapping with (a) $15\ \mu\text{m}$ Al_2O_3 , (b) $9\ \mu\text{m}$ Al_2O_3 , and (c) $3\ \mu\text{m}$ Al_2O_3

Surface profilometer was employed to measure surface roughness R_q by line scanning over 3 mm length. This profilometer was used only on lapped surfaces due to lower sensitivity. From these experiments, surface profile were observed and deviations between maximum and minimum point on scanned line were determined.

We see that surface roughness and standard deviation values were close to those obtained from the AFM measurements (**Table 4.5**). Surface roughness rms (R_q) was around 780 nm for 15 μm Al_2O_3 lapped and maximum deviation of the measured line was 3.2 μm . The main reason of roughness value difference between AFM and surface profilometer is related to the measurement method. While selected area was scanned line by line with AFM, stylus non-contact profilometer scanned only single line. Roughness of scanned line was nearly 400 nm after 9 μm Al_2O_3 lapping process and 191 nm surface roughness was measured for 3 μm Al_2O_3 lapped surface. While roughness measurements of line scan were almost similar with area scan, differences were seen on maximum and minimum values with these two methods.

Table 4.5 Surface profilometer results

Surface Treatment	Surface Roughness (R_q)	Maximum deviation (σ)
15 μm Al_2O_3 lapped	776 nm	3.2 μm
9 μm Al_2O_3 lapped	399 nm	1.4 μm
3 μm Al_2O_3 lapped	191 nm	0.9 μm

4.2.1.2 Surface Morphology Analyses of Lapped Crystals

Surface morphology of crystals after each lapping processes were analyzed with SEM. Captured SEM images after 15 μm , 9 μm , and 3 μm lapping processes are presented in **Figure 4.9**. Images were taken 800x magnification. It was clearly observed that surfaces became more featureless with the smaller powder size of Al_2O_3 abrasive particles. Surface damage was also reduced. Lapping processes created crystal machining related defects

such as micro-cracks, scratches. Moreover, embedded abrasive were mostly removed by ultrasonic cleaner and removed abrasives left micro holes on their corresponding places (**Figure 4.9**).

Many cracks and pits were observed on 15 μm lapped crystal surface (**Figure 4.9a**). Abrasive based removal mechanisms was created cracks while rolling processes on brittle materials. Pits (large and small pit around it) marked on the SEM picture with dashed circles and size of large pit was around 13 μm .

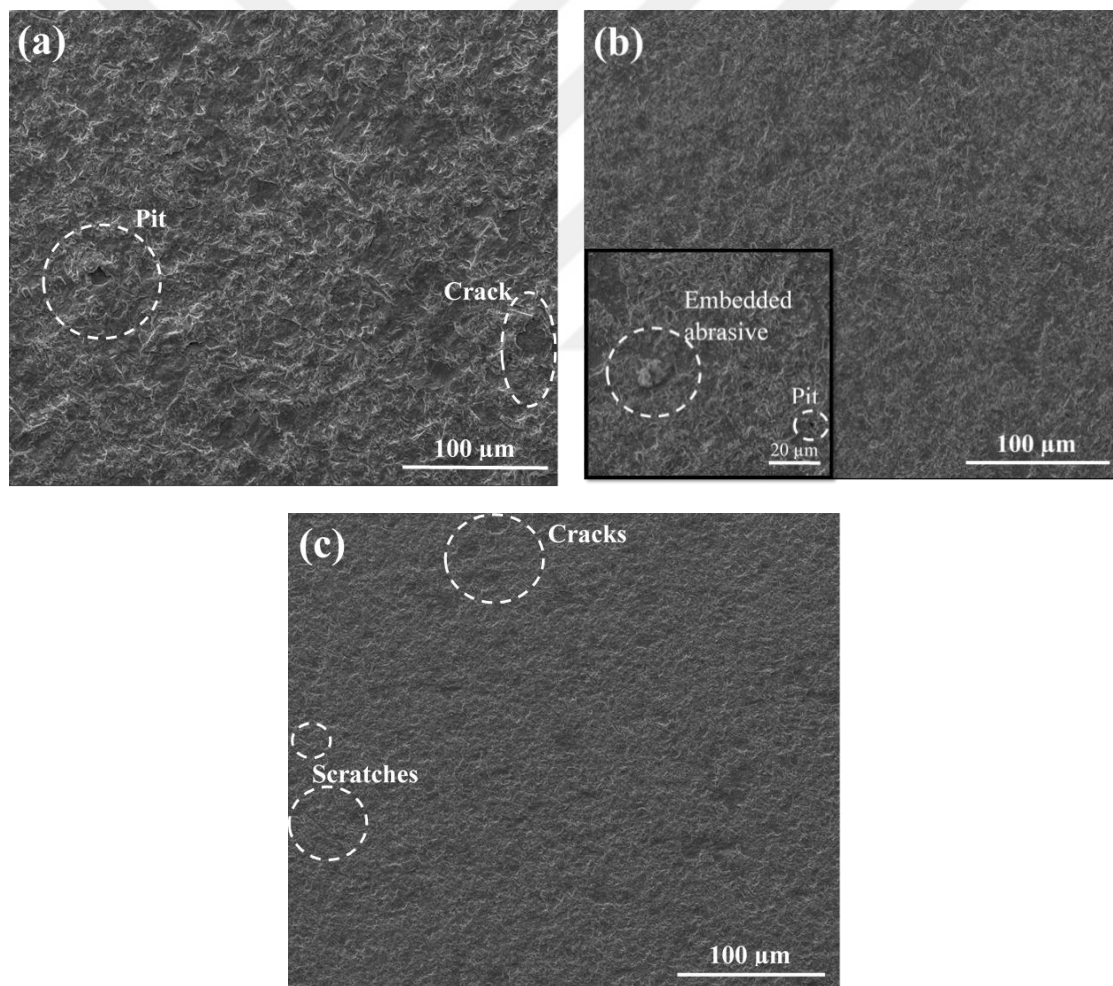


Figure 4.9 Surface morphology of CdZnTe single crystals with 800x magnification (a) 15 μm lapped, (b) 9 μm lapped and (c) 3 μm lapped

For 9 μm Al_2O_3 lapped surface mm abrasive, cracks, embedded abrasives and pits were still observable (**Figure 4.9b**); however, surface topography became more homogenous with decreasing particle size. Besides, imbedded powders into the surface could not be removed with ultrasonic cleaning due to deep embedment. The size of embedded abrasive was nearly 9 μm . Moreover, there was a pit near the surface which possibly caused by small abrasive wear mechanism.

Small scratches and cracks were observed on the 3 μm Al_2O_3 lapping processed crystal (**Figure 4.9c**). Density and size of cracks were decreased and surface became topographically smoother. However, small size of scratches were found on the surface apart from larger size abrasive stated previously. The reason of first-time-appeared scratches may be due to sliding removal mechanism by small size free abrasive lapping.

A closer examinations of various size of Al_2O_3 lapped procedures is shown in **Figure 4.10**. SEM images were captured with 12000x magnification. Cleavages are clearly seen from the pictures. Similar to pit formation mechanism, depth and size of cleavages changed with the size of abrasive. CdZnTe has zinc-blend structure which is described as a pair of interpenetrating face centered cubic (fcc) and its cleavage plane is {110} plane. CdZnTe crystals have high tendency to cleave along [110] direction due to soft nature. Lapping processes were performed on {111}-oriented crystals. Cleavage formations were pyramidal type due to the angle between cleavage plane and processed plane. Moreover, cracks, chips, and scratches as machining micro-defects were investigated.

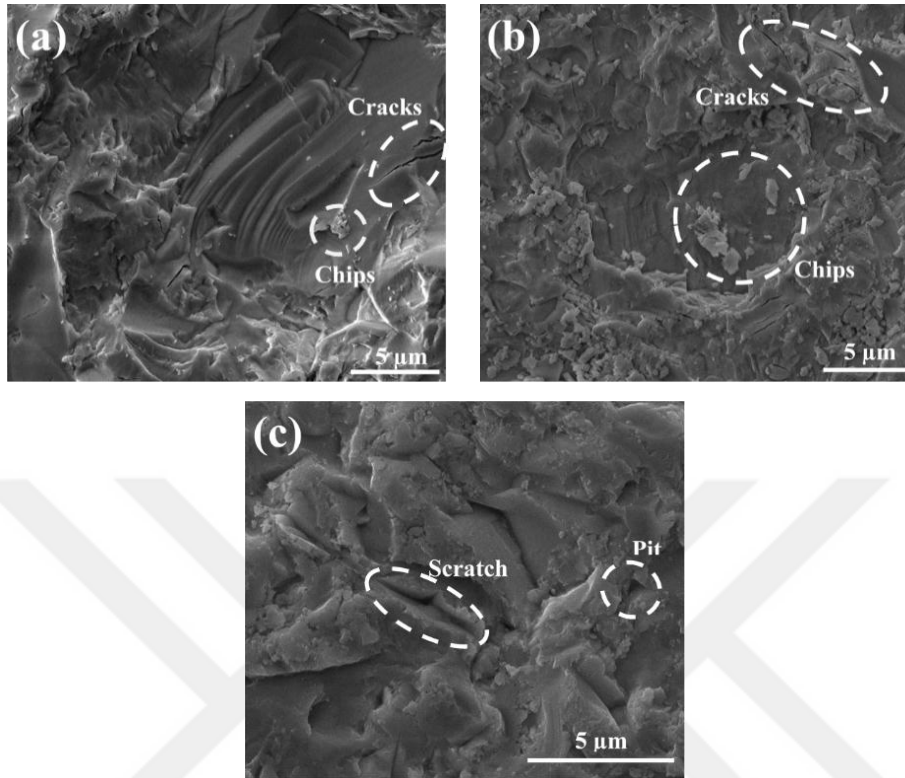


Figure 4.10 Cleavages of CdZnTe single crystals with 12000x magnification (a) 15 μm Al_2O_3 lapping, (b) 9 μm Al_2O_3 lapping, and (c) 3 μm Al_2O_3 lapping

Chips were often found inside cleavage surrounded by cracks after 15 μm lapping process (**Figure 4.10a**). Steps of cleavage plane were clearly seen. The number of chips and cracks increased after 9 μm lapping (**Figure 4.10b**). After 3 μm lapping, cleavages became smaller and chips vanished (**Figure 4.10c**). Scratches on the surface were generated due to small size of abrasive.

Abrasives were free to roll and slide between lapping plate and processed crystal refers to three-body abrasive wear. Rolling of abrasives between lapping plate and processed crystal may cause pitting and micro-cracking on the surface and chips were flaked off from CdZnTe surface during removal. Applied load on the crystals during lapping may create micro-cracks. Micro-cracking were observed after all processes but size and density decreased with finer abrasive. Chips were generally observed inside the cleavages. Sliding of abrasives can be the reason of scratches mostly observed after 3 μm Al_2O_3 lapping.

Eventually, 3 μm -lapped surface became topographically homogeneous. The size and density of cracks decreased; chips and pits vanished; however, the number of line-scratches increased.

4.2.2 Surface Characterizations after Polishing

To improve surface quality, crystals were mechanically polished with ultra-fine Al_2O_3 abrasives. Rough polish was applied to Cd terminated face (A-face) and Te terminated face (B-face) was fine polished. Chemo-mechanical polishing (CMP) was developed during this study. In-house developed CMP slurries were applied.

1 μm and 0.3 μm Al_2O_3 abrasives were mixed with DIW separately to be used as mechanical polishing solution. Selected parameters used during the polishing studies are given in **Table 4.6**.

Table 4.6 Parameters of Mechanical Polishing

Size of Al_2O_3 abrasive	Load (g)	Velocity (rpm)	Mixture of DIW and Al_2O_3
1 μm 0.3 μm	300	70	7.5%-15% (v/o)

Polyurethane polishing cloth examined with SEM to estimate removal mechanisms during polishing (**Figure 4.11a** and **Figure 4.11b**). Based on this cloth structure, abrasives are more likely embedded into the pores and two-body abrasive wear removal mechanism forms; so that abrasives are not free to roll. By limiting the movements of free abrasives, uniformly distributed wear is obtained. Polishing cloth structure seem to be destroyed due to applied force on the jig during both mechanical polishing and chemo-mechanical polishing (**Figure 4.11c** and **Figure 4.11d**). Since there was frictional interaction between polishing cloth and the crystal during removal, depth of holes decreased and width of them were enlarged. Because chemo-mechanical polishing suspensions were prepared by

mixing selected chemicals and ultra-fine abrasives, different cloths must be used for mechanical polishing and chemo-mechanical polishing processes. The cloth for CMP studies had more damage than the cloth for MP due to attacking of chemicals.

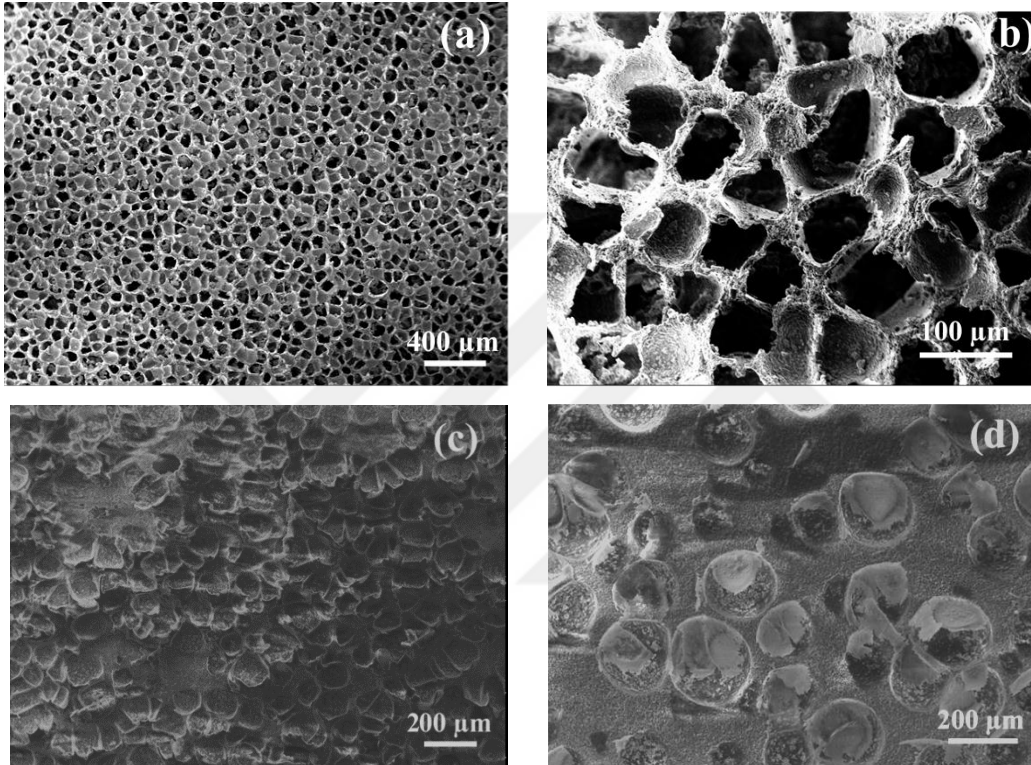


Figure 4.11 Polyurethane polishing cloth (a) 80x (b) 1500x, and used cloth during (c) mechanical polishing (d) chemo-mechanical polishing

4.2.2.1 Surface Roughness of Polished Crystals

AFM and white-light interferometer were employed to analyze the surface topography, flatness and roughness rms for mechanical polishing steps. AFM has measured the area varying between $5\ \mu\text{m} \times 5\ \mu\text{m}$ and $20\ \mu\text{m} \times 20\ \mu\text{m}$ whereas white-light interferometer were capable of measuring large area up to $0.35\ \text{mm} \times 0.47\ \text{mm}$.

After mechanical polishing with $1\ \mu\text{m}\ \text{Al}_2\text{O}_3$ and DIW slurry, surface topography and x-y line scans from the center were recorded as shown in **Figure 4.12**. Crystal was cleaned

with ultrasonic cleaner in isopropyl alcohol to avoid sticking abrasives on the surface. Surface roughness rms was found to be around 9.80 nm and difference between maximum and minimum point of measured area was nearly 105 nm. Although surface was much more flat than lapping processes, small features were detected on the surface. From line scans, peak heights were nearly 60 nm. It is claimed that CdZnTe pieces which could not be removed, formed together on the surface. Moreover, shallow scratches (i.e. polishing lines) were also observed.

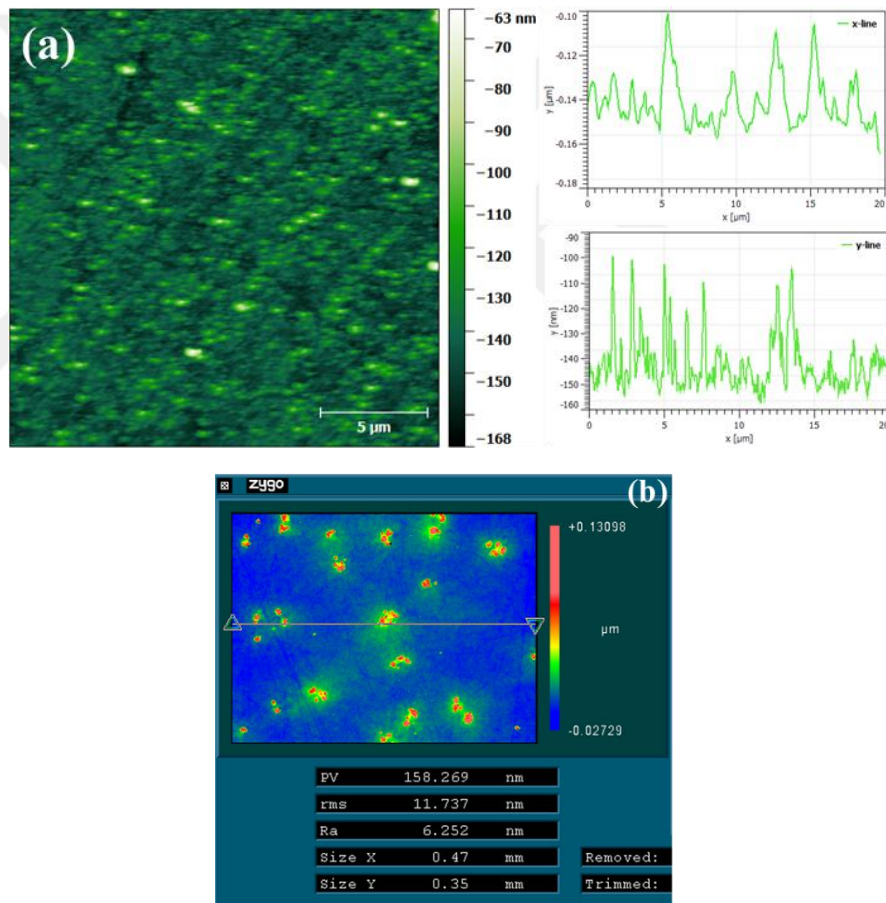


Figure 4.12 Surface roughness and topography measurements with (a) AFM method and (b) White light interferometer method for 1 μm Al₂O₃ polishing process

Surface topography was measured with white light interferometer with 0.47 mm x 0.35 mm surface area after 11 μm Al₂O₃ polishing (**Figure 4.12b**). Surface roughness rms was

around 11 nm and peak to valley difference was 158 nm. Although roughness value was close to small area measurement with AFM, PV degree was much higher. On the surface, CdZnTe particles leading to higher PV values were present. Crystals were intended to be more flat and smoother by using 1-micron-ultra-fine powder and polishing cloth. Obviously, 1 μm Al_2O_3 abrasive was not sufficient for fine polishing though.

As the last step of mechanical polishing, crystals were polished with 0.3 μm Al_2O_3 and DIW slurry. AFM was employed again to analyze surface topography for 20 μm x 20 μm and 10 μm x 10 μm surface areas (**Figure 4.13**). Even though surface was ultrasonically cleaned in isopropyl alcohol in 5 minutes, embedded abrasives were observed on the surface (20 μm x 20 μm). Surface roughness rms was 2.93 nm and difference of maximum peak and minimum valley was nearly 52 nm. Polishing lines and deep grooves were detected on the surface due to abrasive based polishing. Embedded abrasive density was higher than expected. It was observed that methanol solution cleaned the surface more effectively than isopropyl alcohol.

Surface topography of cleaned surface was measured (**Figure 4.13b**). Measured area was 10 μm x 10 μm . Surface roughness rms was 1.34 nm and the peak to valley value was around 17 nm. Surface of the crystal was quite clean and abrasive free. However, polishing lines from removal mechanisms were observed. Deep and shallow scratches partially covered the surface. Although the surface was atomically smooth, scratches should be removed to get better surface quality. Chemo-mechanical polishing study was needed to obtain more smooth and scratch free surfaces.

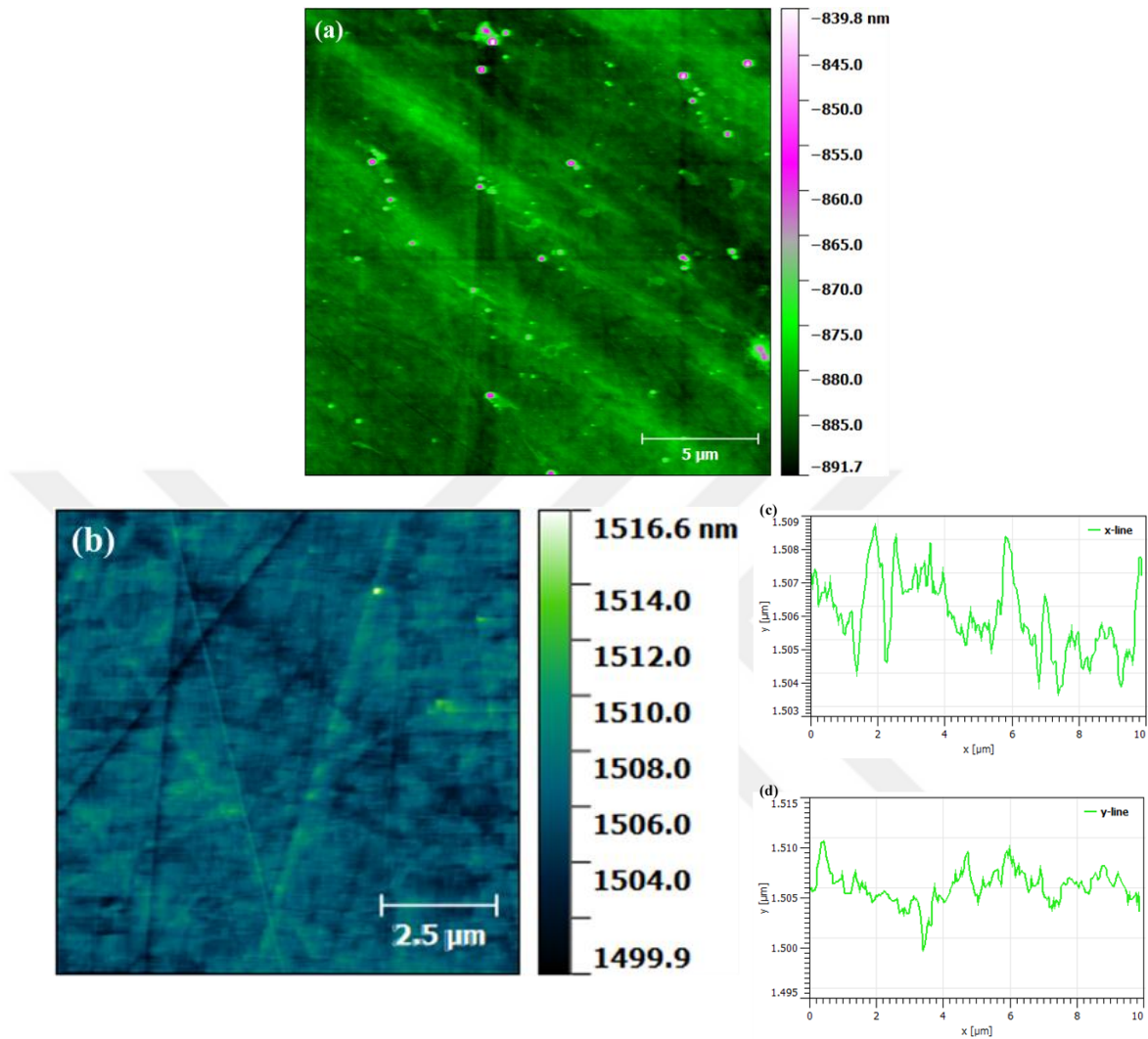


Figure 4.13 AFM measurement of 1 μm Al_2O_3 polishing process for (a) $20 \times 20 \mu\text{m}^2$ and (b) $10 \times 10 \mu\text{m}^2$ surface area

Surface topography was measured with white-light interferometer after ultrasonic cleaning. Surface roughness rms was 1.6 nm and peak to valley value was 55 nm (**Figure 4.14a**). Even though nano-scale surface roughness was obtained, deep and shallow scratches, called polishing lines, were observed. During the material removal, ultra-fine abrasives scratched the surface. These scratches caused not only surface damage but also subsurface damage having serious effect on the detector quality. High abrasive concentration may have been the main reason of the scratches. The slurry mix ratio was

same with lapping procedure, but since the size was much smaller than lapping abrasives, there was more abrasive present inside the polishing slurry container.

Decreasing the Al_2O_3 concentration in DIW can be a solution to reduce scratch density. An alternative solution to remove scratches may be CMP in which ultra-fine abrasives exist inside proper chemicals.

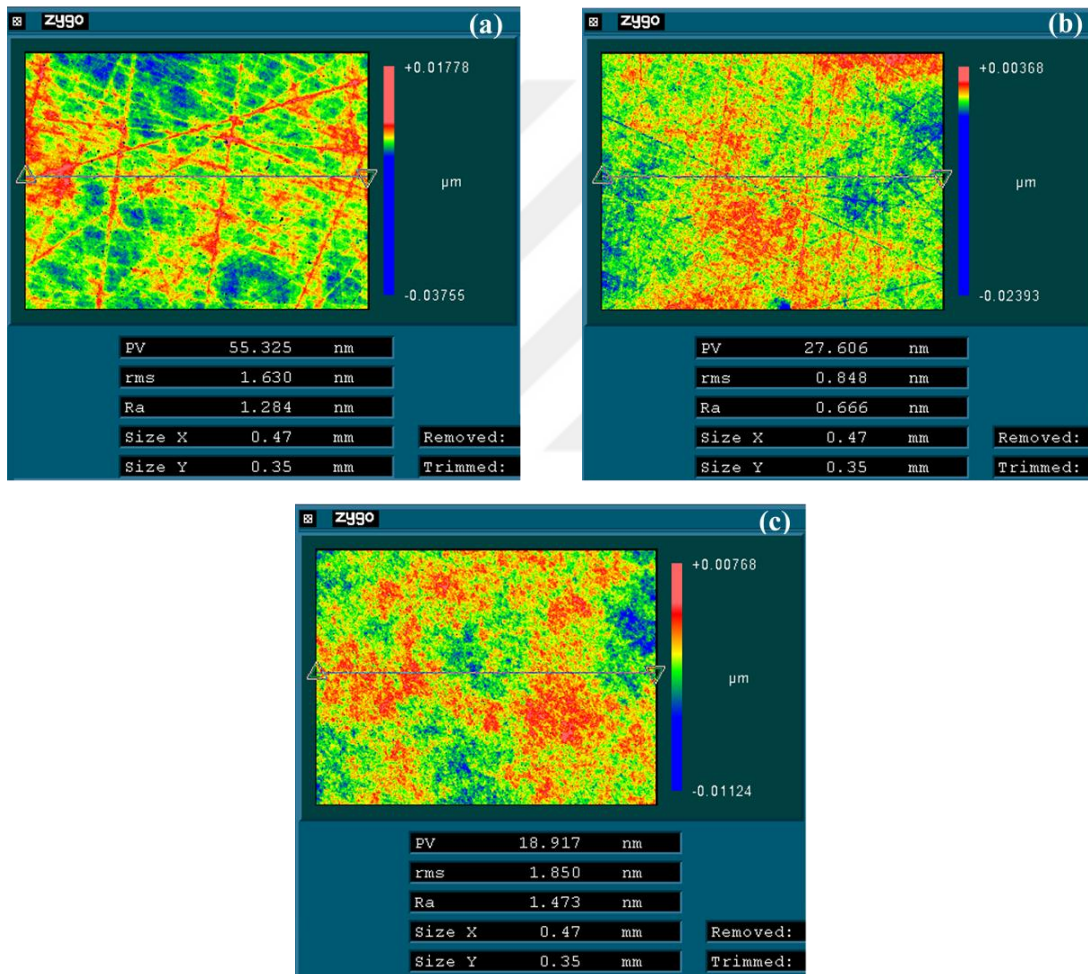


Figure 4.14 Surface topography measured with white light interferometer after $0.3 \mu\text{m}$ Al_2O_3 DIW mixture polishing (a) 15% v/o (b) 7.5% v/o, and (c) CMP with commercial solution

After mechanical polishing with 0.3 μm Al_2O_3 (7.5% v.) slurry, surface topography of crystal was presented in **Figure 4.14b**. In this case have reached sub-nanometer surface roughness rms value which was around 0.8 nm and the highest peak and lowest valley difference was 27 nm. Roughness value was significantly better than that of higher slurry mixture ratio. Density of polishing lines were reduced and this brought about lower surface roughness. However, there were still scratches on the surface; that is the polishing lines were not completely removed.

Different abrasive concentrations of slurries were prepared to compare the material removal rate and surface roughness (**Figure 4.15**). $\text{Cd}_{0.90}\text{Zn}_{0.10}\text{Te}$ crystals were used for this study. When the concentration of abrasive was increased inside DIW from 5% to 20%, the material removal rate also increased from 0.4 to 1.2 $\mu\text{m}/\text{min}$. Wafer polished with 5% (v/o) 0.3 μm Al_2O_3 and DIW mixture had 3.6 nm surface roughness. This value was much more than other concentration since removal rate was not enough to eliminate surface damages remained after lapping. On the contrary, the highest concentration caused higher roughness value due to higher possibility of abrasives embedding into the surface (left pits on the surface after cleaning) and scratches on the surface determining the surface roughness.

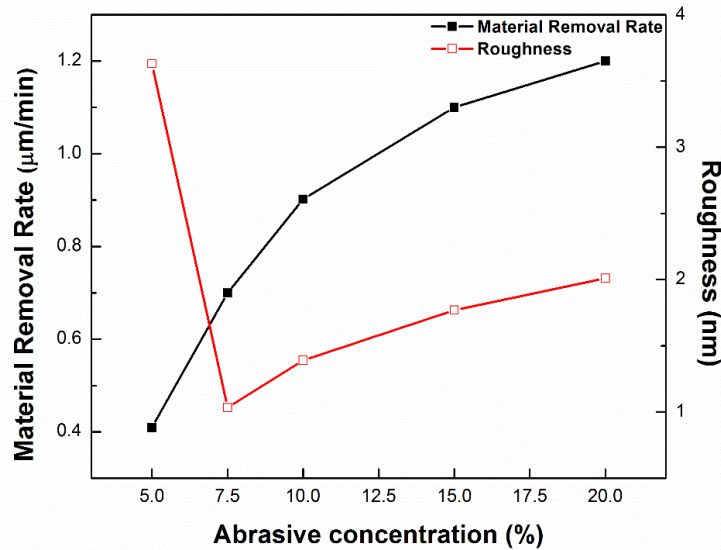


Figure 4.15 Material removal rate and roughness value under different 0.3 µm abrasive concentration

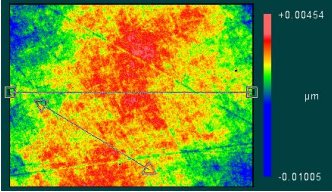
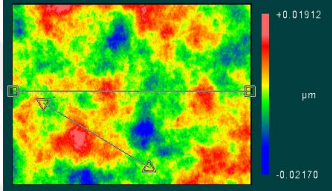
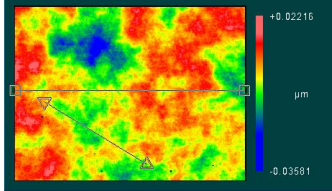
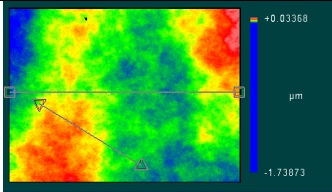
It was proved that surface roughness of crystals polished with higher concentrations create more scratches and subsurface damages. 7.5% (v/o) was found to be ideal for mechanical polishing. Furthermore, surface roughness lower than 0.8 nm could not be achieved with just mechanical polishing. Thus, CMP is required to obtain featureless surfaces with better roughness values.

Crystal surface can be polished with chemo-mechanically to remove scratches. For this purpose sodium hypochlorite (NaOCl) based commercial polishing slurry containing ultra-fine Al₂O₃ abrasives was used for CMP. Surface topography was analyzed with white-light interferometer (**Figure 4.14c**). Surface roughness value was nearly 1.8 nm. Difference between maximum and minimum value was reduced to 18.9 nm since there was no obvious scratches on the surface. Sodium hypochlorite oxidizes the surface and abrasives are responsible for material removal. Surface roughness increased when compared to mechanical polishing because chemical based solution polished the surface anisotropically (edge effect). Chemical reaction was faster on the edges of the samples.

Two main studies were planned based on total polishing times. The aim of these studies was to identify the optimum chemo-mechanical polishing time. In order to investigate the

edge effect, crystals were prepared with different time combination of mechanical and chemo-mechanical polishing providing that the total polishing time was kept constant for Study 1.

Table 4.7 Chemo-mechanical polishing optimization study 1

MP time (min)	CMP time (min)	Roughness (nm)	PV (nm)	Surface morphology
20	0	1.32	14.58	
15	5	5.27	40.81	
10	10	7.23	57.9	
5	15	10.75	1172	

Surface roughness and peak-to-valley values for various mechanical and chemo-mechanical polishing times are shown in **Table 4.7**. This study showed that surface morphology was getting worse by increasing chemo-mechanical polishing time. Differences between maximum height and minimum valley increased especially after 15-minute-chemo-mechanical polishing followed by 5- minute-mechanical polishing. It was

also found that the reason of higher roughness values may be due to shorter mechanical polishing times rather than optimized process times.

In study 2, mechanical polishing time was kept constant as 20 minutes and surfaces were chemo-mechanically polished for various times (**Table 4.8**).

With the increase of mechanical polishing time, surface morphology seemed to be smoother and scratches (polishing lines) were removed on the surface. Nevertheless, roughness and PV values are still high with additional chemo-mechanical polishing time.

Table 4.8 Chemo-mechanical polishing optimization study 2

MP time (min)	CMP time (min)	Roughness (nm)	PV (nm)	Surface morphology
20	5	1.85	18.917	
20	10	2.061	23.483	
20	15	3.14	26.014	

It was shown that surface roughness increased because of the dominant effect of CMP slurry to the surface. It was then concluded that this sodium hypochlorite based slurry was not proper for CdZnTe crystals and did not improve the surface roughness. The aim was to remove polishing lines and eliminate inclusions on the surface using chemicals. Almost

non-scratches surfaces were achieved since the chemo-mechanical fluid contains nano-sized abrasives. Nevertheless, high concentration of chemicals with high pH caused non-uniform surfaces and chemicals attacked to edges of the crystals. To eliminate warp on the surfaces, crystals were lapped with convex plate. Thus, surfaces of the polished samples were concave and this gave us an important advantage in the chemo-mechanical polishing because of edge effect.

Based on the feedbacks from commercial polishing solution, a NaOCl-based solution called CMP1 was developed. Crystals were chemo-mechanically polished with CMP1 under various time followed by 20 minutes mechanical polishing (**Figure 4.16a**). 10 minutes chemo-mechanical polished crystal had 0.87 nm surface roughness and 13.5 nm PV value. Increasing of chemo-mechanical polishing time to 20 minutes helped to remove scratches and created homogeneous surface topography (**Figure 4.16b**). Surface roughness-rms around 0.5 nm and 8.4 nm peak-to-valley value was achieved in a measured area $0.47 \times 0.35 \mu\text{m}^2$. Surface was atomically smooth and scratch free with this promising polishing solution.

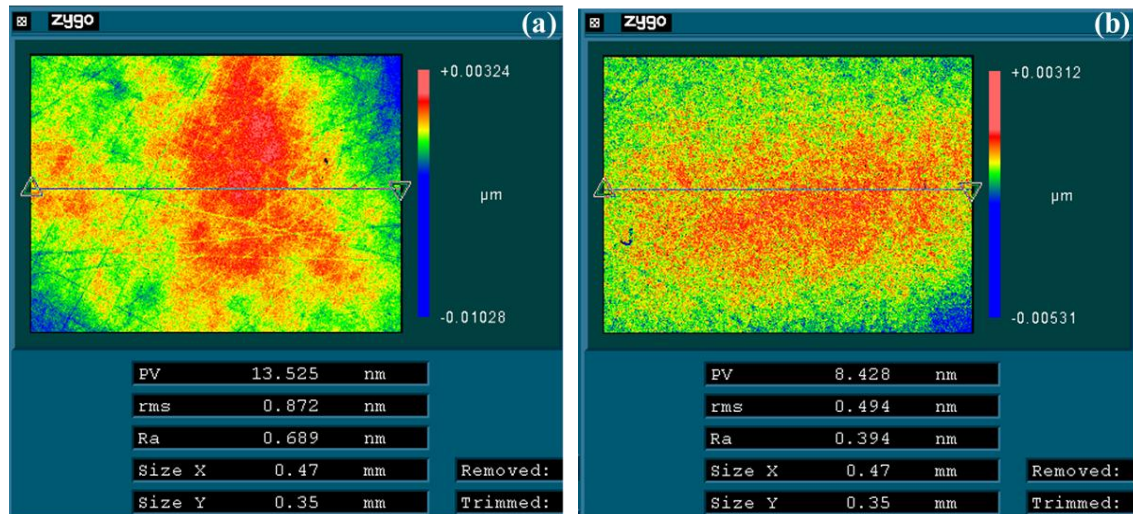


Figure 4.16 Surface topography of crystals polished with CMP1 (a) 10 minutes (b) 20 minutes

4.2.2.2 Surface Morphology Analyses of Polished Crystals

Surface morphology images were investigated by Optical Microscopy and SEM after mechanical polishing treatments with 1 μm and 0.3 μm Al_2O_3 abrasives (**Figure 4.17** and **Figure 4.18**). Material removal mechanisms were analyzed. Polishing lines, embedded abrasives, small size pits, and structural defects determining the overall surface roughness were examined extensively.

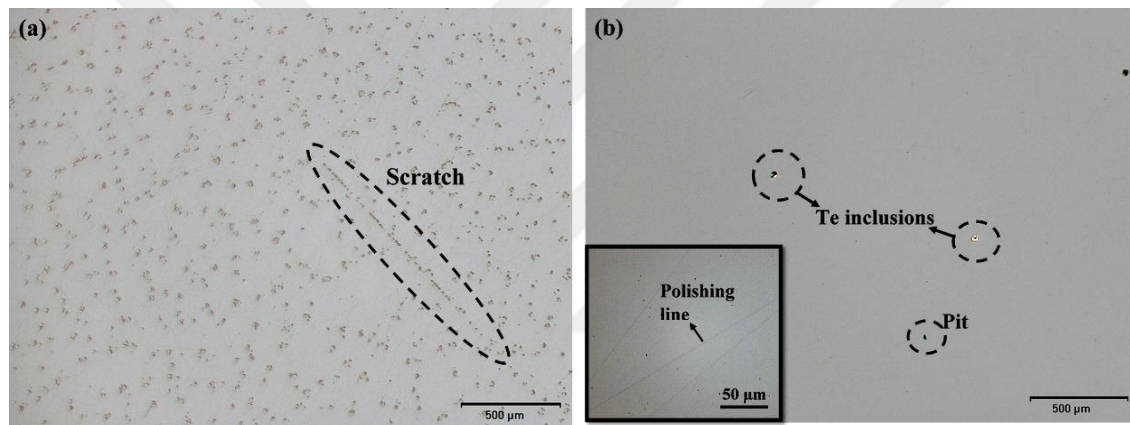


Figure 4.17 Optical microscope images of polished samples with (a) 1 μm Al_2O_3 , (b) 0.3 μm Al_2O_3

Figure 4.17a shows the surface morphology after 1 μm Al_2O_3 (i.e. rough polishing with coarse abrasives) mechanical polishing. Micro-scale CdZnTe particles aggregated all around the surface. Alumina abrasives were nested onto the clustered CdZnTe particles due to fractures created during polishing treatment.

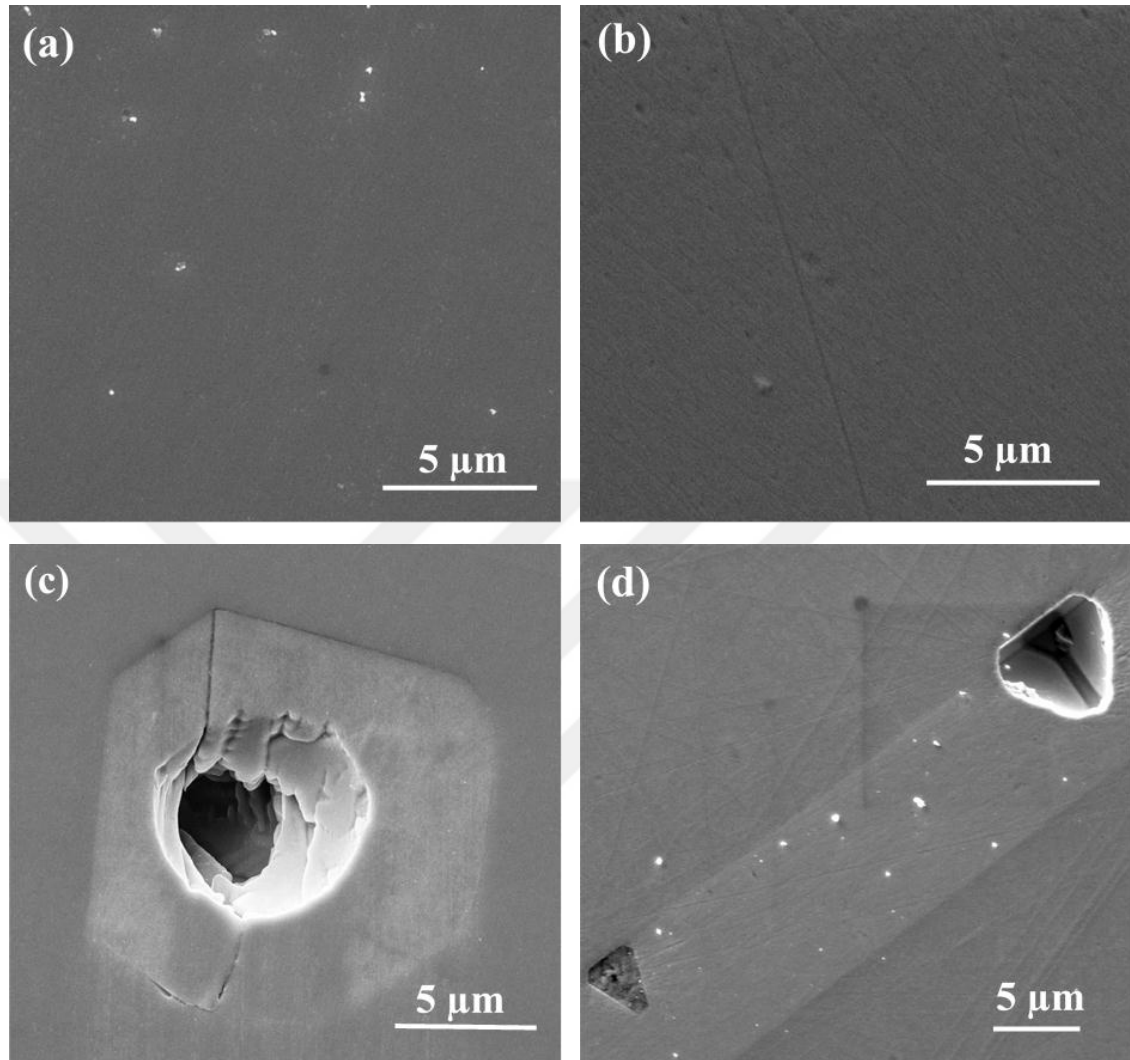


Figure 4.18 SEM images of polished samples with 0.3 μm Al_2O_3 abrasives

After 0.3 μm Al_2O_3 mechanical polishing, pits, inclusions, and polishing lines (scratches) were investigated on the surface (**Figure 4.17b** and **Figure 4.18**). If the surface are not cleaned carefully, sticking abrasives remains on the surface as shown in **Figure 4.18a**. Moreover, abrasive cleaning was one of the major issue after finishing of samples. Samples were cleaned ultrasonically with methanol after each polishing process. Abrasives are squeezed into the pores of polishing cloth; as a consequence, abrasives scratched the surface during stock removal. Lapping-induced micro-cracks, cleavages and chips were removed and rolling of abrasives became limited. Triangular and hexagonal shape inclusions were found on the surface.

Figure 4.18c and **Figure 4.18d** shows Te inclusions and dislocation line after mechanical polishing. Large hexagonal Te-inclusions with dimensions changing between 20 μm and 5 μm were observed. Inclusions had different structures like void, cavity, and purely occupied Te inclusions. Dislocation line was accompanied with Te inclusions. It is believed that voids inside the inclusions caused by surface preparation; however, inclusions were formed during the crystallization of the melt.

Surface morphology after CMP with modified polishing slurry was analyzed with SEM technique (**Figure 4.19**). It was clearly showed that there was topographical deformations near the edge. It is the proof of chemical solution attacked to the edge faster than the center. Around the center, surface scratches and were removed comparing with mechanical polishing. However, small stacked silica abrasives were captured on the surface. The size of abrasives changed between 80 nm and 20 nm. Ultrasonically cleaning of crystal inside methanol showed that abrasives were not embedded on the surface. Surface of cleaned sample had no scratches, abrasives or pits (**Figure 4.19c**).

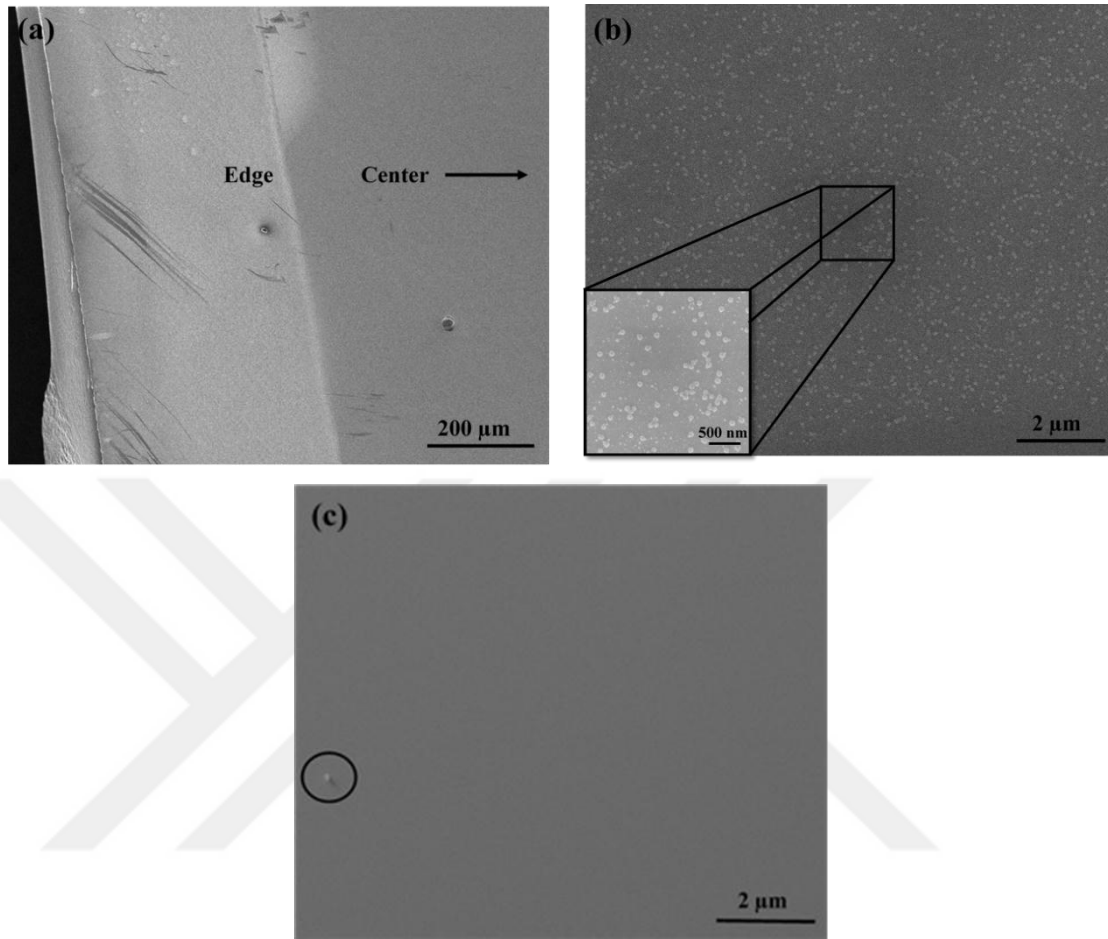


Figure 4.19 SEM images of chemo-mechanical polishing with modified solution (a) from edge and (b) from the center (c) cleaned surface

4.3 Structural Characterizations

In this part of our study, various techniques were employed to characterize finished surfaces in terms of structure and composition. These techniques inspected or described the surface and crystal quality. Results of these studies are presented below.

4.3.1 Crystal Orientation Studies with XRD method

Orientation of grains singled out from the unseeded grown CdZnTe ingots were unknown. As was described in ‘Slicing of CdZnTe Crystals’ at Chapter 3, twin formations were used to obtain {111}-, {220}- and {422}-oriented single crystals. This method was used until the employment of X-ray back reflection method from which large dimensions of crystals could be obtained and crystal preparation time was noticeably reduced.

It was given that XRD results of {211}-oriented slices obtained with these methods showed significant dissimilarities (**Figure 4.20**). MT5-RH1-G1-W1 was sliced with twinning method and MT3-RS2-G5-W2 was cut with the help of X-ray back reflection technique. 2Theta degree of {422} orientation for $\text{Cd}_{0.96}\text{Zn}_{0.04}\text{Te}$ is given as 71.29° [ref]. 2Theta degrees for MT5 and MT3 grown wafers were 71° and 71.35° respectively. Peak position may be moved due to misorientation from slicing. Comparing with these two methods, intensity of peaks was higher for MT3 wafer. Moreover, additional low intensity peaks detected from MT5-grown wafer were referred to {111}, (220), (311), (331), and (642) orientations respectively. Some minor peaks which cannot be seen easily were also observed from XRD measurements of MT3-grown as-cut wafer. Additional peaks may be arisen with misorientation due to slicing method or wire cutter’s performance during slicing explained in Chapter 3. Surface condition may be the reason of minor peaks though. Since as-cut surfaces were highly damaged due to diamond-wire tracks, x-rays may have been scattered from the surface.

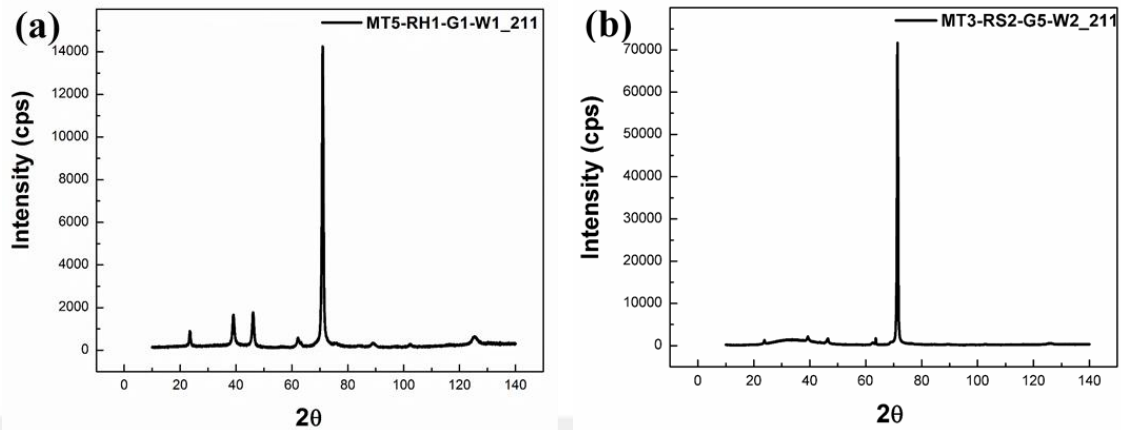


Figure 4.20 XRD measurements of (211)-oriented as-cut $\text{Cd}_{0.96}\text{Zn}_{0.04}\text{Te}$ slices (a) sliced with twinning method from MT5 (b) sliced with X-ray back reflection method from MT3

(111), (211), and (220)-oriented wafers can be sliced by twinning method, but (111) plane was twin plane created as defect formations on the grown ingot. Adjusting angles on goniometer during slicing process was completed by eye as precise as possible; hence, possibility of misorientation was increased with this method. One of the main aim of crystal growth was to obtain large single crystal yield without twin formation. Twinning method is limited by proper twinning formations. Thus, x-ray back reflection method is more preferable for CdZnTe crystals.

XRD measurements were repeated after each surface treatment for {111}-oriented $\text{Cd}_{0.96}\text{Zn}_{0.04}\text{Te}$ crystals (**Figure 4.21**). MT3-RS2-G7-W1 wafer was used. After polishing, additional peaks were disappeared and {111}-family peaks were moved to their peak position 2θ degrees. Since surface was extremely flat and damage free, measurements seemed to be more reliable.

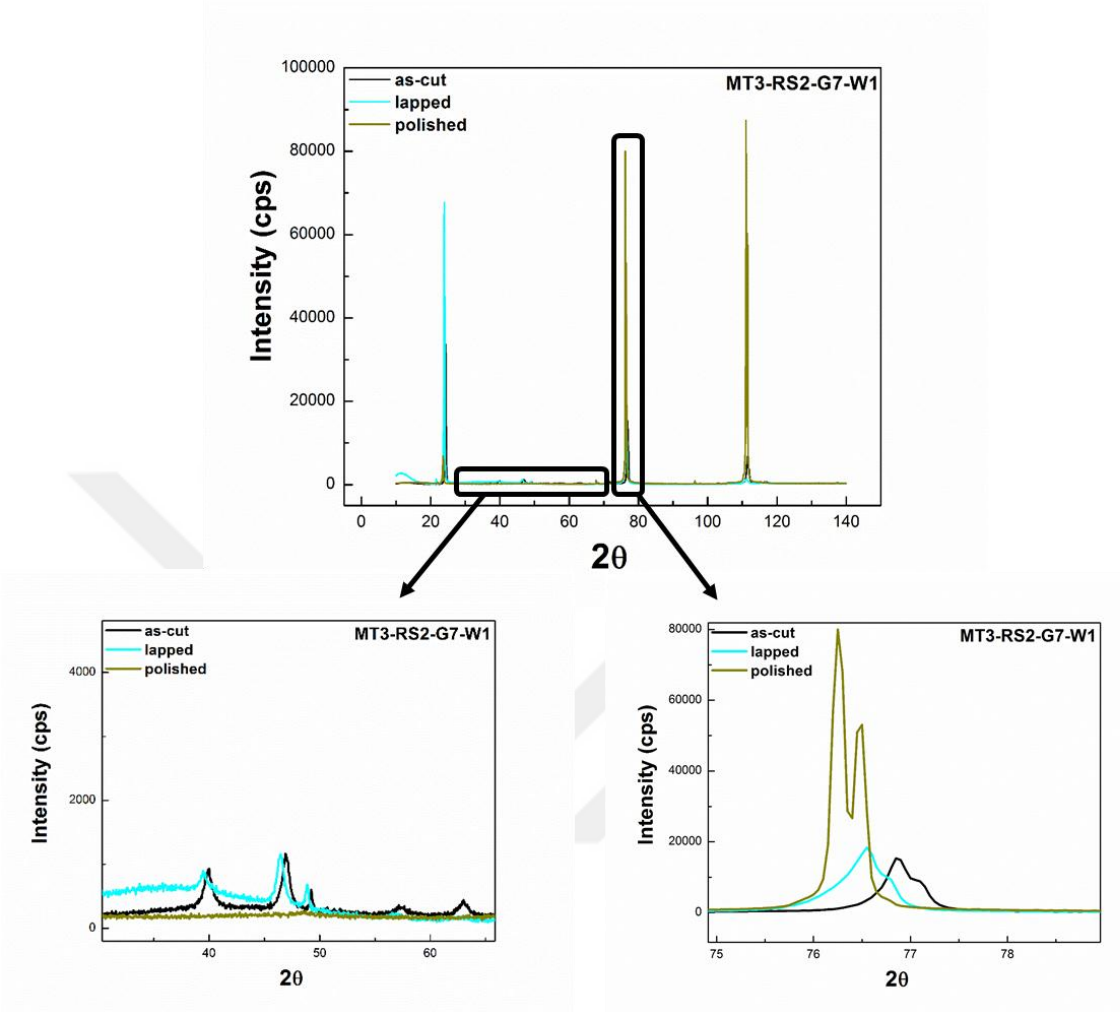


Figure 4.21 XRD measurements of {111}-sliced crystal after surface treatments

It was shown that additional peaks, {220}, {311}, and {331}, appeared after slicing with twinning method (**Figure 4.21**). Low-intense {331} peak vanished after 3 μm Al_2O_3 lapping. Therefore, all of the additional peaks were gone after polishing due to reduced scattering from the surface. A closer examination of (333)-orientation peak was given in **Figure 4.21**. Peak position moved to its corresponding position after each treatment and also the intensity of peak increased. Peak position of maximum intensity of finished surface was 76.25° which was very close to exact position.

4.3.2 Surface Composition of Crystals with EDX Method

To analyze surface composition, EDX method in which every element has a unique signature allowing a unique set of peaks on spectroscopy was employed and compositional analyses after lapping and polishing were conducted. MT12-RX7 sliced wafers from $\text{Cd}_{0.90}\text{Zn}_{0.10}\text{Te}$ ingot were used to analyze zinc distribution.

In addition to main elements of Cd, Zn, Te peaks, extra peaks were observed due to air and slurry exposure. Since lapping and polishing slurry included Al_2O_3 abrasive, Al and O peaks were also detected. This showed that residuals were adhered on the surface even after ultrasonic cleaning.

Atomic concentration of main elements and the ratio of overall Te to Cd+Zn were measured after each surface treatment (**Figure 4.22**). Same wafer was used during measurements in order not to be affected from the zinc segregation along the ingot. Zinc concentration varied from 8% to 13% during surface processes. It was expected that Te/Cd+Zn ratio was around 1 for stoichiometric surfaces. The ratios were observed to have changed between 0.92 and 0.98. It seemed that lapped surfaces was prone to be non-stoichiometric. Even so, the ratios were close to 1 after polishing procedures.

Zinc distribution of grown $\text{Cd}_{0.90}\text{Zn}_{0.10}\text{Te}$ crystal was determined to be nearly 10%. EDX spectroscopy was not sensitive enough to analyze chemical compositions of CdZnTe crystals due to at least 2% error.

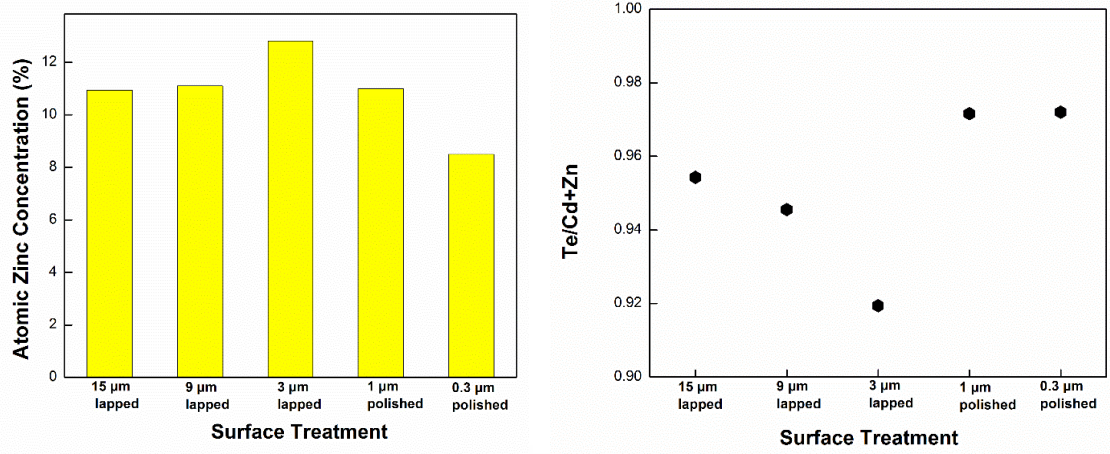


Figure 4.22 Left: Atomic Zinc concentration of $\text{Cd}_{0.90}\text{Zn}_{0.10}\text{Te}$ crystal after different surface treatments measured by EDX, Right: The ratio of overall Te to Cd+Zn chemical compositions measured by EDX spectra

MT4-grown $\text{Cd}_{0.96}\text{Zn}_{0.04}\text{Te}$ crystal was used to analyze stoichiometry of the surface after polishing. EDX was employed 4 different points with 4 different lines on the $20 \times 20 \text{ mm}^2$ wafer (**Figure 4.23**). Measurement showed that zinc distribution of $\text{Cd}_{0.96}\text{Zn}_{0.04}\text{Te}$ crystal was around 4% for all points.

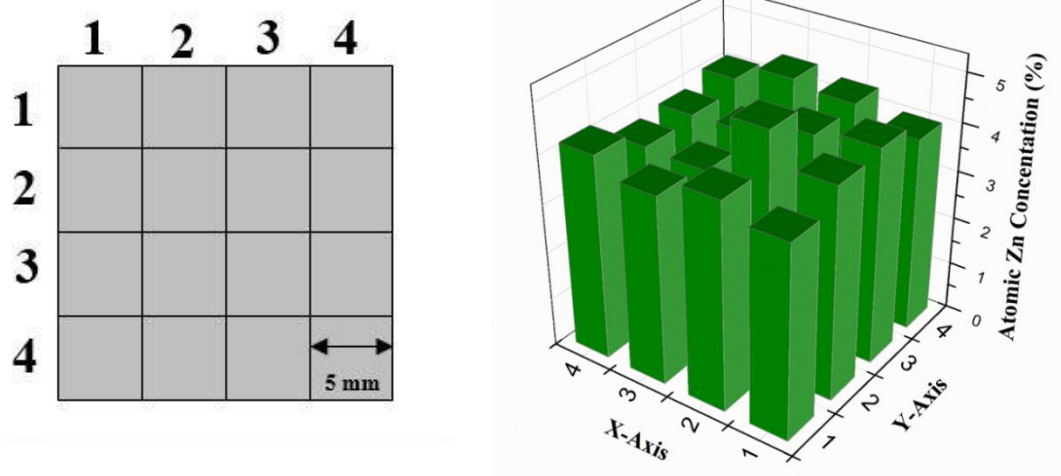


Figure 4.23 Atomic zinc concentration of polished $\text{Cd}_{0.96}\text{Zn}_{0.04}\text{Te}$ crystal from different point on the surface

4.3.3 IR Transmittance Studies

It was expected that IR transmittance for high quality CdZnTe crystals to be around 60% within the range 2-20 μm wavelength interval. The IR transmission spectra of different surface treatments are given in **Figure 4.24**. MT2-grown wafer was used to examine the effect of surface topography. In the range of 2-20 μm , IR transmittance of as-cut wafer changed between 14% and 23% which was very low. For the wavelength range from 2 μm to 10 μm , transmittance was again very low after final double-side lapping with 3 μm -sized Al_2O_3 abrasive. The IR transmittance was increased to 65% after mirror-like polishing with 0.3 μm -sized Al_2O_3 abrasive.

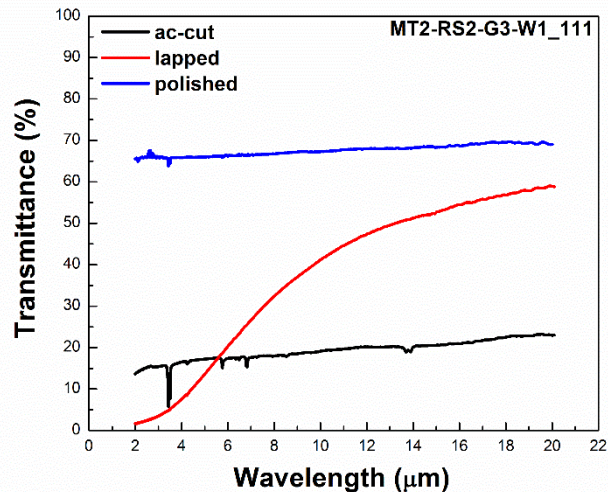


Figure 4.24 IR Transmittance measurements after surface treatments

Lapping process has a detrimental effect on IR transmission due to scattering losses from rough surface. Single-side polishing and double-side polishing was compared using MT2-grown wafer (**Figure 4.25a**). To achieve this, one surface of crystal was mirror-like

polished and the other-side was kept as 3 μm lapped. Obviously, non-reflective surfaces influenced the measurement. IR transmittance was very low for mid wave infrared region (i.e. 3-5 μm). However, IR transmittance value was almost constant within the range of longer wavelengths.

IR transmittance spectra of double-side grinded and double-side lapped crystals were shown in **Figure 4.25b**. While the transmittance was very low for 3 μm lapped surface, it was more than 60% and quite stable for grinded sample looked mirror-like with deep grooves. It can be deduced that both surfaces of crystal must be mirror-like to analyze the transmittance correctly. Otherwise, commenting on crystal quality cannot be certain. These investigations showed that the surface preparation was extremely important for the quality of characterizations and so detector performance.

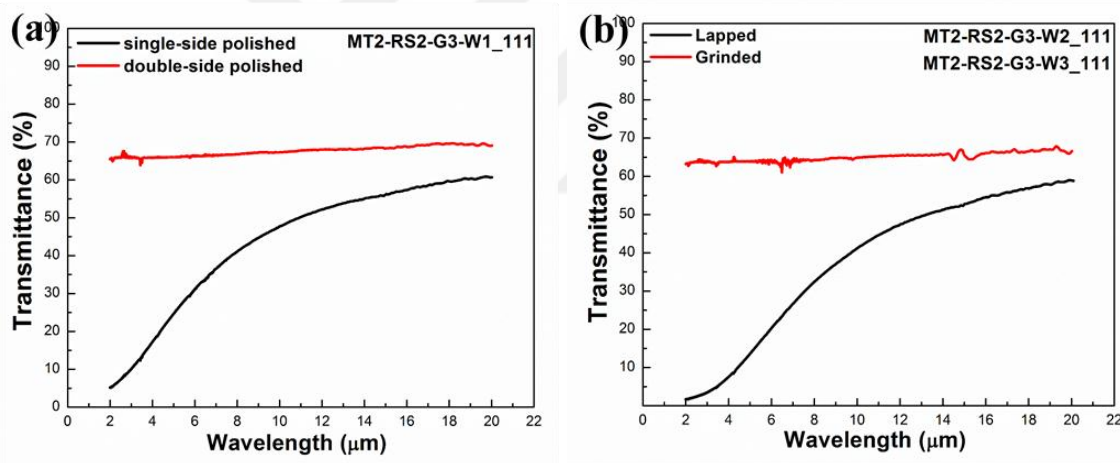


Figure 4.25 IR transmission measurements (a) polished surfaces (b) lapped and grinded surfaces

MT2-grown single-side polished (the other side was lapped) sample was chemically polished with Inoue's E-solution. Wafer was dipped into the chemical polishing solution without any machining steps. Wafer was dipped into E-solution for various times to observe the chemical polishing effect. IR transmittance at shorter-wavelengths (2-8 μm) was rapidly increased after chemical treatments **Figure 4.26**. The reason of the rise in transmittance was chemically polished of lapped surface providing almost a mirror-like surface. Nevertheless, chemicals attacked to the surface, after 120 seconds, the quality of

the surface in terms of topography and morphology was reduced. It was decided that double-side mechanical polishing was best option for IR transmittance measurements.

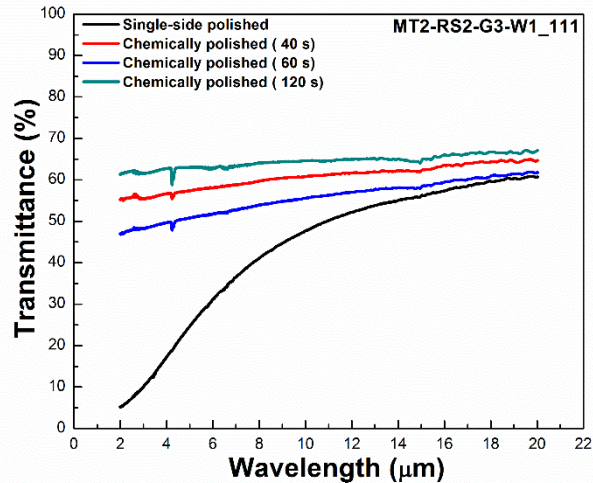


Figure 4.26 IR Transmittance measurements for chemical polishing studies

IR transmittance measurements were performed for double-side polished wafers cut from MT5- and MT8-grown $\text{Cd}_{0.96}\text{Zn}_{0.04}\text{Te}$ ingots with 880 μm thicknesses (**Figure 4.27**). It was obtained that IR transmittance was higher than 30% for MT5-grown {111} oriented crystal and IR transmittance was higher than 60% for MT8-grown {211} oriented crystal in the range of 2-20 μm wavelength. IR transmittance continuously decreased until 30% due to free carrier absorption for MT5-grown crystals. This decreasing of IR transmittance at long wavelengths ($>10 \mu\text{m}$) may have been caused by the low crystal quality and micro-defects existing in the crystal.

Hence, in order to confirm this, crystals were chemically etched for micro-defect revealing in the crystals. Everson etching was applied for 5 minutes. Defect formations of triangular etch pits were produced on the surface and etch pit density (EPD) of crystals were correlated with IR-transmittance (**Figure 4.27**). While deep and shallow equilateral triangles pits were counted over the surface of MT5-grown wafer and EPD was calculated around $\sim 10^5 \text{ cm}^{-2}$. EPD of MT8-grown wafer was around $\sim 10^4 \text{ cm}^{-2}$. Thus, IR-

transmittance measurements have been confirmed with EPD characterizations for crystal quality.

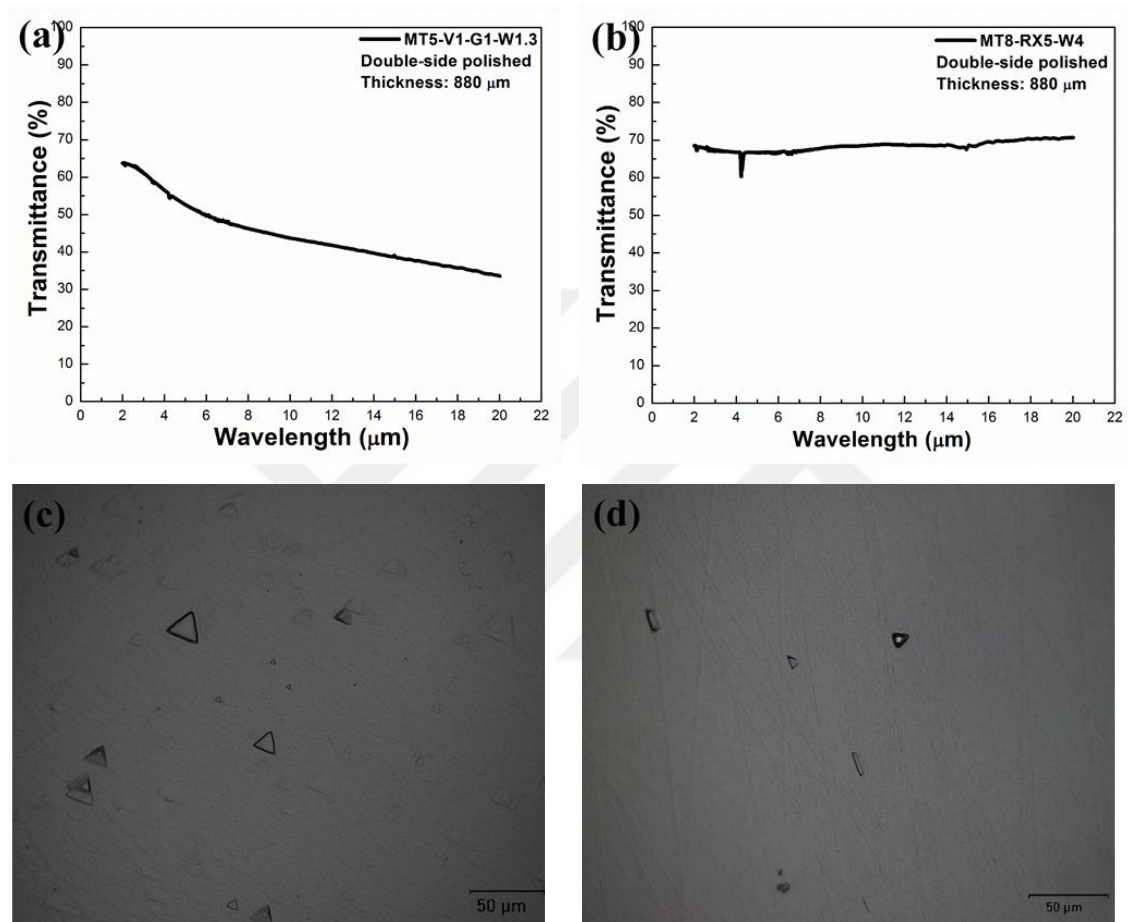


Figure 4.27 IR Transmittance and EPD measurements for (a), (c) MT5-grown ingot and (b), (d) MT8- grown ingot

4.3.4 Chemical Etching for Defect Characterizations

High quality CdZnTe detectors must have low dislocation and inclusion density. The density of dislocations was revealed by chemical etching for different oriented crystals. Surface of crystals should be mirror-like polished to clearly distinguish dislocations etch pits on the surface.

Etch pit formation of different crystallographic oriented wafers had characteristic shapes since pits were formed according to Thomson tetrahedron. Various oriented crystals from $\text{Cd}_{0.96}\text{Zn}_{0.04}\text{Te}$ grown ingots different were chemically etched with Inoue etchant (EAg-2) because of its compatibility to all orientations (**Figure 4.28**).

According to Inoue, shape of pits were depend on crystal orientation. Pits grown on the Thomson tetrahedron. The characteristic shapes of pits on the (111), (110), and (100) surfaces are equilateral triangle, isosceles triangles with 70.6° , and rectangular dislocation pits respectively. In **Figure 4.28**, it was observed that pits exactly what Inoue said. Small size equilateral triangles leagued together and created bigger size equilateral triangles on the surface of $\{111\}$ B. Moreover, small sized isosceles triangles gathered and they formed like uncompleted isosceles triangles on the surface of $\{211\}$ B. Rectangle shape pits with line in showed anisotropically etching on the surface of $\{100\}$. Isosceles triangles with the angle of 71.15° on the surface of $\{110\}$. The angle value is very close to theoretical value. The sample sliced with twinning method and this lead to a few degree of misorientation. Since different oriented samples were sliced and prepared from different MT-growths, dislocation density and size of the pits may change the according to growth quality.

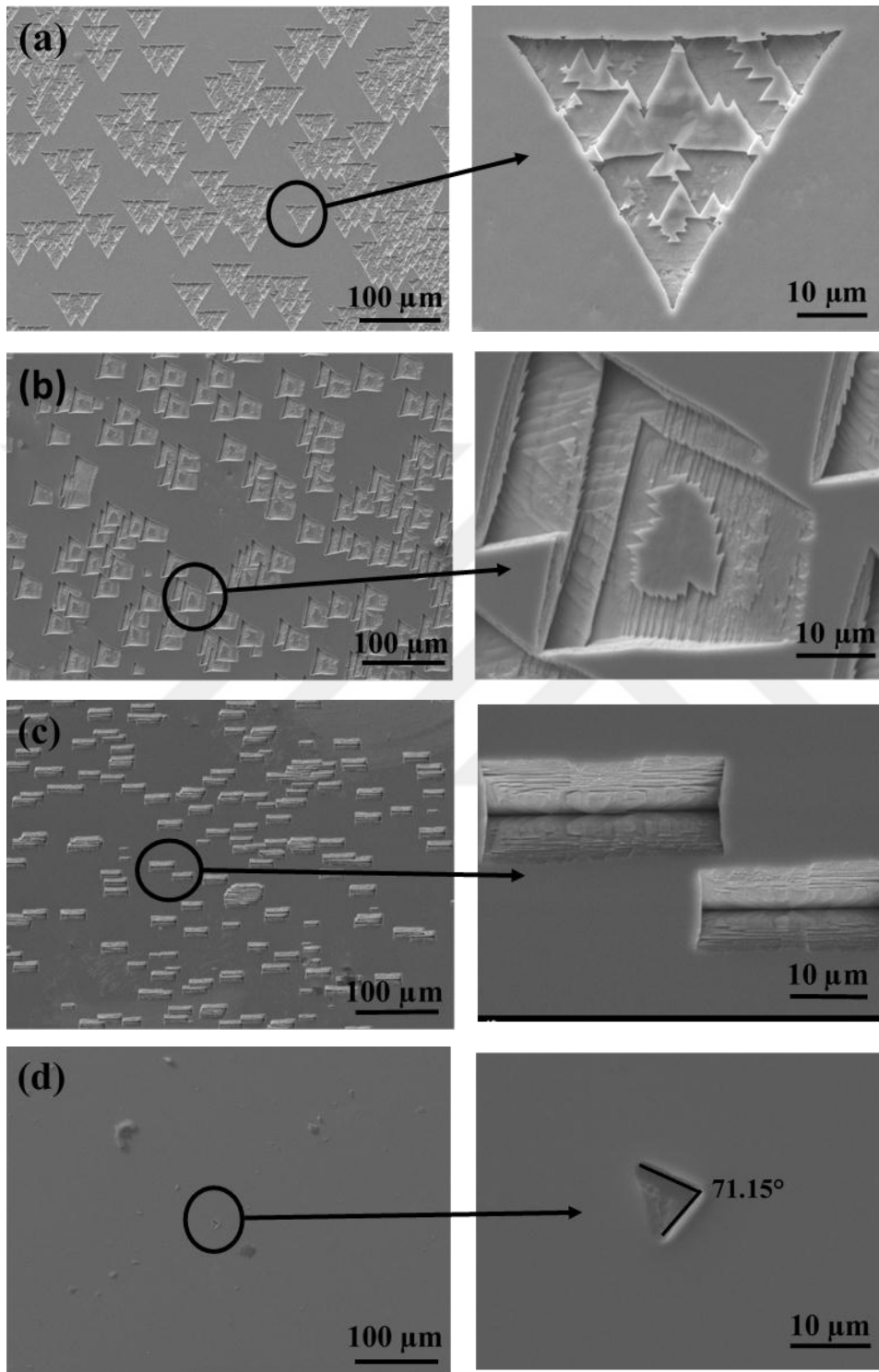


Figure 4.28 Inoue etchant applied to different crystallographic orientations (a) {111}-orientation, (b) {211}-orientation, (c) {100}-orientation, and (d) {110}-orientation

Inclusions were observed after chemical etching. Morphology of micro-scale inclusions was captured with SEM. Inclusions were analyzed with EDX spectrum to present atomic percentages. The composition of inclusion was determined with EDX mapping measurement. Atomic composition of hexagonal-shaped Te inclusion with a size of about 10 μm (**Figure 4.29**) was given in **Table 4.9**.

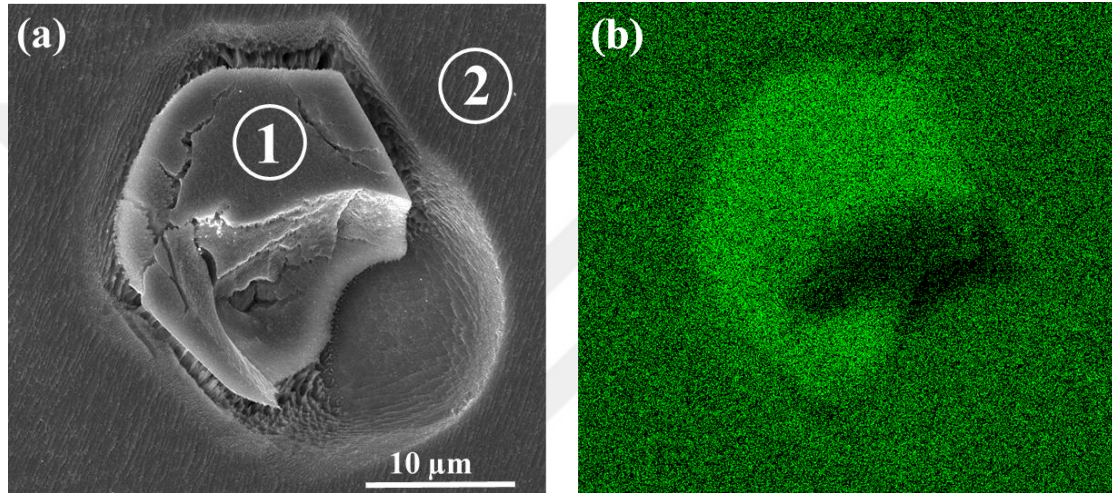


Figure 4.29 Te inclusion (a) SEM image (b) EDX mapping

Table 4.9 Composition analyses of $\text{Cd}_{0.96}\text{Zn}_{0.04}\text{Te}$ crystal and inclusion

Region number	Cadmium Atomic %	Zinc Atomic %	Tellurium Atomic %
(1)	0	0	100
(2)	46.5	2.1	51.4

Te-inclusions appeared during mechanical polishing and were removed by chemo-mechanical polishing mentioned in **Chapter 4.2**. Removed inclusions left large pits. Crystals sliced from MT5 and MT10-grown ingots were etched with Nakagawa and Everson etchants. Inclusions were investigated before and after etching. Exactly the same Te-inclusions were captured with SEM (**Figure 4.30** and **Figure 4.31**).

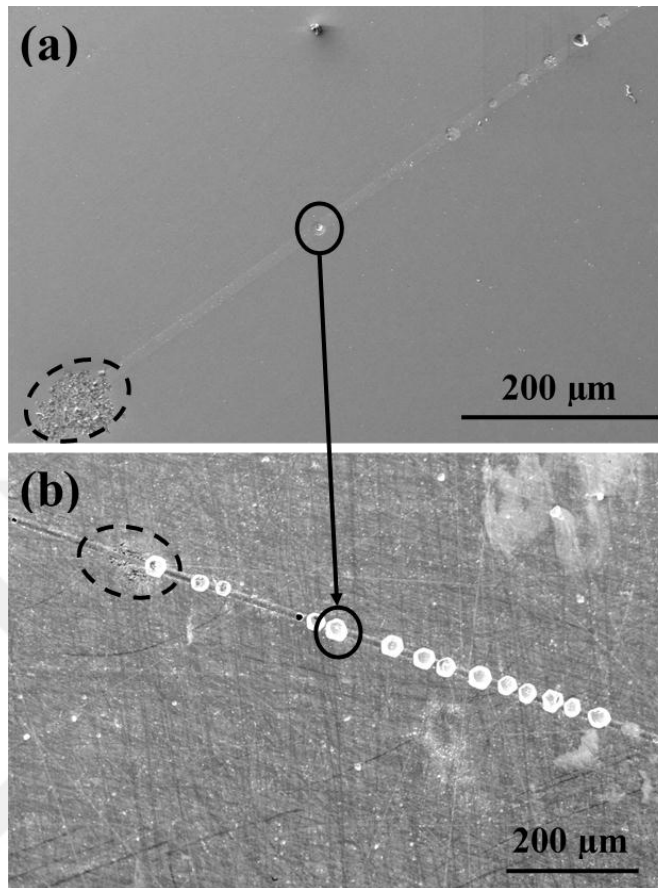


Figure 4.30 Te inclusions decorated with dislocation line from MT5-grown ingot (a) after 0.3 μm Al_2O_3 mechanical polishing (b) after Nakagawa etching

Te-inclusions in the matrix induced dislocation line was shown in **Figure 4.30**. Crystal was chemically etched with Nakagawa solution for 2 minutes. Exactly same inclusions and dislocation line was observed after etching. Te-inclusions disappeared leaving behind empty hexagonal shapes along the dislocation line. Chemicals of Nakagawa solution (H_2O_2 as oxidant) may have attacked to the inclusions.

Te-inclusions after mechanical polishing (**Figure 4.31a**) and chemo-mechanical polishing with CMP1 solution (**Figure 4.31c**) were investigated. While half-filled Te-inclusion was observed after mechanical polishing, empty hexagonal-shape was seen after the chemo-mechanical polishing, since chemicals attacked to the inclusion. Crystals were etched with Everson solution for 5 minutes. Similar hexagonal-shaped inclusions were observed after dislocation. In this case, Te-inclusion was revealed more clearly (**Figure 4.31b**). In **Figure**

4.31d, edges of hexagonal-shape became sharper and direction of edges is $\langle 110 \rangle$. Cavities were bounded by triangular and square faces. Everson etch may have revealed inclusions more clearly (HNO_3 as oxidant) since its etch rate is several micrometers per minute for CdZnTe matrix so that inclusions are exposed more easily.

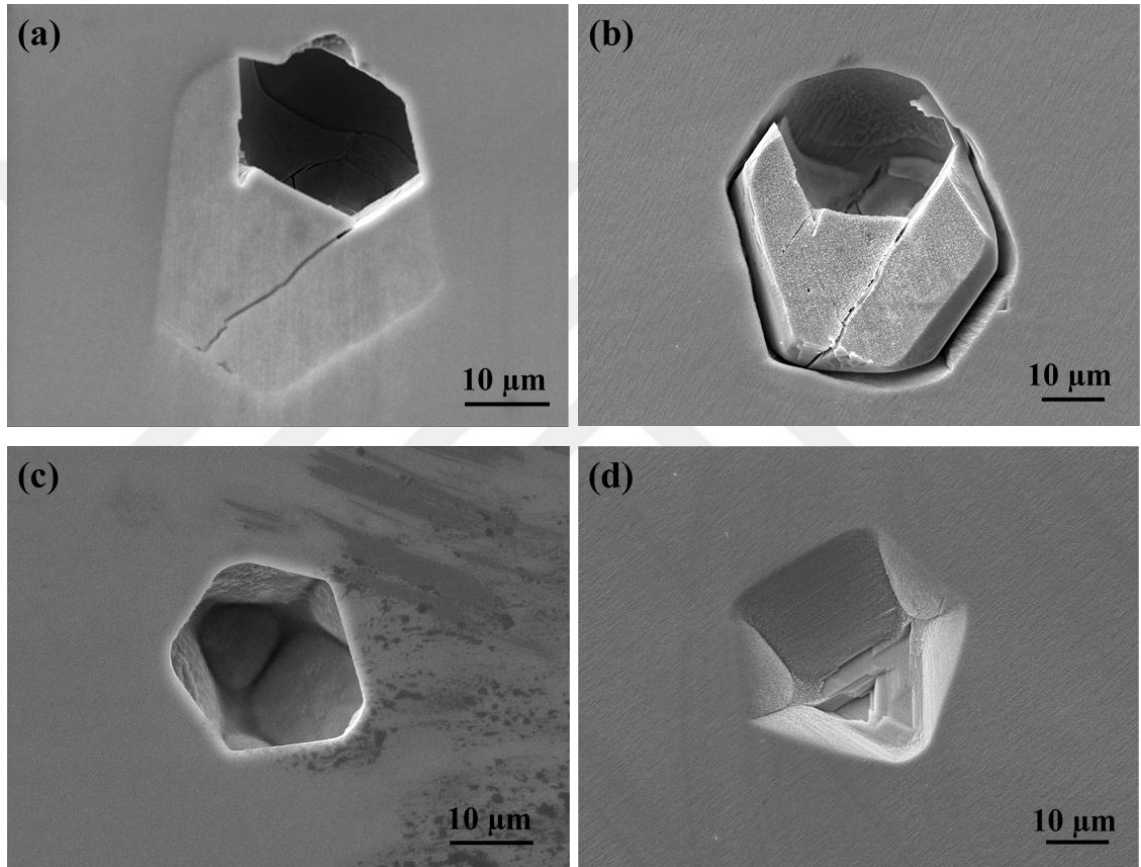


Figure 4.31 Te inclusions from MT10-grown ingot (a), (b) same Te-inclusion after mechanical polishing and Everson etching (c), (d) same Te-inclusion after chemo-mechanical polishing and Everson etching

Optical microscope was used to analyze the depth of inclusions. Nakagawa etched crystal from MT5 and Everson etched crystal from MT2 were analyzed (**Figure 4.32**). Depth of inclusion pit was around $9 \mu\text{m}$ (**Figure 4.32b**). Most probable reason for the removal of inclusions is that chemicals etched Te-inclusion faster CdZnTe for Nakagawa solution. Te-inclusion with etch pit rosette was observed with optical microscope. Height of the

inclusion was nearly $2.5\ \mu\text{m}$ (**Figure 4.32d**). It was concluded that the etch rate of CdZnTe crystal was higher than Te inclusion for Everson etchant.

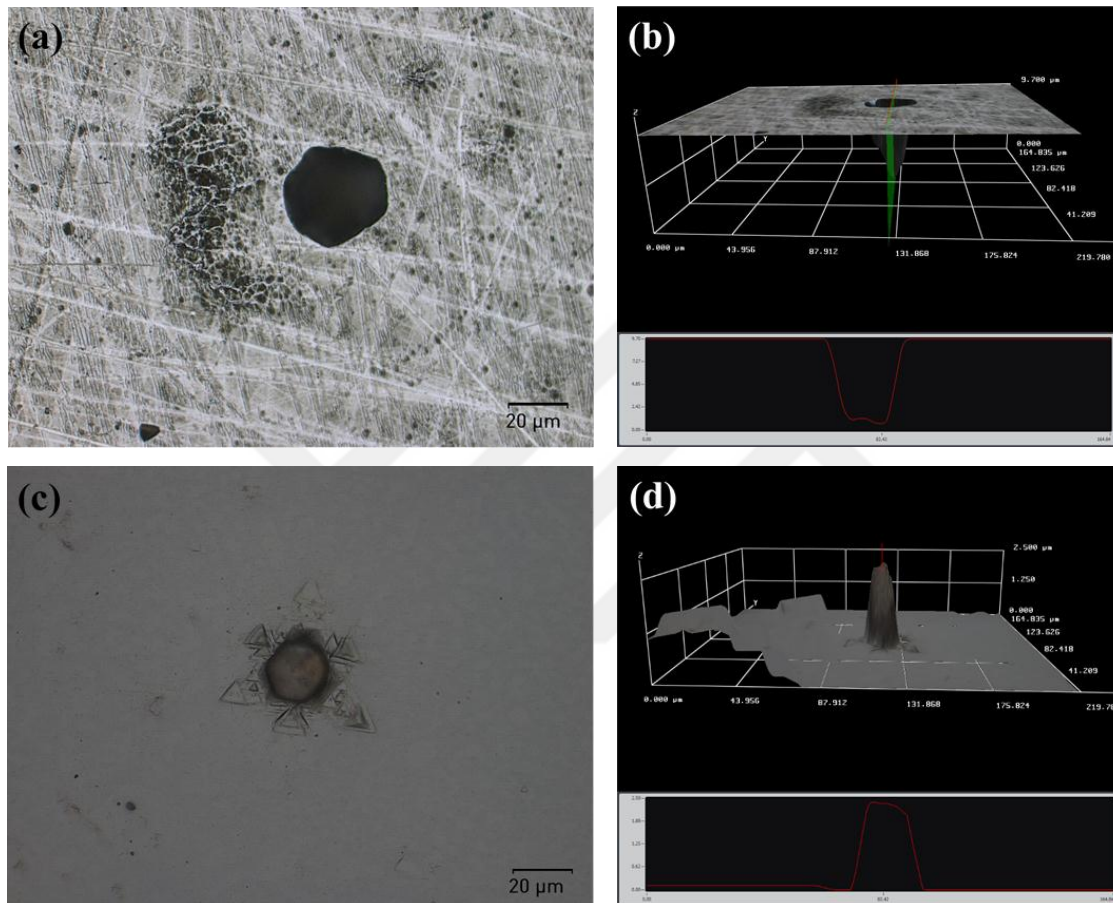


Figure 4.32 Te-inclusion depth analyses (a), (b) after Nakagawa etching to MT5-grown wafer (c), (d) after Everson etching to MT2-grown wafer

4.4 Nano-mechanical Characterizations

The nano-mechanical properties of $\{111\}$ -, $\{211\}$ -, $\{100\}$ -, and $\{110\}$ -oriented $\text{Cd}_{0.96}\text{Zn}_{0.04}\text{Te}$ crystals and also $\{211\}$ -oriented $\text{Cd}_{0.90}\text{Zn}_{0.10}\text{Te}$ crystals were measured by nanoindentation. In this measurements, increased force were applied on the surfaces and indentation displacement was measured correspondingly.

It was shown that as experimental results, when indentation load increased, hardness and elastic modulus decreased for different kinds of CdZnTe crystals (**Figure 4.34**). This phenomena is called indentation size effect related to changing mechanical properties due to residual stress and plastic deformations [58]. Sub-nanometer machining damage layer exist near the surface; so lower subsurface has higher deformation energy. Therefore, increasing displacement generate lower hardness and elastic modulus [16].

Force displacement curve of {111}-oriented Cd_{0.96}Zn_{0.04}Te crystal showed that pile-up phenomena was observed for higher forces (≥ 5 mN) due to plastic deformation (**Figure 4.33**). Since displacement of 1 mN force was near the machining surface and it was not influenced by pile-up, 1 mN force ideal to decide nano-hardness and elastic modulus. Hardness and elastic modulus of {111}-oriented Cd_{0.96}Zn_{0.04}Te crystal were 1.25 GPa and 63 GPa respectively.

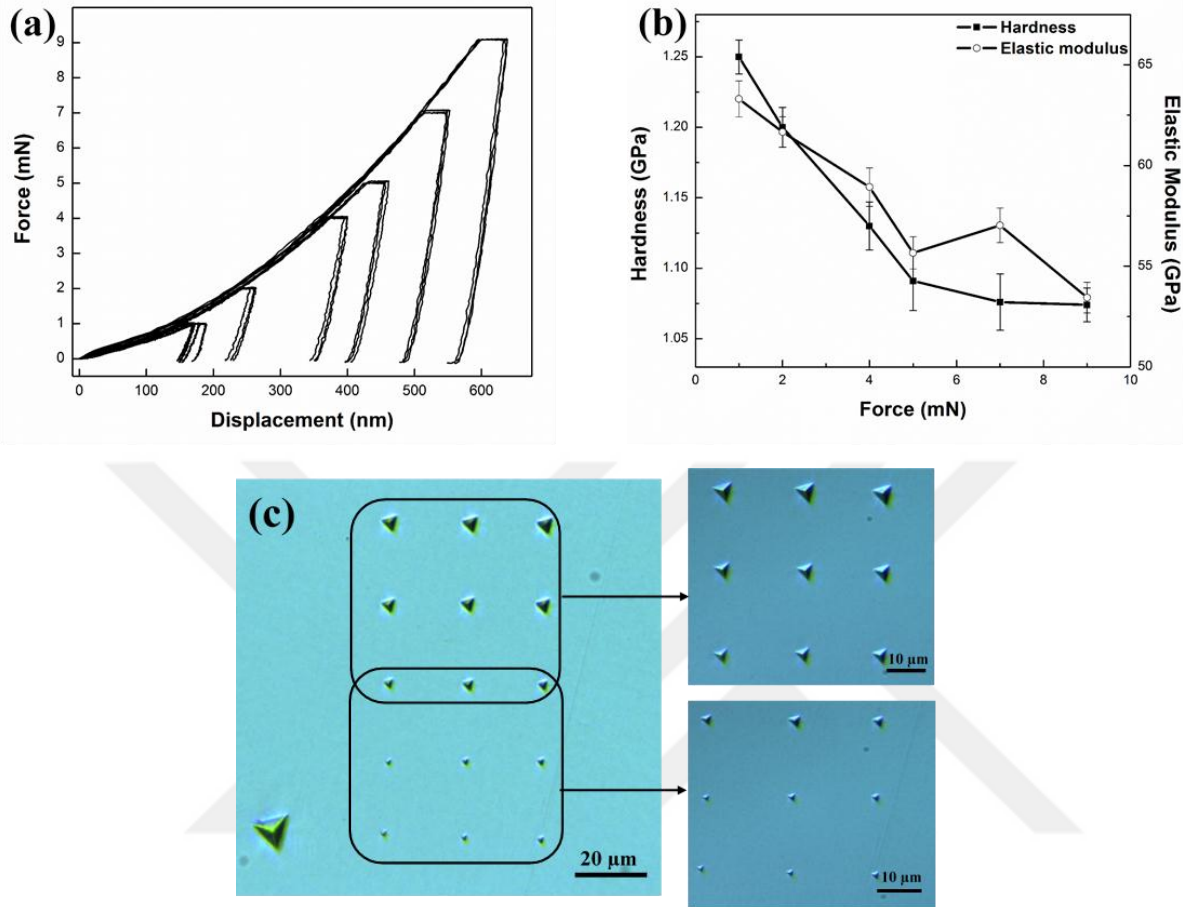


Figure 4.33 Nano-indenter measurement for {111}-oriented $\text{Cd}_{0.96}\text{Zn}_{0.04}\text{Te}$ crystal (a) Load-displacement curve (b) Hardness and elastic modulus measurements, and (c) Optical microscope images

Hardness and elastic modulus of {211}-, {100}-, and {110}-oriented crystals measured with different applied force. Hardness and elastic modulus of various crystallographic orientations were different due to anisotropy of CdZnTe crystals. Hardness and elastic modulus of {211}-, {100}- and {110}-oriented $\text{Cd}_{0.96}\text{Zn}_{0.04}\text{Te}$ crystals were 1.21 GPa, 54.17 GPa; 1.17 GPa, 49.83 GPa; and 1.08 GPa, 49.63 GPa, respectively. Since {110} planes has lower atomic density than other measured planes, hardness and elastic modulus are the lowest for {110}. As mentioned in **Section 4.1**, differences of mechanical properties influences crystal machining. It was proven that material removal rate is higher for the planes having lower hardness.

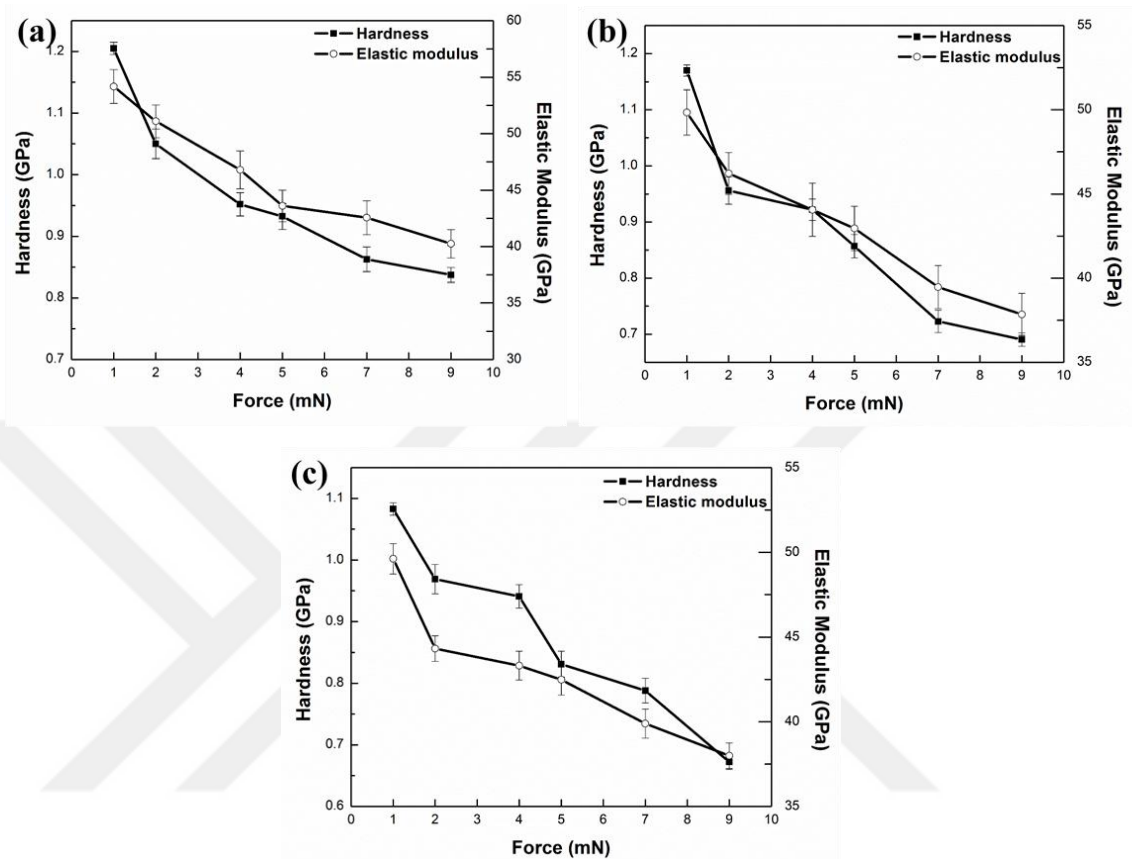


Figure 4.34 Hardness and elastic modulus measurements under different force for (a) {211}-oriented (b){100}-oriented, and (c) {110}-oriented $\text{Cd}_{0.96}\text{Zn}_{0.04}\text{Te}$ crystals

{211}-oriented $\text{Cd}_{0.90}\text{Zn}_{0.10}\text{Te}$ crystal were used to compare the effect of Zn-concentration on nano-mechanical behavior (**Figure 4.35**). It was found that {211} $\text{Cd}_{0.90}\text{Zn}_{0.10}\text{Te}$ had hardness of 1.08 GPa and elastic modulus of 59.68 GPa. Increasing of Zn concentration has tendency to decrease the hardness. In $\text{Cd}_{1-x}\text{Zn}_x\text{Te}$ crystal structure, Cd atoms are substituted by Zn atoms. CdZnTe crystals belong to II-VI soft-materials and also Cd and Zn atoms are from IIB group in periodic table. Even though Cd and Zn atoms have similar physical and chemical properties, atomic radius of Cd atoms are higher than Zn atoms. Therefore, bond energy between Cd and Te atoms are higher than bond energy of Zn-Te. Increase of zinc concentration leads to weaker bonding of elements and this is the main reason of decreasing of hardness.

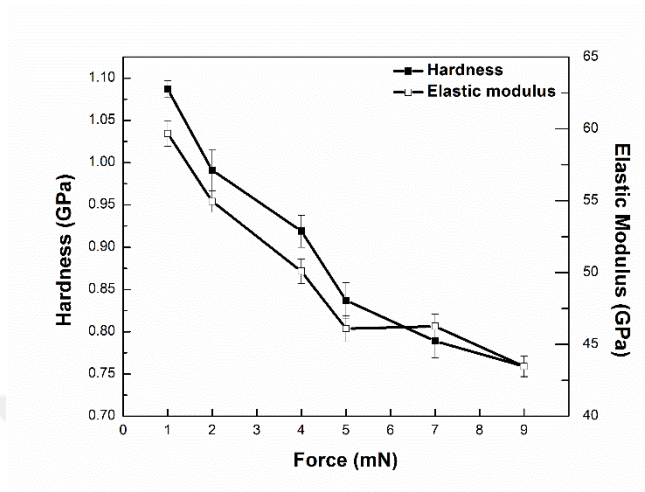


Figure 4.35 Hardness and elastic modulus measurement for {211}-oriented $\text{Cd}_{0.90}\text{Zn}_{0.10}\text{Te}$ crystal

4.5 Subsurface Damage Analyses

Damage layer under the surface deteriorate the detector performance. Subsurface damage (amorphous layer) was introduced into the crystals during slicing. Crystals were lapped to decrease subsurface damage. Subsurface damage was almost reduced through mechanical polishing with ultra-fine abrasives. Subsurface damage in the form of micro-cracks after the lapping process are given in **Figure 4.36**.

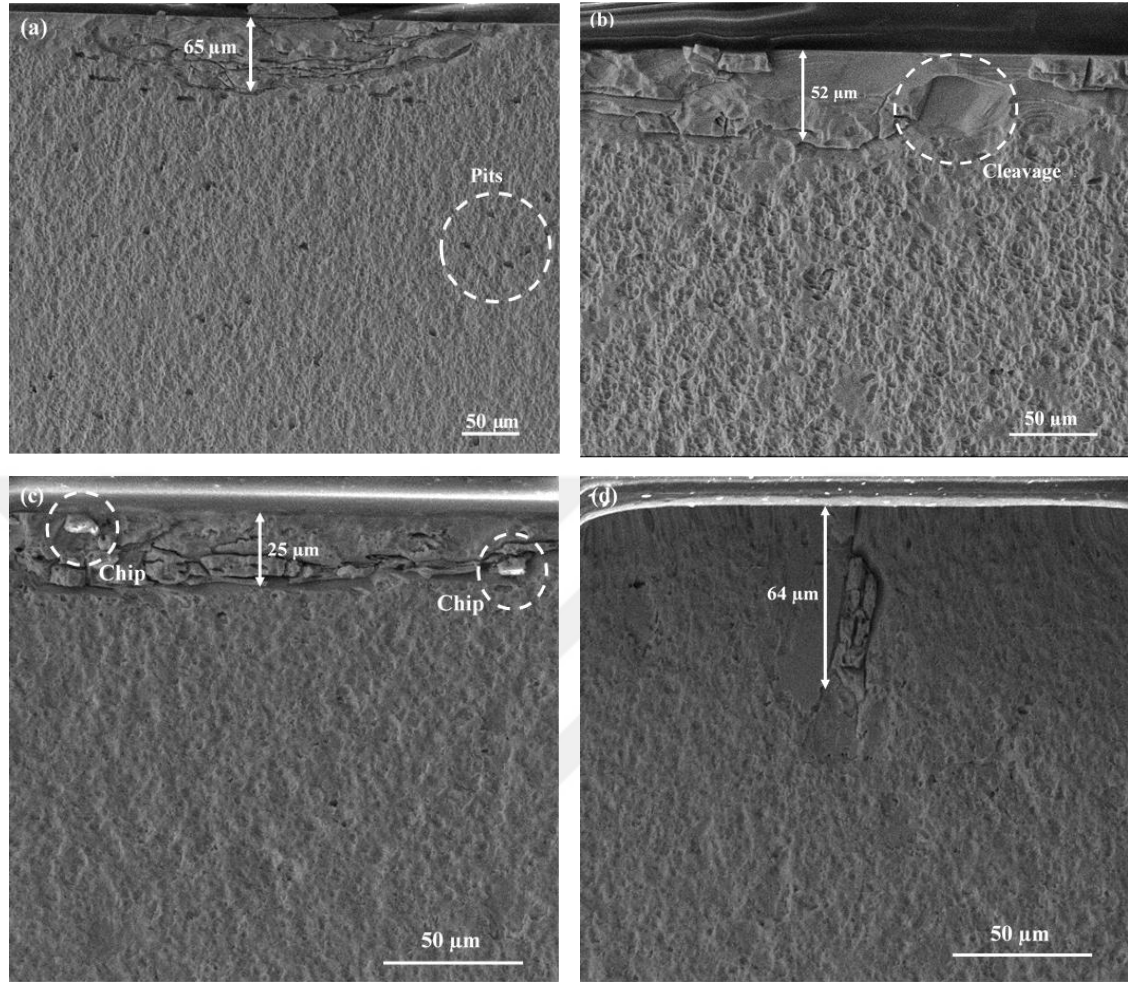


Figure 4.36 Subsurface damages of CdZnTe (a), (b) 9 μm Al_2O_3 lapped and (c), (d) 3 μm Al_2O_3 lapped

SEM pictures of the cross-section of the samples processed with different abrasive particle sizes are shown in **Figure 4.36**. Cracks, pits, chips and cleavages were observed on all lapped surfaces. In **Figure 4.36a** lateral cracks parallel to the surface with maximum depth of 65 μm were investigated. Pits are formed after the etching for damage revealing. About 26 μm x 36 μm cleavage was also present in addition to lateral cracks following the 9 μm Al_2O_3 lapping process (**Figure 4.36b**). Subsurface damage depth changed from 40 μm to 65 μm , and mostly lateral cracks caused by material removal mechanism for brittle material like indentation effect were observed.

Subsurface damage depth of lateral cracks was reduced to 25 μm after 3 μm lapping (**Figure 4.36c**). Chips again were again formed inside the cracks. Median crack depth of 64 μm was found to be normal to the surface (**Figure 4.36d**). The reason of median cracks could be the stress intensity of ductile removal mechanism on soft-brittle CdZnTe (i.e. strength degradation in brittle materials).

Figure 4.37 shows that subsurface damage layer after mechanical polishing. 2.5 μm damage layer was measured after 1 μm polishing. Damage layers was solely composed of curly, thin lines at nano-scale (**Figure 4.37a**). After 0.3 μm polishing, these lines seemed to be completely avoided (**Figure 4.37b**) except only one location (**Figure 4.37b** inset). It is more likely that clear visualization of subsurface damage after the fine mechanical polishing may not be applicable with this method.

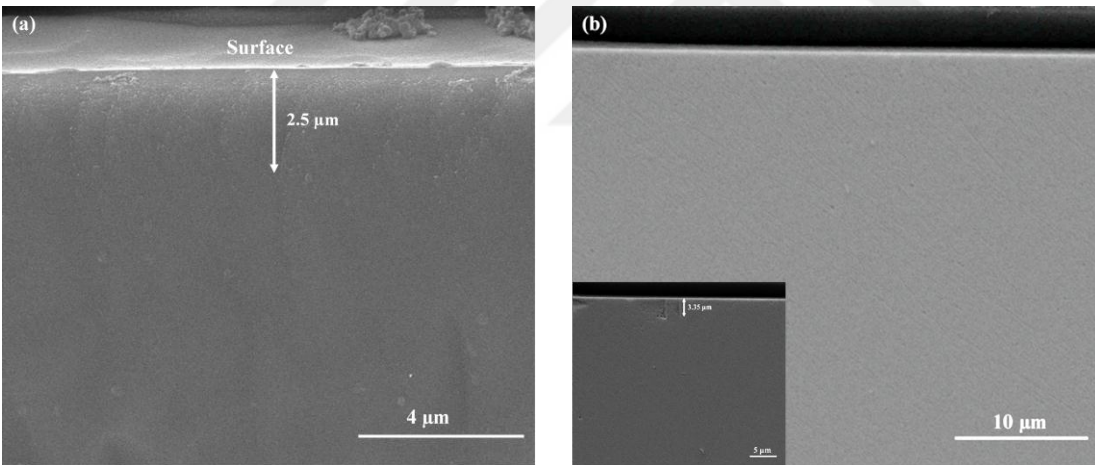


Figure 4.37 Subsurface damages of CdZnTe (a) 1 μm Al_2O_3 polished, (b) 0.3 μm Al_2O_3 polished

CONCLUSIONS

In this study, wafering and surface finishing studies were intensively conducted. Atomically smooth wafers up to $20 \times 30 \text{ mm}^2$ were produced from grown CdZnTe ingots. The following conclusions summarize the results that investigated through this study.

Wafering studies were conducted with two different slicing methods. In twining method, twin formations was used that lied on $\{111\}$ plane and grown along $\{211\}$ direction. Twin lines were aligned parallel to the wire by three axes of goniometer. Small size of wafers ($10 \times 10 \text{ mm}^2$) were sliced with this method; however, the possibility of misorientation was increased since alignment were conducted by eye. In conventional x-ray back reflection method, x-rays reflected from selected grain and mathematical software gave possible solutions for desired orientation. Any crystal orientation can be aligned more precisely. The main advantage of this method is that multi-slicing can be performed and the number of wafers with large area ($\geq 20 \times 20 \text{ mm}^2$) may increase.

Surface preparation steps include multi-step lapping process and then mechanical polishing. Several steps of lapping with different size of abrasives were applied primarily to reduce the thickness, roughness and damage zones. Material removal rate studies were deeply studied for the crystals with different crystallographic orientations and various zinc concentrations. The effect of applied pressure and plate velocity on MRR analyzed based on Preston Equation. Size of abrasive, crystal orientation, zinc concentration in CdZnTe material also directly influence the material removal rate as inside Preston constant. Thanks to MRR studies, lapping processes were optimized to obtain desired thickness with low surface damage.

In mechanical polishing, ultra-fine abrasives were used to obtain smooth and mirror-like surfaces. Abrasive concentration was optimized in terms of MRR and surface roughness. Even though sub-nanometer surface roughness ($\sim 0.8 \text{ nm}$) was achieved, polishing lines surrounded the surface. Mechanical polishing was followed by chemo-mechanical

polishing to avoid polishing lines. Chemical polishing was the final polishing step to reduce surface roughness further. Sub-nanometer surface roughness of 0.4 nm was achieved over relatively large area ($\sim 2 \text{ mm}^2$). Moreover, after final polishing, total thickness variation was recorded as low as 1 μm . It was shown that success of chemical polishing was strongly depending on the pH value of the slurry. Slightly basic solutions seemed to provide better uniformity on the wafers rather than acidic solutions.

Surface finishing studies could be further optimized if white-light interferometry system was owned at in house facility. Lack of this instrument prevents to obtaining instant feedbacks after each intermediate surface finishing step.

Throughout this work, characterizations of produced wafers were conducted in terms of surface, structural, compositional, optical, and mechanical characterization tools.

As a surface characterization, optical microscope and scanning electron microscopy were employed to investigate the surface quality after each surface preparation. It was shown that different type of surface damage depends on material removal mechanism. It was also shown that surface cleaning was one of the major issue.

XRD measurements showed that additional peaks, belonging to different crystallographic orientations, appeared for sliced wafer with twinning method and more intense major peaks were observed for sliced wafer with x-ray back reflection method. It was found that additional peaks disappear after mirror-like polished and minor peaks shifted to their exact position.

EDX measurements showed uniform Zn homogeneity (around 10%) after each surface process for $\text{Cd}_{0.90}\text{Zn}_{0.10}\text{Te}$ crystals. Surface of crystals were stoichiometric after each surface treatment since the ratio of overall Te to Cd+Zn was around 1. It was also shown that 4% Zn concentration in large surface area ($20 \times 20 \text{ mm}^2$) $\text{Cd}_{0.96}\text{Zn}_{0.04}\text{Te}$ finished wafer.

Infrared transmittance of 60% was achieved for METU-grown crystals. It was claimed that surface must be double side polished (reflected surfaces) to avoid scattering of surface morphology. It was also shown that decreasing of IR-transmittance for double side polished sample related to crystal quality.

Crystals were chemically etched to explore crystal quality. Inoue, Everson and Nakagawa etchants were utilized to reveal etch pits (dislocations) and inclusions. Surface of crystal should be mirror-like to observe dislocations. Different crystallographic orientations can be etched with Inoue etchant while Nakagawa and Everson etchants only work on {111} and {211} orientations. Different shape of Te-inclusions were observed just after polishing steps and chemical etch. It was shown that different etchants had different etch rates on Te and CdZnTe matrix.

Subsurface damage after lapping and mechanical polishing studies were analyzed using bonded interface method. It was found that abrasive size had strong effect on crack formations under the surface. This method is insufficient to observe subsurface damage after mechanical polishing. New methods such as angle polishing can be used as future studies.

As future studies, chemical polishing studies can be improved using different combinations of proper chemicals. Surface chemistry and oxidation studies can be added to chemical polishing studies in order to measure oxide thickness after the processes. Moreover, subsurface damage and lattice deformations of finished samples can be analyzed with high resolution transmission electron microscopy.



REFERENCES

- [1] S. Tari, F. Aqariden, Y. Chang, C. Grein, J. Li, and N. Kioussis, "Impact of surface treatment on the structural and electronic properties of polished CdZnTe surfaces for radiation detectors," *J. Electron. Mater.*, vol. 42, no. 11, pp. 3252–3258, 2013.
- [2] P. Capper and J. Garland, *Mercury Cadmium Tellurite, Growth, Properties and Applications*. Wil, 2011.
- [3] O. S. Babalola, "Surface and Bulk Defects in Cadmium Zinc Telluride and Cadmium Manganese Telluride Crystals," *PhD Diss.*, no. Vanderbilt University, 2009.
- [4] T. Asahi, O. Oda, Y. Taniguchi, and A. Koyama, "Characterization of 100 mm diameter CdZnTe single crystals grown by the vertical gradient freezing method," *J. Cryst. Growth*, vol. 149, no. 1–2, pp. 23–29, 1995.
- [5] S. del Sordo, L. Abbene, E. Caroli, A. M. Mancini, A. Zappettini, and P. Ubertini, "Progress in the development of CdTe and CdZnTe semiconductor radiation detectors for astrophysical and medical applications," *Sensors*, vol. 9, no. 5, pp. 3491–3526, 2009.
- [6] K. C. Mandal *et al.*, "Characterization of Low-Defect Cd 0 : 9 Zn 0 : 1 Te Frisch Collar Detectors," *IEEE Trans. Nucl. Sci.*, vol. 54, no. 4, pp. 802–806, 2007.
- [7] P. Moravec *et al.*, "Chemical polishing of CdZnTe substrates fabricated from crystals grown by the vertical-gradient freezing method," *J. Electron. Mater.*, vol. 35, no. 6, pp. 1206–1213, 2006.
- [8] P. Capper, *Bulk Crystal Growth of Electronic, Optical & Optoelectronic Materials*. West Sussex: Wiley, 2005.
- [9] Q. Zheng, "Preparation and Development of CdTe and CdZnTe Detectors for Gamma Ray Radiation Applications PhD Dissertation," *PhD*, no. October, 2012.

- [10] P. Capper, "Properties of narrow gap cadmium-based compounds," *III-Vs Review*, vol. 8, no. 2. INSPEC, London, 1995.
- [11] Z. Zhang, H. Gao, W. Jie, D. Guo, R. Kang, and Y. Li, "Chemical mechanical polishing and nanomechanics of semiconductor CdZnTe single crystals," *Semicond. Sci. Technol. Semicond. Sci. Technol.*, vol. 23, no. 23, pp. 105023–9, 2008.
- [12] R. Singh *et al.*, "Molecular beam epitaxy growth of high-quality HgCdTe LWIR layers on polished and repolished CdZnTe substrates," *J. Electron. Mater.*, vol. 34, no. 6, pp. 885–890, 2005.
- [13] R. K. Willardson, A. C. Beer, and E. R. Weber, *Semiconductors for room-temperature nuclear detector application*. California: Academic Press, 1995.
- [14] M. Fiederle, a Fauler, V. Babentsov, J. P. Konrath, and J. Franc, "Growth of high resistivity CdTe and (Cd,Zn)Te crystals," *Proc. SPIE - Int. Soc. Opt. Eng.*, vol. 5198, no. 7, pp. 48–53, 2004.
- [15] C. Szeles, S. E. Cameron, J. O. Ndap, and W. C. Chalmers, "Advances in the crystal growth of semi-insulating CdZnTe for radiation detector applications," *IEEE Trans. Nucl. Sci.*, vol. 49 II, no. 5, pp. 2535–2540, 2002.
- [16] Z. Zhang, H. Gao, W. Jie, D. Guo, R. Kang, and Y. Li, "Chemical mechanical polishing and nanomechanics of semiconductor CdZnTe single crystals," *Semicond. Sci. Technol.*, vol. 23, p. 105023, 2008.
- [17] A. J. Strauss, A. J. S. The, and D. P. Appliquee, "The physical properties of cadmium telluride," *Rev. Phys. Appliquée*, vol. 12, no. 2, pp. 167–184, 1977.
- [18] R. Triboulet and P. Siffert, *CdTe and Related Compounds; Physics, Defects, Hetero-and Nano-structures, Crystal Growth, Surfaces and Applications: Physics, CdTe-based*. 2009.
- [19] H. Bensalah, "The Effect of Crystal Growth Conditions and Surface Treatment on CdZnTe Bulk Single Crystal," 2013.

- [20] T. . Schlesinger *et al.*, “Cadmium zinc telluride and its use as a nuclear radiation detector material,” *Mater. Sci. Eng. R Reports*, vol. 32, no. 4–5, pp. 103–189, 2001.
- [21] D. B. Holt, “Surface polarity and symmetry in semiconducting compounds - Part 1 Macroscopic effects of polarity,” *J. Mater. Sci.*, vol. 23, no. 3, pp. 1131–1136, 1988.
- [22] C. H. Gatos and M. C. Lavine, “Etching and Inhibition of The {111} Surfaces of the III-V Intermetallic Compounds: InSb,” *J. Phys. Chm. Solids*, vol. 14, pp. 169–174, 1960.
- [23] E. P. Warekois, M. C. Lavine, A. N. Mariano, and H. C. Gatos, “Crystallographic polarity in the II-VI compounds,” *J. Appl. Phys.*, vol. 33, no. 2, pp. 690–696, 1962.
- [24] P. D. Brown, K. Durose, G. J. Russell, and J. Woods, “The absolute determination of CdTe crystal polarity,” *J. Cryst. Growth*, vol. 101, no. 1–4, pp. 211–215, 1990.
- [25] K. Durose, “Structural Defects in CdTe,” 1986.
- [26] D. Zeng, W. Jie, T. Wang, and G. Zha, “Residual stress and strain in CdZnTe wafer examined by X-ray diffraction methods,” *Appl. Phys. A Mater. Sci. Process.*, vol. 86, no. 2, pp. 257–260, 2007.
- [27] A. Sher, “Effects influencing the structural integrity of semiconductors and their alloys,” *J. Vac. Sci. Technol. A Vacuum, Surfaces, Film.*, vol. 3, no. 1, p. 105, 1985.
- [28] Y. Li, W. Jie, R. Kang, and H. Gao, “Effect of mechanical anisotropy on material removal rate and surface quality during polishing CdZnTe wafers,” *Rare Met.*, vol. 30, no. 4, pp. 381–386, 2011.
- [29] Y. Li, R. Kang, H. Gao, J. Wang, and Y. Lang, “Nanomechanical behaviors of (110) and (111) CdZnTe crystals investigated by nanoindentation,” *Rare Met.*, vol. 28, no. 6, pp. 570–575, 2009.
- [30] W. C. Oliver and G. M. Pharr, “An Improved Technique for Determining Hardness and Elastic Modulus Using Load and Displacement Sensing Indentation Experiments,” *J. Mater. Res.*, vol. 7, pp. 1564–1584, 1992.

- [31] S. Sen, D. R. Rhiger, C. R. Curtis, M. H. Kalisher, H. L. Hettich, and M. C. Currie, “Infrared absorption behavior in CdZnTe substrates,” *J. Electron. Mater.*, vol. 30, no. 6, pp. 611–618, 2001.
- [32] L. I. Yujie, G. U. Zhi, L. I. Guoqiang, and J. I. E. Wanqi, “Infrared Transmission Spectra of Cd_{1-x}Zn_xTe (x=0 . 04) Crystals,” vol. 33, no. 8, pp. 1–3, 2004.
- [33] V. C. Valero, “GROWTH AND CHARACTERIZATION OF Cd_{0.85}Zn_{0.15}Te CRYSTALS DOPED WITH Bi.”
- [34] M. Bugar, “Dynamics of structural defects in CdTe-based semiconductors,” *Med. Lav.*, vol. 101, no. 5, p. 91, 2011.
- [35] G.-Q. Li, W.-Q. Jie, Z. Gu, and H. Hua, “Correlation between the IR Transmission Spectra and the CdZnTe Qualities,” *Chinese Phys. Lett.*, vol. 20, no. 9, pp. 1600–1602, 2003.
- [36] P. Rudolph, “Fundamentals and engineering of defects,” *Prog. Cryst. Growth Charact. Mater.*, 2016.
- [37] G. Li, S. J. Shih, Y. Huang, T. Wang, and W. Jie, “Nanostructures of defects in CdZnTe single crystals,” *J. Cryst. Growth*, vol. 311, no. 1, pp. 85–89, 2008.
- [38] G. Dhanaraj, K. Byrappa, V. Prasad, and M. Dudley, *Springer Handbook of Crystal Growth*. 2010.
- [39] D. Zeng, W. Jie, T. Wang, and H. Zhou, “Transmission electron microscopy observations of twin boundaries and sub-boundary networks in bulk CdZnTe crystals,” *J. Cryst. Growth*, vol. 311, no. 19, pp. 4414–4417, 2009.
- [40] S. Hu, C. H. Henager, and L. Chen, “Simulations of stress-induced twinning and de-twinning: A phase field model,” *Acta Mater.*, vol. 58, no. 19, pp. 6554–6564, 2010.
- [41] P. Rudolph, “Dislocation patterning and bunching in crystals and epitaxial layers - a review,” vol. 15, no. August, pp. 1–15, 2016.
- [42] J. Crocco, T. Advisor, and T. Tribunal, “Crystal Growth & Technology , Device

Fabrication , and Material Properties of Cd (Zn) Te for Radiation Detector Applications.”

- [43] J. Schreiber, L. Horing, H. Uniewski, S. Hildebrandt, and H. S. Leipner, “Recognition and distribution of A(g) and B(g) dislocations in indentation deformation zones on {111} and {110} surfaces of CdTe,” *Phys. Status Solidi Appl. Res.*, vol. 171, pp. 89–97, 1999.
- [44] M. Inoue, I. Teramoto, and S. Takayanagi, “Etch Pits and Polarity in CdTe Crystals,” *J. Appl. Phys.*, vol. 33, no. 8, pp. 2578–2582, 1962.
- [45] K. Nakagawa, K. Maeda, and S. Takeuchi, “Observation of dislocations in cadmium telluride by cathodoluminescence microscopy,” *Appl. Phys. Lett.*, vol. 34, no. 9, pp. 574–575, 1979.
- [46] W. J. Everson, C. K. Ard, J. L. Sepich, B. E. Dean, G. T. Neugebauer, and H. F. Schaake, “Etch pit characterization of CdTe and CdZnTe substrates for use in mercury cadmium telluride epitaxy,” *J. Electron. Mater.*, vol. 24, no. 5, pp. 505–510, 1995.
- [47] P. Rudolph, M. Neubert, and M. M:uhlberg, “Defects in CdTe bridgman monocrystals caused by nonstoichiometric growth conditions,” *J. Cryst. Growth*, vol. 128, no. 1–4 PART 2, pp. 582–587, 1993.
- [48] M. Wada and J. Suzuki, “Characterization of Te precipitates in CdTe crystals,” *Jpn. J. Appl. Phys.*, vol. 27, no. 6, pp. 972–975, 1988.
- [49] Y. Xu *et al.*, “Investigation of Te inclusion induced glides and the corresponding dislocations in CdZnTe crystal,” *CrystEngComm*, vol. 14, no. 2, pp. 417–420, 2012.
- [50] R. D. S. Yadava, R. K. Bagai, and W. N. Borle, “Theory of te precipitation and related effects in CdTe Crystals,” *J. Electron. Mater.*, vol. 21, no. 10, pp. 1001–1016, 1992.
- [51] Y. He *et al.*, “Matrix-controlled morphology evolution of Te inclusions in CdZnTe

- single crystal,” *Scr. Mater.*, vol. 67, no. 1, pp. 5–8, 2012.
- [52] E. Belas *et al.*, “Reduction of inclusions in (CdZn)Te and CdTe:In single crystals by post-growth annealing,” *J. Electron. Mater.*, vol. 37, no. 9, pp. 1212–1218, 2008.
- [53] G. A. Carini, A. E. Bolotnikov, G. S. Camarda, G. W. Wright, L. Li, and R. B. James, “EFFECT OF TE PRECIPITATES ON THE PERFORMANCE OF CdZnTe (CZT) DETECTORS,” *Appl. Phys. A Mater. Sci. Process.*, vol. 88, 2006.
- [54] L. Yan, K. Renke, G. Hang, and W. Dongjiang, “Damage mechanisms during lapping and mechanical polishing CdZnTe wafers,” *Rare Met.*, vol. 29, no. 3, pp. 276–279, 2010.
- [55] Z. Zhang, Y. Meng, D. Guo, R. Kang, and H. Gao, “Nanoscale machinability and subsurface damage machined by CMP of soft-brittle CdZnTe crystals,” *Int. J. Adv. Manuf. Technol.*, vol. 47, no. 9–12, pp. 1105–1112, 2010.
- [56] Z. Zhang, Y. Meng, D. Guo, L. Wu, Y. Tian, and R. Liu, “Material removal mechanism of precision grinding of soft-brittle CdZnTe wafers,” *Int. J. Adv. Manuf. Technol.*, vol. 46, no. 5–8, pp. 563–569, 2010.
- [57] X. Le and M. L. Peterson, “Material removal rate in flat lapping,” *J. Manuf. Process.*, vol. 1, no. 1, pp. 71–78, 1999.
- [58] Y. V. Milman, A. A. Golubenko, and S. N. Dub, “Indentation size effect in nanohardness,” *Acta Mater.*, vol. 59, no. 20, pp. 7480–7487, 2011.